UAB
Universitat Autònoma de Barcelona

New insights into Cr electrodeposits obtained from Cr(III)-based electrolytes: effect of the chemistry and semiconducting properties of their oxide films on the corrosion behaviour

Jonathan León

Tesi Doctoral
Programa de Doctorat en Ciència de Materials

Jesús Manuel Vega (director)

Eva García Lecina (directora)

Eva Pellicer Vilà (tutora)

Departament de Física

Facultat de Ciències

2021

UAB
Universitat Autònoma de Barcelona

Memòria presentada per aspirar al Grau de Doctor per

Jonathan León Moro

Vist i plau

Jesús Manuel Vega Vega	Eva García Lecina	Eva Pellicer Vilà
(Director)	(Directora)	(Tutora)

Bellaterra, 26/11/2021

El **Dr. Jesús Manuel Vega Vega**, responsable de l'àmbit de coneixement Corrosión y Tribología de CIDETEC Suface Engineering en Fundación CIDETEC,

la **Dra. Eva García Lecina**, directora de CIDETEC Surface Engineering en Fundación CIDETEC,

i la **Dra. Eva Pellicer Vilà**, professora agregada del Departament de Física de la Universitat Autònoma de Barcelona,

CERTIFIQUEN:

Que **Jonathan León Moro** ha realitzat sota la seva direcció el treball d´investigació que s´exposa a la memòria titulada "New insights into Cr electrodeposits obtained from Cr(III)-based electrolytes: effect of the chemistry and semiconducting properties of their oxide films on the corrosion behaviour" per optar al grau de **Doctor per la Universitat Autònoma de Barcelona**.

Que el disseny del experiments, síntesi de mostres, llur caracterització, l'anàlisi dels resultats, la redacció dels articles i de aquesta memòria són fruit del treball d´investigació realitzat per Jonathan León Moro.

I perquè així consti, signen el present certificat,

Jesús Manuel Vega Vega   Eva García Lecina   Eva Pellicer Vilà

Bellaterra, 26/11/2021

i. Acknowledgments

A lot of people have lent me help and assistance during the course of this research work, therefore, I would like to take the opportunity to acknowledge their contribution to the development of this Ph.D.

First of all, I would like to thank the role and the guidance provided by my directors, Doctor Eva Gacía Lecina and Doctor Jesús Manuel Vega. Definitely, the achievement and quality of this investigation would not have been possible without their help. At the same time, I would like to acknowledge the whole team that are behind them, since people from all the departments of CIDETEC have somehow lend me a hand when necessary. Special thanks to both Corrosion and Tribology and Electrodeposition groups for their continuous active support. I would also like to mention my Ph.D. colleague, Larraitz Ganborena, who accompanied me in this adventure, both in the good and in the hard moments and who recently defended his Ph.D. successfully.

Secondly, due to the international nature of this Ph.D., I have stayed at different universities/institutes where I met a lot of people that became part of this work. Many thanks to the SURF research group of the Vrije Universiteit Brussel (VUB) for taken in me for 3 months in their laboratories, where I learnt a lot about surface analysis and corrosion, but also, I was able to perform experimental measurements in their facilities using their equipment. This was possible thank to the help of Professor Herman Terryn and Professor Annick Hubin. I would also like to thank to the technicians, postdoctoral and Ph.D. students of the group for helping me carrying out the experimental measurements and also for making me feel part of the team from the first day. Here I would like to mention the help of Priya Laha, Oscar Steenhaut and Sven Pletincx.

CorrIS research group from the Institut National des Scienses Appliquées (INSA) of Lyon is also acknowledge here, especially the help of the Professor Bernard Normand and Professor Benoît Ter-Ovanessian. I thank them for allowing me to stay in their laboratories where I learnt lots of things about the electrochemical characterisation of surfaces, specifically on the characterisation of semiconducting properties of thin oxide layers. Once again, I would like to mention the Ph.D. students of this research group for their help during my stay with them, as well as for making me feel like one more of the team.

ii. Abstract

Decorative chromium coatings are one of the most used aesthetic finishes in the industry. Particularly, such coatings have been widely employed in the automotive sector, among others, for coating both plastic and metal components. Although these coatings were traditionally obtained using Cr(VI)-based electroplating baths, nowadays, the use of hexavalent chromium is limited by EU regulations due to its high toxicity and carcinogenic effects Consequently, Cr(III)-based electrolytes have been widely explored as one of the main alternative over the last decades.

Such decorative Cr coatings are featured by their metallic bright appearance and the high corrosion resistance. In fact, the latter can be achieved without any aesthetic impact on the surface thanks to a multilayer configuration: e.g., having three nickel layers underneath the chromium one. The goal of such multilayer configuration is to maintain hidden the corrosion front by guiding it below the surface (i.e., located in the underneath bight nickel layer). Therefore, the overall corrosion performance belongs to a combination effect of the different nickel layers and the top-chromium one. However, the corrosion performance of the thin Cr layer (200 – 300 nm) itself has not been explored in detail.

In particular, this Ph.D. thesis is focused on studying different Cr coatings/electrodeposits obtained from model Cr(III)-based baths (a chloride and a sulphate-based one). Coatings obtained from a Cr(VI)-based electroplating bath were used as a reference system as well as pure Cr. The composition and physicochemical properties of such thin chromium layers (below 0.4 µm) and their native oxide (< 5 nm) are assumed to be governing the corrosion resistance; therefore, a detailed characterisation was carried out on the different coatings: the corrosion behaviour (by linear and non-linear potentiodynamic polarisation tests), the semiconducting properties of the oxide layers (by Mott-Schottky and Point Defect Model), the kinetic of such oxide formation (by current-time transients) as well as the composition (by AES, XPS and synchrotron-based XANES).

Initially, despite very similar physicochemical properties were found for both Cr(III)-based electroplating baths (chloride and sulphate), the sulphate-based system presented a lower C concentration in the Cr layer and traces of adsorbed and absorbed S on its surface and inside the Cr layer, respectively. Moreover, the semiconducting properties of their native oxide layers revealed a higher defect concentration (Mott-Schottky results) for the sulphate-

based coating. Such features were attributed to the presence S which was found to hinder the formation of the native oxide layer, triggering the formation of a less protective oxide film. As a consequence, a lower corrosion resistance was observed for the sulphate-based electrodeposits in the borate buffer (pH 8.4) electrolyte. Using more aggressive electrolytes such as NaCl, it was revealed no difference in the corrosion resistance performance of both *as obtained* Cr(III)-based coatings. However, aged (1 year) sulphate-based systems showed a higher corrosion resistance in comparison to the chloride-systems when testing the passive film breakdown by varying the chloride content in the NaCl electrolyte.

On the other hand, since Fe is used as an additive to decrease the deposition rate of the electroplating process in commercially Cr(III)-based baths, its impact in the final Cr coatings was explored using a model sulphate-based Cr(III) bath. It was found that, independently of the concentration, adding Fe caused the electrodeposition of a Cr-Fe alloy instead of a Cr layer. Moreover, if the bath is doped in the 100 - 400 mg/L Fe range, a duplex Fe-Cr native oxide layer is formed. This affected dramatically to (i) the semiconductor properties of such native oxide layers, introducing a new n-type semiconductor behaviour with the subsequent increase of point defects, and (ii) their oxide formation kinetics: slowing it down and triggering the formation of a more porous oxide layer. As a result, doping the bath with 8 mg/L of Fe decreases the deposition rate of the process and provides a proper corrosion protection, maintaining the properties of the oxide layer (i.e., semiconducting, homogeneity, etc.). In contrast, if the concentration was 100 mg/L Fe or higher, a detrimental effect on the corrosion resistance performance was observed.

Finally, the Cr(VI) and Cr(III) systems were investigated and compared. In general, the Cr(VI)-based electrodeposits showed a better performance in terms of corrosion resistance, probably caused by the presence of a thin topmost CrO_3 layer on the native oxide layer. This additional topmost oxide layer is believed to be the responsible of enhancing the corrosion resistance of the coatings, due to: (i) the low defects concentration of the native oxide layers and low diffusion coefficient, and (ii) the fast oxide formation kinetics and lower passivation current value. This CrO_3 layer was revealed by synchrotron-based XANES measurements and it was assumed to be formed in the electroplating bath, which works at highly acid and oxidising conditions. Indeed, when the coating was polished, this topcoat CrO_3 layer was removed and the semiconducting properties were very similar to the Cr(III)-based systems (native oxide layer constituted mainly by Cr(III)-based oxide and hydroxides).

iii. Resumen

Los recubrimientos de cromo decorativos son uno de los acabados estéticos más utilizados en la industria. En particular, tales recubrimientos han sido ampliamente usados en el sector de la automoción, entre otros, para recubrir componentes tanto plásticos como metálicos. Aunque estos recubrimientos se obtenían tradicionalmente mediante baños de electrodeposición basados en sales de Cr(VI), en la actualidad, el uso de cromo hexavalente está limitado por regulaciones de la UE debido a su alta toxicidad, por lo que se encuentra en proceso de ser sustituido. Desde entonces, los electrolitos basados en Cr(III) se han convertido en una de las principales alternativas en las últimas décadas.

Dichos recubrimientos de Cr decorativos se caracterizan por su aspecto metálico brillante y su alta resistencia a la corrosión. De hecho, esto último se puede lograr sin sufrir ningún impacto estético en la superficie gracias a su configuración multicapa: por ejemplo, teniendo tres capas de níquel debajo de la de cromo. El objetivo de dicha configuración multicapa es mantener oculto el frente de corrosión guiándolo bajo la superficie (es decir, hacia las capas inferiores de níquel brillo). Por lo tanto, el comportamiento global frente a la corrosión viene dado por el efecto de la combinación de las diferentes capas de níquel y la superior de cromo. Sin embargo, el comportamiento frente a la corrosión de la capa fina de Cr (200 - 300 nm) no se ha explorado de manera aislada respecto de las capas de níquel que se encuentran debajo.

En particular, esta tesis se centra en el estudio de diferentes recubrimientos/electrodepósitos de Cr, únicamente de la capa de Cr y de su óxido, obtenidos a partir de baños modelo de Cr trivalente (basado en cloruros y sulfatos). Se supone que la composición y las propiedades fisicoquímicas de dichas capas finas de cromo (por debajo de 0,4 µm) y sus capas de óxido nativo (< 5 nm) gobiernan la resistencia a la corrosión; por lo tanto, se ha realizado una caracterización exhaustiva sobre los diferentes recubrimientos, incluyendo unos usados a modo de sistema de referencia obtenidos a partir de un baño de electrodeposición de Cr(VI): comportamiento electroquímico (mediante pruebas de polarización potenciodinámica lineal y no lineal), las propiedades semiconductoras de las capas de óxido (Mott-Schottky y *Point Defect Model*) y la cinética de formación del óxido (por medio del estudio de *current-time trasnsients*), así como una caracterización de su composición (AES, XPS y XANES basado en sincrotrón).

Inicialmente, a pesar de que se encontraron propiedades fisicoquímicas muy similares para ambos baños de electrodeposición de Cr(III) (cloruro y sulfato), el sistema basado en sulfato presentó una menor concentración de C en la capa de Cr y trazas de S adsorbido y absorbido en su superficie y dentro de la capa de Cr respectivamente. Además, las propiedades semiconductoras de sus capas de óxido nativas revelaron una mayor concentración de defectos electrónicos (resultados de Mott-Schottky). Tales características se atribuyeron a la presencia de S, el cual dificulta la formación de la capa nativa de óxido, dando lugar a una capa de óxido menos protectora. Como consecuencia, se observó una menor resistencia a la corrosión en el electrolito de tampón borato (pH 8.4) para los recubrimientos de Cr basados en sulfatos. El uso de electrolitos más agresivos como NaCl no reveló diferencias en las propiedades de resistencia a la corrosión de ambos recubrimientos de Cr (III) cuando se analizaron las muestras tras ser obtenidas del baño (*as obtained*); sin embargo, cuando se incrementó el tiempo entre la obtención y el análisis de las muestras, el sistema basado en sales de sulfato mostró una mayor resistencia a la corrosión en comparación con el sistema de cloruros al evaluar la resistencia de la capa pasiva realizando medidas electroquímicas variando el contenido de cloruro en el electrolito de NaCl.

Por otro lado, dado el Fe se usa como aditivo para reducir la tasa de deposición durante el proceso de electrodeposición de Cr(III) en los sistemas comerciales, se investigó su efecto final sobre los recubrimientos de Cr usando un baño modelo de Cr(III) basado en sales de sulfatos. Se encontró que, independientemente de la concentración, la adición de Fe provocó la electrodeposición de una aleación de Cr-Fe en lugar de una capa de Cr. Además, si el baño se dopaba con un rango de concentración de Fe comprendido entre 100 y 400 mg/L, se formaba una capa de nativa de óxido dúplex de Fe-Cr. Esto afectó dramáticamente a (i) las propiedades semiconductoras de tales capas nativas de óxido, introduciendo un nuevo comportamiento semiconductor de tipo n con el subsecuente aumento de defectos electrónicos, y (ii) su cinética de formación de óxido: ralentizándola y promoviendo la formación de una capa de óxido más porosa. Como resultado, dopar el baño con 8 mg/L de Fe permitió mejorar la tasa de deposición del proceso al mismo tiempo que proporcionaba una protección adecuada contra la corrosión y mantenía las propiedades de la capa de óxido (semiconductoras, homogeneidad, etc.). Sin embargo, si la concentración de Fe en el baño era de 100 mg/L, se obtuvo un efecto perjudicial sobre la resistencia a la corrosión.

Finalmente, se investigaron y compararon los sistemas Cr(VI) y Cr(III). En general, los electrodepósitos obtenidos por medio de Cr(VI) mostraron un mejor desempeño en cuanto a resistencia a la corrosión se refiere, probablemente causado por la presencia de una capa fina de CrO_3 que se observó sobre la capa de óxido nativa. Se cree que esta capa de óxido adicional es la responsable de mejorar la resistencia a la corrosión de los recubrimientos, debido a: (i) la baja cantidad de defectos electrónicos encontrados en la capa de óxido nativo y el bajo coeficiente de difusión y (ii) la rápida cinética de formación de óxido. Esta capa de CrO_3 se observó mediante medidas de XANES basadas en radiación de sincrotrón y se asumió que se formó en el baño de electrodeposición de Cr(VI), ya que trabaja bajo condiciones altamente ácidas y oxidantes. De hecho, cuando se pulió el recubrimiento, esta capa de CrO_3 se eliminó y las propiedades fueron modificadas, alcanzando valores muy similares a las de los sistemas basados en Cr(III), cuyas capas de óxido estaban constituidas principalmente por óxidos e hidróxidos de Cr(III).

Table of content

CHAPTER 1. INTRODUCTION

1.1 Electroplated Cr coatings

Electroplating is an electrolytic process in which metallic species, that are dissolved in a solution, are applied by the reduction of their metallic cations (caused by a direct electric current) on the surface of a different metal. Electroplated chromium is widely used in the industry as a surface finishing to confer new features that the bare materials (used in this case as substrate) do not present. Among the diverse existing chromium coating types, the hard chromium and the decorative chromium plating are well-known [1–3]. Both types of coatings are based on the same manufacturing process but they are obtained under different working conditions, providing systems with different features and final applications.

On the one hand, the hard chromium, also called engineered or industrial chrome, is commonly applied directly on the metal substrate (usually, steel, copper or brass) with a standard thickness of 20 - 40 µm, reaching sometimes even 100 µm depending on the final application. Long electroplating time and high current density are required for this process. These hard chromium coatings have properties such us heat, wear, erosion and corrosion resistance, as well as a high hardness [4–6], making them suitable for applications like machinery parts (which usually operates at very high temperature) or even moving parts like pistons or hydraulic cylinders [7,8].

On the other hand, the decorative chromium coatings are generally applied on previously nickel plated metallic surfaces or directly on stainless steel [1,9]. In contrast to hard chromium, they have a considerably lower thickness (usually ranged between 0.4 - 0.8 µm) and therefore a less durability is achieved for similar applications. However, in such decorative coatings the aesthetic appearance and the corrosion resistance are the targeted properties. That is the reason why they are mainly used for covering tools, kitchen utensils and car parts, where a shiny and smooth appearance are desired as well as easy cleaning and resistance to external oxidising agents [10].

Particularly, this thin so-called decorative chromium has been very used in the automotive sector, being implemented in interior and exterior parts due to its bright appearance, colour and corrosion resistance performance. In general, such decorative chromium coatings are also known as nickel-chrome coatings because they are electroplated with a multilayer configuration of different nickel layers, having the decorative Cr layer (around 200 - 500 nm) as the topmost layer. This nanometric Cr layer is enough to provide to the substrate with an elegant shiny metallic appearance whilst ensuring a long-lasting performance during the whole life cycle at the same time that preserves the good appearance. The multilayer nickel-

chrome system has been continuously improved over the years, aiming to enhance the lifetime of these coatings without affecting their aesthetic [11–13]. The idea behind this complex system is quite philosophical since, in few words, it lies in accepting the fact that sooner or later the surfaces will be corroded from a thermodynamic point of view. Instead of trying to avoid this fact, the multilayer systems are designed to guide the corrosion front inside the coating (i.e., underneath the top chromium layer and in between the nickel ones) through artificial micropores (*Figure 1*). Once the corrosion front has crossed vertically the outer microporous nickel layer, it starts to spread horizontally in such a way that the corrosion process is locked inside and put away from the topmost and good-looking Cr coating. Such corrosion mechanism occurs thanks to the different potential values existing between the different Ni layers, which relative values are indicated as positive or negative signs in the *Figure 1* [14,15].
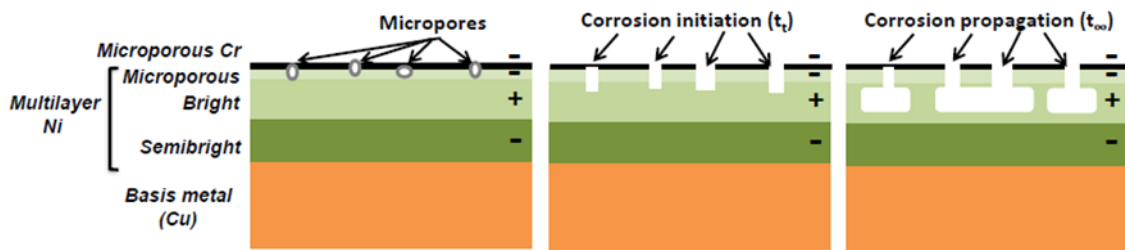
Figure 1. *Corrosion mechanism of the multilayer nickel-chrome system* [16,17].

1.1.1 Hexavalent-based electroplating baths

Traditionally, the topmost Cr layer of the decorative coatings was obtained using Cr(VI)-based electroplating baths; however, in 2000 the European Union (EU) approved a directive, commonly known as the end-of-life vehicle directive (ELV), in which the use of this chemical was limited and controlled by the European Chemicals Agency (ECHA) due to environmental and health concerns (Cr(VI) was found to be highly carcinogenic and mutagenic) [18,19]. Although the use of Cr(VI) was supposed to be completely removed (according to regulation of the EU called "Registration, Evaluation, Authorisation and Restriction of Chemicals (REACH)"), in April 2013 it was included in the Annex XIV of the list of substances subject to authorisation, allowing its use under certain limitations. Currently, the ECHA is under an investigation procedure to decide the further use or the complete prohibition of this substance. As a consequence, several researches were pushed on the search of Cr(VI)-free alternatives that could meet the same required properties of traditional Cr(VI)-based electrodeposits to completely substitute the process. Although several alternatives were explored, such as physical vapour deposition (PVD), chemical

vapour deposition (CVD), anodised aluminium, electroless nickel, etc. [20], Cr(III) seemed to be the main alternative to substitute to the Cr(VI) [21–23].

Several attempts to develop a Cr(III)-based electroplating bath were carried out in the past, but without commercial success. The first patents were registered in the period 1927 - 1929 but until the 1960s no electroplating bath based on Cr(III) was commercially available. Fortunately, suitable Cr(III)-based electroplating baths were developed in the last decades, mainly motivated by the imminent prohibition of the use of Cr(VI), obtaining coatings with similar aesthetic properties and performance than the traditional Cr(VI)-based electrodeposits. Nowadays, even though the use of Cr(VI) has not been completely forbidden yet, most of the industrial process are currently based on the use of Cr(III) baths to obtain decorative chromium coatings. Nevertheless, even today there is no Cr(III)-based formulation capable of replicating perfectly the same capabilities than the coatings obtained using Cr(VI)-based electroplating baths.

1.1.2 Types of trivalent-based electroplating baths

Currently, there are two main types of Cr(III)-based baths: the chloride and the sulphate-containing (also known as chloride-free) baths [24,25]. The primary difference between them lies in the salts that are used in the formulation of their formulations: the chloride system contains chloride-based chromium and conducting salts (e.g., $CrCl_3$, KCl, NH_4Cl, etc.) whilst the sulphate-based system is characterised by not including any chlorides, where sulphate salts are commonly used (e.g., $Cr_4(SO_4)_5(OH)_2$, $Na_2(SO_4)$, etc.). Usually, the working parameters of the electroplating process are similar but in the *Table 1* some general differences of both Cr(III) electroplating baths are gathered.

Table 1. *Advantages and disadvantages of both Cr(III)-based electroplating baths.*

Bath type	Advantages	Disadvantages
Sulphate (chloride-free)	• Similar colour to the traditional Cr(VI)-based coating. • Higher resistance to metallic contamination. • Higher working temperature, easier maintenance of the chemical's concentration due to the higher evaporation (no need of removing water) • Less corrosive formulation.	• Higher cost, due to the use of Ti-based anodes. • Generally higher deposition rate (which can cause more stress and tensions in the coatings, leading to cracked surface).
Chloride	• Slightly higher deposition rate. • Less cost due to the use of graphite-based anodes.	• Greater colour difference in comparison to Cr(VI)-based electrodeposits. • Water removal required when adjusting the concentration of the chemical components due to the lower evaporation ratio (lower working temperature).

It has to be mentioned that even inside each family of Cr(III)-based baths (chloride or sulphate), there is a very comprehensive selection of different formulations and working conditions. In fact, despite the higher sensibility to metallic contamination of Cr(III)-based electroplating baths, it was found that the addition of small amounts of Fe could benefit the industrial process [26]. It was discovered that the Fe can act as a colouring agent providing a darker appearance as a consequence of its codeposition in the Cr layer [27,28], or even that it could also enhance the deposition rate of the Cr plating [29], as well as the corrosion resistance if the Cr(III)-based electrolyte contained a proper amount of Fe ions [30]. Typically, the Fe is added to Cr(III)-based electroplating baths as a soluble salt, being chloride or sulphate the preferably anion of such salts (depending on the type of the Cr(III)-based electroplating bath, i.e., if its chloride or chloride-free). Anions such as nitrates are not desirable due to their oxidising behaviour which may has a negative effect on the electroplating bath and the plating process [27]. In principle, both Fe^{2+} and Fe^{3+} ions could be added to the baths; however, traditionally Fe^{2+} was used instead of Fe^{3+} when dealing

with formulations containing hypophosphite in order to avoid the reduction of trivalent to divalent iron by the hypophosphite, which will lead to decreasing the concentration of the latter; Fe^{3+} could be added to the electroplating bath as long as it does not interfere with the rest of the chemical compounds. Therefore, Fe is sometimes added systematically in commercial Cr(III)-based electroplating baths since it has been empirically demonstrated that can benefit the Cr electrodeposition process.

1.1.3 Composition and working parameters of the electroplating baths

Despite the similarities between both Cr(III)-based systems, the formulation, deposition mechanism and working conditions of Cr(VI) and Cr(III)-based baths have been found to differ significantly. The *Table 2* shows some of these differences in terms of their chemistry and working parameters, comparing a model Cr(VI) and Cr(III)-based electroplating baths [25,31,32].

Table 2. Example of composition and working conditions of a model Cr(VI) and Cr(III)-based electrolytes.

Component	Electroplating bath	
	Cr (VI)	*Cr (III)*
CrO_3	300 g/L	
H_2SO_4	3.5 g/L	
Basic sulphate chromium [Cr(III)]		140 g/L (0.46 M)
HCOOH		250 g/L (5.43 M)
NH_3		90 g/L (5.3 M)
KBr		10 g/L (0.085 M)
PEG 400		0.5 g/L
Ammonium quaternary compounds		1 g/L
Working conditions	*Cr (VI)*	*Cr (III)*
Temperature (° C)	38 - 43	25 – 35
pH	< 1	2.5 – 2.8
Current density (A/dm^2)	9 - 15	4 – 10
Anode	Pb/Pb-based alloys	Graphite or Ti-based alloys
Deposition rate	0.1 µm/min	0,04 - 0,15 µm/min
Bath life	From several months to years	At least two months

As it can be observed in the table above, switching from a Cr(VI) to a Cr(III)-based electroplating process is not as straightforward as changing the chromium and conducting salts of the bath. The chemistry of the Cr(VI)-based electroplating baths is quite simple as it only requires a Cr(VI)-based salt as Cr source and a strong oxidant (typically H_2SO_4). In contrast, the Cr(III)-based formulation possess a more complex chemistry, including far more chemical components.

In fact, a Cr(III)-based electroplating bath required the following chemicals for a proper operation:

- **Cr(III) source**. Typically, chloride or sulphate-based salts.
- **Stabilising agent**. Normally, they are organic complexing molecules that are usually used together with lower amounts of other similar components (auxiliary complexing agents). Their purpose is to ease the Cr(III) to metallic electroreduction process (more details in the section 1.1.4).
- **Buffering agent.** The pH must be maintained in constant values because in the cathode the hydrogen evolution secondary reaction can take place, which will cause local pH increasing. A high pH could promote the formation of chromium hydroxides which will precipitate due to their low solubility, reducing as a result, the efficiency of the process.
- **Conducting salts.** These baths are featured by having a low electrical conductivity; therefore, adding conducting salts are need to improve the energetic efficiency of the electroplating process.

- **Other components like brighteners or moistening additives**. Organic molecules added in very low amounts that are aimed to improve the penetration and the covering distribution of the electrodeposition.

Regarding the working conditions of both systems (*Table 2*), on the one hand, Cr(VI)-based baths work under very acid and oxidant conditions, as well as at higher temperatures and current densities. They also require the use of Pb-based anodes which are also known for being highly toxic. On the other hand, Cr(III)-based electrolytes operate under milder conditions as their pH is higher whilst their working temperature and current density are lower. Although, graphite anodes can be used, a secondary reaction can take place at such anodes in which Cr(III) could be oxidised to Cr(VI). Even if this reaction is not predominant since it occurs at a very low rate, it could be detrimental for the deposition rate and the efficiency of the electroplating process. This can be easily avoided by using Ti-based

anodes, which in contrast, are more expensive and increase the total cost of the process, together with the already mentioned higher amount of chemical components.

1.1.4 Electroplating mechanism

In theory, even if the formulation of Cr(VI) and Cr(III)-based electroplating baths and working conditions are different (*Table 2*), initially, similar nanometric Cr coatings are expected to be obtained. However, if the features of both Cr electrodeposits are compared (*Table 3*), it can be easily observed that they present different properties, as well as, a different colour and appearance (Cr(VI)-based coatings are blueish whilst Cr(III) ones are grey).

Table 3. *Comparison of certain features of Cr(III) and Cr(VI)-based Cr electrodeposits.*

Characteristic	*Electroplated coatings*	
	Cr (VI)	*Cr (III)*
Surface Hardness (HV)	800-900 *(decreasing when annealing)*	800-900 *(increasing up to 1500 after annealing)*
Surface morphology	Homogeneous	Nodular
Corrosion resistance	Excellent	Poor
Brightness (L* value)	> 85	80-85

The differences observed in the table above are significantly enough to claim that both obtained Cr electrodeposits have not the same properties and performance. Since there is a big difference in the formulations of their electroplating baths, the key parameter that makes the Cr electrodeposits different should lie in their obtaining mechanism. The study of such matter requires a brief the review and understanding of the Cr electroreduction mechanisms when using Cr(VI) or Cr(III).

On the one hand, the Cr electroplating process from Cr(VI) ions is simple and well-known as it has been used in the industry for more than 80 years. Cr(VI) ions can be reduced to metallic Cr in presence of a catalyst, which typically is the H_2SO_4, as proposed by Fink in his patent of 1926 [33]. Since then, all traditional Cr(VI)-based electroplating baths and processes have been based on Fink's formulation. Although no further discussion is done here about hexavalent chromium, it should be note that its electrodeposition mechanism is complex because it involves a six electrons reduction [34,35].

On the other hand, regarding the Cr(III), there are still some unknown details about its electroplating mechanism. The most popular hypothesis states that the electroreduction of

Cr(III) occurs via intermediate Cr(II) so that it is reduced to Cr(0) in a two steps reduction (*Figure 2*): first, the reduction of Cr(III) to Cr(II) takes place and then to metallic Cr [4,36].

Cr(III) $\xrightarrow[E^0 = -0.407 \text{ V}]{+e^-}$ **Cr(II)** $\xrightarrow[E^0 = -0.913 \text{ V}]{+2e^-}$ **Cr(0)**

$\xrightarrow[E^0 = -0.744 \text{ V}]{+3e^-}$
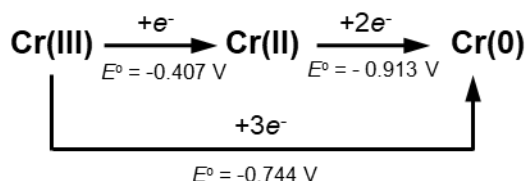
Figure 2. *Electrochemical reduction paths of the chromium ions and their standard reduction potentials.*

Initially, it could be considered that the direct reduction from Cr(III) to Cr(0) will be easy because other metals such as Zn possess a similar standard reduction potential and are known to be easily electroplated. However, Cr(III) cannot be electroplated in this way because, unlike Zn, Cr(III) can undergo other electron transfer reaction to form Cr(II). According to the scheme shown in the *Figure 2* this reduction (Cr(III) to Cr(II)) is more thermodynamically favoured and takes place preferentially. Further reduction of Cr(II) to metallic Cr will not occur due to the low standard reduction potential of that reaction, and as a consequence, no electroplated Cr will be obtained. Furthermore, its strong reducing properties will make Cr(II) to react with acidic medium to form hydrogen in the cathode, producing more Cr(III) as it is shown by the following reaction:

$$2\ Cr^{2+} + 2\ H^+\ \rightarrow\ 2\ Cr^{3+} + H_2 \qquad \text{(Reaction 1)}$$
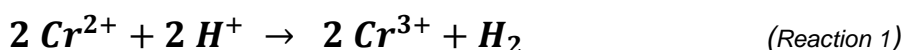
Therefore, according to the thermodynamics, the reduction of Cr(III) is not possible to occur and hydrogen gas will be generated instead of forming an electroplated Cr layer. However, the Cr(III) has also some kinetic issues: once the Cr(III) salt is dissolved, it forms an hexaacuo complex ($[Cr(H_2O)_6]^{3+}$) which is in equilibrium and undergoes a continuous ion exchange with the solvent. The Cr-water complex is very stable (actually, it has a very short bonding distance in comparison to other similar water-metal complexes) and it presents a very slow exchange rate with the solvent, hindering the availability of Cr(III) ions to react and be reduced at the cathode. Fortunately, the kinetics can be modified to make possible the reduction of Cr(III) to metallic Cr. Using complexing agents can enlarge the distance of the Cr-water bonds, decreasing as a consequence the stability of the hexaaquochromium complex, and allowing to Cr(III) ions to be reduced to metallic Cr [37]. This is the main reason why the Cr(III)-based electroplating baths possess a more complex chemistry in

their formulations as they require the use of more chemical components than the Cr(VI)-based baths.

Finally, it is important to highlight that such required compounds in the Cr(III)-based electroplating process (i.e., organic additives) not only affects to the mechanism but can also slightly modify the chemical composition of the electroplated Cr layer (e.g., to codeposit, to react, or event to get stuck in the coating) [38–40]. This is believed to be the main reason of the differences observed in the properties of the electroplated Cr layers obtained when using a Cr(VI) or a Cr(III)-based electroplating bath.

1.1.5 Corrosion performance and characterisation of the electroplated Cr coatings for decorative applications

As mentioned before, nowadays the decorative coatings are designed to maintain the aesthetic of the surface during the whole lifetime of the coating after exposure (indoor or outdoor) to aggressive environments or daily products such as cleaning detergents. Therefore, the multilayer system (nickel-chrome), shown in *Figure 1*, not only must fulfil the corrosion resistance requirement but also is required to maintain the aesthetic appearance during the whole service time [41]. Usually, the overall corrosion resistance performance of the different nickel layers as well as the top-chromium one is evaluated. However, the corrosion behaviour of the top chromium layer itself cannot be distinguished when using the multilayer configuration, as the measured response is a combination of all the system (i.e., all the nickel layers and the topmost Cr layer). Therefore, the top Cr coating has to be isolated as a "defect-free single layer" to understand its corrosion capabilities, exploring the protection depending on the composition of the bath, the type of bath (sulphate or chloride-based), the final composition of the Cr layer and its oxide layer as well as the semiconducting properties of the latter.

1.1.5.1 Corrosion performance

The corrosion performance of top Cr coatings is usually evaluated having several nickel layers underneath. Some authors observed that when using a single or duplex nickels layers underneath of four different chromium layers (one hexavalent-based, one chloride-based and two sulphate based), a higher i_{corr} for the chloride-based system in 5 % NaCl. This behaviour was attributed to the presence of microcracks whilst the other systems were crack-free [25]. On the one hand, if Cr(VI)-based coatings are compared to Cr(III) ones, in general the overall corrosion resistance is higher for Cr(VI) systems [10]. However,

decorative Cr(III)-based coatings are able to show higher corrosion resistance (impedance around $10^6 \, \Omega \, cm^2$) in 3 % NaCl [40] compared to hard Cr(III) and Cr(VI) coatings (impedance around $10^4 \, \Omega \, cm^2$) in 3.5% NaCl [42]. This demonstrates that the Cr electrodeposits can have diverse properties as a function of the substrate, electroplating bath, structure, presence or absence of microcracks/pores, type of electrolyte, etc. Therefore, electroplated defect-free Cr coatings isolated from the substrate have been obtained in this Ph.D. to avoid any side effect during the electrochemical characterisation and corrosion evaluation.

On the other hand, as it was previously introduced, the chemical components of the Cr(III) electroplating baths (e.g., the concentration of the chromium salt, additives, complexing agents, etc.) can affect the composition of the coatings and, consequently, can modify their corrosion performance. If the concentration of $Cr_2(SO_4)_3$ (salt as a source of Cr) varied from 0.05 to 0.2 M, not only the deposition rate was modified (faster when using the highest concentration) but also the corrosion behaviour was drastically affected (faster deposition rate promotes the formation of coatings with large cracks on the surface) [43]. Indeed, using the lowest Cr salt concentration resulted in the formation of a defect-free coating with a lower i_{corr} value. A similar study was carried out varying the amount of formaldehyde (additive) of a sulphate-based Cr(III) electroplating bath. The polarisation resistance was increased 6 times after adding 100 mg/L of such organic additive. However, increasing the concentration of formaldehyde above that threshold worsened the corrosion resistance [3]. In this way, complexing agents can also improve the corrosion behaviour. Although basic chloride-based Cr(III) coatings showed pits and cracks on the surface when testing its corrosion resistance in 3 %NaCl, adding aluminium chloride (acting as complexation agent and buffer assistant) hinders the formation of pits and cracks as well as increases the charge transfer resistance [40]. Using hypophosphite instead formic acid can also be used as example of the impact of different complexing agents: Cr-P layers (obtained by hypophosphite addition to a chloride-based Cr(III) bath) were found to exhibit a better corrosion resistance in 10 % HCl electrolyte in comparison to Cr(VI)-based and Cr-C coatings [44]. The current of the passive region was found to be 4 times lower in comparison to the other systems due to the presence of Cr phosphides in the oxide layer. Therefore, a detailed surface analysis is crucial to explain the different corrosion behaviour.

Finally, there are few studies focused on the detailed analysis of the different corrosion behaviour of Cr(III)-based coatings (chloride and sulphate-based systems). Although such coatings (Cr-C coatings electroplated on 4140 alloy steel using both baths) have shown similar corrosion resistance (i_{corr} of 1.67 and $1.54 \times 10^{-6} \, A \, cm^{-2}$, respectively) [45], a tailored characterisation has been done in this Ph.D. to figure out their singularities as a function of the used Cr(III)-bath (chloride and sulphate-based ones).

1.1.5.2 Surface Analysis

Usually, electroplated Cr coatings based on Cr(III) electrolytes for decorative applications show inclusions of other elements into their matrix due to the presence of organic additives (acting as complexing agents) among other compounds in the bath. In the previous section the strong effect that the complexing agents have on the corrosion resistance has been mentioned; however, they also have a significantly impact on the physicochemical properties of the electroplated coatings. In fact, different Cr coatings were obtained from chloride-based Cr(III) electroplating baths by varying the complexing agents: formic acid, ammonium formate, acetic acid and ammonium acetate [46]. Results revealed that the presence of ammonium led to the Cr coating with the highest C content (up to a 37 % atomic concentration (% at.) C when using ammonium acetate). However, a thinner Cr layer was obtained compared to the bath that included additives without ammonium, indicating that the efficiency was approximately reduced from 10 % to 5 %. If more than one organic complexing agent are simultaneously used in a sulphate-based Cr(III) baths (i.e., formic acid and carbamide (urea)) [36], their impact in the composition of the Cr layer is quite different, since independently of the formic acid concentration, the C content did not change in the electroplated Cr layer. In contrast, increasing the carbamide concentration in the bath rose the content of C in the Cr coating. In general, such C content is located inside of the metallic Cr matrix forming carbides, consequently, the electrodeposits obtained from Cr(III)-based electrolytes are referred as Cr-C or chromium carbide coatings [47–49]. Regarding to the structure of such Cr layers, it is claimed that the Cr-C coatings have a high amorphous grade (caused by the C insertion in the crystal lattice of the Cr, decreasing its crystallinity) which increases as a function of the C content [46,50]. The annealing process of the samples was able to reveal the carbide phases ($Cr_{23}C_6$ or Cr_7C_3 were revealed) by crystallising them [49,51,52].

Therefore, either the electrodeposition process or the Cr layer itself can be drastically affected by complexing agents. Beyond the modification of their C content, the addition of other type of complexing agents (carbon-free ligands or organic additives with other non-metals) also has a great impact on the chemical composition of the coatings. The formation of Cr-P coatings occurred in a chloride-based Cr(III) electroplating bath when using sodium hypophosphite monohydrate (phosphorus-based species) alone [44] or combined with other C-based auxiliary complexing agents [53]. On the other hand, coatings having absorbed S and N were obtained after using S-based and organic additives including functional groups with N (such as urea, thiourea, glycine or hydrazine) [54–56].

1.1.5.3 Semiconducting properties

It is generally agreed that the native oxide layer formed on metals are considered highly disordered films with point defects that can act as dopants, providing as a result a semiconductor behaviour [57,58]. These electronic properties are expected to play a key role in the electrochemical reactions that can take place at the surface [59–61]. Therefore, the study of the semiconducting properties can also provide useful information on the understanding of the passivity/protection capabilities of such oxide films [62]. In fact, these electronic properties can be related to the physicochemical properties of the oxide layer and their protective behaviour when exposed to an aggressive medium, i.e., their anticorrosion properties [63]. In fact, some authors observed that the presence of low point defects at the native oxide layer or a low capacitance can strongly affect to the protective behaviour of such oxide films, providing as a result a better corrosion resistance performance [64–67].

The electronic properties of the oxide layers strongly depend on the experimental protocol used to create such oxide films (typically formed electrochemically), the procedure to measure the semiconducting properties (e.g., potential range and direction of the polarisation) and the medium (electrolyte) among others parameters. In this context, contradictory results using different oxide formation protocols were obtained for pure Cr in sulphuric-based electrolytes (with and without sodium sulphate) by Mott-Schottky measurements [68,69]. If an anodic potential was applied to create an oxide layer, a typical p-type semiconducting behaviour of the Cr oxide was observed [69]. However, if a polished sample was directly used applying a stepwise potential in the less noble direction, a n-type behaviour was obtained [68]. Finally, although photoelectrochemical measurements revealed the presence of a oxide film constituted by an inner p-type Cr oxide and an outer n-type Cr hydroxide layer, it is generally claimed that pure Cr possess an oxide that usually behaves as a p-type semiconductor, having an acceptor density in the range of 10^{19}-10^{21} cm^{-3} depending on the electrolyte [70–72].

Despite having a lot of information about pure Cr, to our knowledge, the semiconducting properties of the oxide layers formed on decorative Cr(III)-based coatings have not been explored. Much more information can be found about bulk materials such as Cr or stainless steel (Fe-Cr alloy). The semiconducting properties of their oxide layers are given by a heterojunction of an internal Cr-rich and external Fe-rich oxide layer in borate buffer electrolyte, respectively [59,60,73].

As a summary, the oxide layers are usually formed after applying a passivation potential for certain time (i.e., electrochemically formed). In addition, not only there is an absence of studies conducted or focused on investigating the semiconducting properties of the native

oxide layers but also coatings from Cr(III)-based electrolyte have not been explored yet. Therefore, a detailed characterisation of the native oxide layer has been carried out in this Ph.D. for coatings obtained for Cr(III)-based electrolytes and a further evaluation of their corrosion capabilities has been done.

1.2 Surface Analysis

Since the decorative Cr coatings are in the nanometre scale, different methodologies and highly surface sensitive equipment have been used for a proper thin film characterisation.

1.2.1 Techniques for thin film characterisation

Usually, the characterisation of the surface is needed to understand the corrosion resistance provided by the coatings; moreover, if certain aesthetic appearance is required such characterisation becomes mandatory. In that sense, from the insanely large number of atoms that there are in a bulk sample, only the outer atoms located at the interphase can participate in superficial reactions with the external medium/environment. Therefore, the investigation of the most superficial features is a key matter because of the surface chemistry and its physicochemical properties. In fact, the surface is governing the type of interactions taking place at the metallic-medium interphase, modifying the corrosion resistance, catalytic activity or even adhesion properties, among others. Currently, it is known that most of the protective properties are conferred by the native oxide or passive film that spontaneously is formed on the top of the Cr electrodeposits [74,75]. This oxide layer is known to be few nanometres thick (2 - 10 nm) so the use of sensitive techniques is a must.

In general, the chemical composition of thin layers can be studied in the solution (*in-situ* method) or after taking away from the electrolyte (*ex-situ* method) [76]. From a theoretical point of view, the use of *in-situ* techniques (e.g., Fourier-Transform Infrared Spectroscopy (FTIR), Raman Spectroscopy, Ellipsometry, etc) [77,78] is preferred because it avoids any surface modification which can occur in the *ex-situ* techniques (e.g., X-ray Photoelectron Spectroscopy (XPS), Auger Electron Spectroscopy (AES), Secondary Ion Mass Spectrometry (SIMS), etc.) during the removal from the aqueous media and the consequent exposure to atmospheric conditions. However, the *ex-situ* methodologies have been widely used because they can provide a very useful and more complete information about the film composition [74].

During the 1970s and '80s, several surface analysis techniques emerged being ones of the most ease to use, useful and realistic tools for *ex-situ* measurements [79,80]. All the different analytical techniques and methodologies operate under Ultra-High Vacuum (UHV) conditions and they mainly differ in the type of particle and/or energy of the primary beam as well as in the particles of the secondary beam. Some examples of the most used and well-known surface analysis techniques are listed below and classified according to the particles involved in the measurement:

i. *Photons in and electrons out*
   X-ray Photoelectron Spectroscopy (XPS), also called, Electron Spectroscopy for Chemical Analysis (ESCA).

ii. *Electrons in and out*
   Auger Electron Spectroscopy (AES).

iii. *Ions in and out*
   Secondary Ion Mass Spectrometry (SIMS) and Ion Scattering Spectroscopy (ISS), also called Low Energy Ion Scattering Spectroscopy (LEIS) for low energy and Rutherford Back-scattering Spectroscopy (RBS) for high-energy.

This work is mainly focused on the use of the *ex-situ* surface analysis techniques, most of them are spectroscopic techniques based on the "beam in, beam out" mechanism. Typically, a primary beam of photons, electrons, or ions penetrates the material to a very superficial depth, depending on the beam characteristics. A second beam, resulting from the interaction of the first beam with the solid matter gets out of the surface and is collected in the detector of the spectrometer. The outgoing beam possesses the information regarding the composition of the material with which the primary beam interacted.

In this section, the fundaments of each technique are briefly described, taking into account their different advantages and disadvantages. In addition, the method to obtain information of the depth through argon (Ar) sputtering is described, as well as some different ways to estimate the thickness of the oxide layer using such techniques.

1.2.1.1 X-ray Photoelectron Spectroscopy/Electron Spectroscopy for Chemical Analysis (XPS/ESCA)

The XPS is based on the photoelectric effect discovered by Einstein. X-ray photons of known energy are irradiated on the sample, typically, they are generated from Al-K_α or Mg-K_α (1486.6 and 1253.6 eV, respectively). As a consequence of the interaction between the

photons and the matter, an electron (photoelectron) of the inner shells of the atom is excited and ejected from its orbital (*Figure 3*). The electrons are not ejected as long as the energy of the incident photon is not higher than the binding energy of that electron (E_b); once that the energy threshold is overcome, photoelectrons are generated whilst the excess of the energy is taken by them as kinetic energy (E_{kin}) [81].
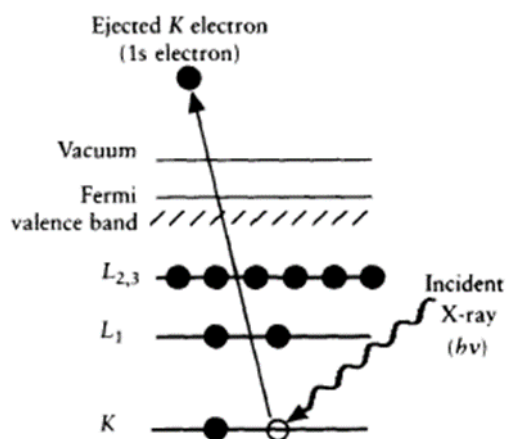
Figure 3. *Scheme of the photoionisation process occurring in the XPS measurements* [82].

The photoelectrons emitted from the surface of the sample are collected at the detector and the analyser determines their kinetic energy. The contact between the sample and the analyser equals their potential and, as a consequence, their Fermi level. This is why is very convenient to use the Fermi level as a reference point for referring to the energy values, since the E_{Fermi} can be set in zero value. So, according to that, the following energy balance can be proposed:

$$E_{kin} = h\nu - E_b - \varphi_{W,det}$$ *(Equation 1)*

Where E_{kin} is the kinetic energy of the photoelectrons that reached the analyser, $h\nu$ is the corresponding energy of the primary used X-ray beam, E_b is the binding energy of the photoelectron, which indeed is the energy difference between the Fermi level and the energy level where the photoelectron has been emitted. This parameter is characteristic of the energy level, the element and its chemical nature or oxidation state. The $\varphi_{W,det}$ parameter is the work function of the detector, which is described by the difference between the Fermi energy level of the analyser and the vacuum level, which in fact is the zero point of the electron energy scale. In practice, the $\varphi_{W,det}$ parameter is not quantified since it can be omitted by calibrating the analyser with a sample such as a gold standard whose binding energy is known [83].

The binding energy represents the force with which the electron interacts with the nucleus. This value increases with the nuclear charge and the distance from the nucleus (orbital s > orbital p). The binding energy is a constant and characteristic value for each electron at a specific energy level of a specific element. However, some shifts in the binding energy may occur as a function of the different chemical nature or by the surroundings elements and their oxidation state. For example, if a C atom is bounded to an O atom, the electronegative behaviour of O will drain some electrons of the bond leaving the C with a formal positive charge. So, the electron of this C will be more strongly attached due to electrostatic effects, having a higher binding energy than a C that is bonded to another C (for example to and aliphatic C-C); this effect has cumulative effect, so the more oxygen atoms bonded to the C the higher shift will suffer its signal. As a general rule and apart from some specific exceptions (final state effects), the more electronegative the neighbour atom is, the higher the binding energy will be (e.g., binding energy of oxide > binding energy of the metal).

The XPS spectra are represented by plotting the intensity or number of counts against the binding energy value. Normally, many peaks can be observed because several photoelectrons of the same atom can be emitted from different energy levels. The qualitative chemical analysis is done by analysing the positions or values of the binding energies of the main photoelectronic peaks; however, other peaks may appear so the identification of the interesting peaks must be done beforehand [84].

The quantification of the elements is made through the quantification of the areas of the peaks which is a complex task that requires a careful data treatment. A previous background correction must be carried out using one of the several mathematical algorithms (e.g., Shirley, Tougaard., etc.). Then a data fitting must be done in order to identify and perform a deconvolution of all the peaks included in the global envelope of the obtained signal. This is usually carried out by adding Gaussian-distributed components with specific mathematical parameters.

XPS results can be also used to estimate the thickness of the native oxide layer according to the studies and calculations developed by Strohmeier and Carlson, which resulted in the following equation [85]:

$$\mathbf{d} = \lambda_0 \sin\theta \left[\frac{N_m \lambda_m I_o}{N_o \lambda_o I_m} + 1 \right]$$

(Equation 2)

Where d is the native oxide layer thickness and it can be estimated knowing the following parameters: the inelastic mean free paths of the metal (λ_m) and oxide (λ_o), their volume density (N_m and N_o), the photoelectron take-off angle (θ) and the area percentages of the metal (I_m) and oxide (I_o), obtained from the quantification of the high-resolution spectra of the metal peak. This approach is valid to estimate the thickness of thin film oxide layers up to 10 nm.

The XPS technique is applicable to both conducting and insulating samples; however, if the conductivity of the sample is not high enough the Fermi levels of the analyser and the sample may not be equalised, leading to misleading values. For solving this issue, most of the modern equipment possesses an accessory called "flooding gun" that bombard the samples with low energy electrons to provide the required conductivity.

Finally, the Angle Resolved X-ray Photoelectron Spectroscopy (ARXPS) is a non-destructive way of modifying the depth resolution of the obtained data (without using Ar etching). Generally, a take-off angle of 45 ^{0} is commonly used in XPS, but when tilting the sample and changing that take-off angle, the penetration of the escaped photoelectrons can be modified, obtaining a more surface or bulk sensitive data (the lower angle, the more surface sensitive). The thickness of the oxide film can also be estimated by using models that take into account the different penetration of the escaped photoelectrons as a function of the modification of the take-off angle [86].

1.2.1.2 Auger Electron Spectroscopy (AES)

AES, as XPS, is also based on the detection of electrons coming from the sample; however, it uses electrons as primary source instead of X-ray photons. The measurement requires a mechanism in which 3 electrons are involved (*Figure 4).* First, an electron from the core (K shell or 1 energy level, E_k) is excited and ejected by using a primary electron source (2 - 10 KeV), as a result, a hole is generated, which is spontaneously filled by the relaxation of a higher energy electron (from the L shell for example, E_L). At this point, there are two possible paths to remove the extra energy of the atom: (i) X-ray fluorescence, emitting the extra energy (E_K - E_L) in form of X-rays or (ii) Auger emission, transferring the extra energy to a neighbour electron of an outer level which is ejected as a result [81]; the latter is the fundament of the AES technique. These are competitive processes with an associated probability related to the atomic number of the irradiated atoms, the Auger emission is more likely in light elements, whilst the heavier elements tend to emit X-ray fluorescence.
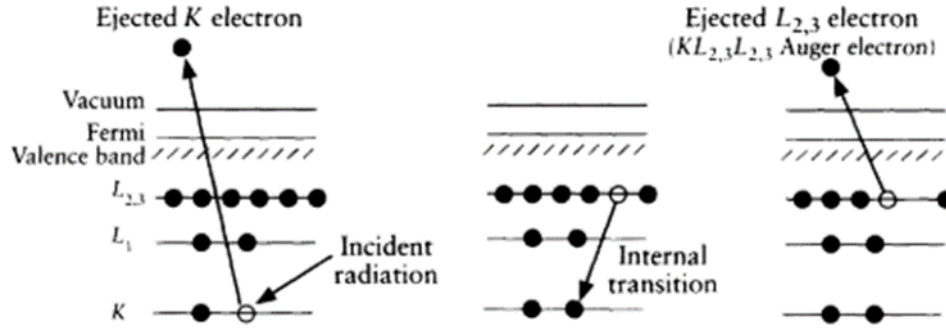
Figure 4. *Scheme of the three electron mechanism of Auger emission* [82]*.*

The data analysis is made through the energy balance of the transition, taking as a reference the Fermi level of the analyser, assigned to zero value. For example, for a WXY transition:

$$\mathbf{E_W - E_X = E_Y + E_{kin} + \varphi_{W,det}}$$ *(Equation 3)*

Where E_W, E_X and E_Y are the binding energy of the electrons at those energy levels, $E_{kinetic}$ is the kinetic energy of the emitted Auger electron and $\varphi_{W,det}$ is the work function of the analyser. AES electrons can be detected in XPS but not the other way round. The kinetic energy of Auger electrons is independent of the primary source, unlike in XPS (*Equation 1*), where the binding energy is dependent of the ion source energy [83].

AES measurements are preferred to be performed on conductive samples because a strong charging effect could be caused by the primary electron beam when analysing insulators. However, as mentioned before, the most modern equipment usually includes a flooding gun to compensate this charging effect, allowing in some cases, to measure insulator samples properly. Auger spectra are often presented versus the kinetic energy of the detected electron, in the first derivate/differentiate form, because auger transitions provide small signals in a steep and noisy background, caused mainly by secondary electrons [87].

1.2.1.3 Secondary Ion Mass Spectrometry (SIMS)

The SIMS technique, usually coupled with a Time-of-Flight (ToF) spectrometer, also called Time-of-Flight Secondary Ion Mass Spectrometry (ToF-SIMS), is a very surface-sensitive tool that can study the chemical composition of both conductive and insulating materials. It operates by bombarding the surface of the sample with a very energetic (1 - 25 kV) focused ion beam (usually Ar^+, C_{60} or SF_6) in UHV conditions, being considered a destructive technique. As a result of such ion bombardment, material from the topmost atomic layers of the target surface is sputtered away by breaking the bonds of the chemical molecules.

Consequently, secondary ions are emitted (*Figure 5*) in form of single atoms or other smaller molecular fragments, in ionic or even neutral states. These ions are guided via an electric field towards a ToF detector that separates them by their mass, based on the time required for them to reach the detector that positioned at the end of the tube [88].
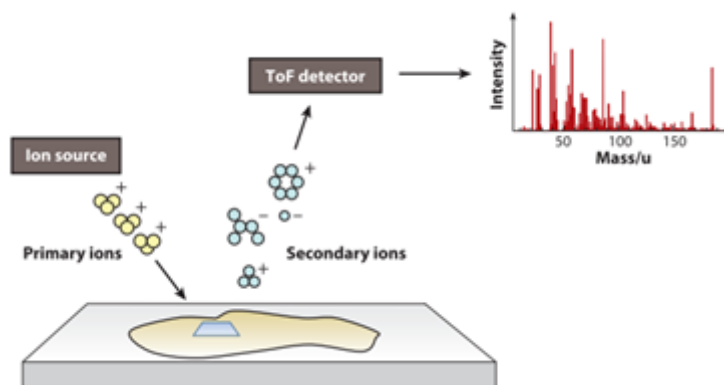
***Figure 5.** Scheme of the ToF-SIMS measurement* [89]*.*

In the ToF analyser, the ejected ions are accelerated into the analyser with a common energy, but at different velocities depending on their particle mass. Due to that different speed, the smaller ions will move through the analyser faster than the larger ones. The mass of the secondary ions, as mentioned before, is determined by their travel time through the analyser, obtaining as a result the SIMS data in form of mass spectra.

The secondary emitted ions are characteristic and directly related to the nature of the atomic and molecular species that originally were present at the topmost monolayer of the surface. So, accurately measuring the masses of the detected secondary ions (thanks to the mass spectrometer detector coupled to the equipment) allows to draw direct conclusions regarding the chemical composition of the original uppermost monolayer of the studied surface, thanks to the use of a fragment database [90].

1.2.1.4 Ion Scattering Spectroscopy/Low Energy Ion Scattering Spectroscopy (ISS/LEIS) and Rutherford Backscattering Spectroscopy (RBS)

Analogously to SIMS, LEIS probes the surface with an ion-based primary source (typically noble gases) and detects the backscattered ions (*Figure 6*). LEIS is an extremely high surface sensitive technique, capable of measuring the chemical composition of the first atomic monolayer, being considered one of the most surface sensitive surface analysis technique among all the techniques described so far in this section [91]. Due to this higher surface sensitivity, hydrocarbons that have been adsorbed from the atmosphere during transport must usually be carefully removed from the samples to avoid any masking effects.

When these low energy ions interact with the surface, some of them are scattered whilst others penetrate and enter into the solid matter, when this happens the ions are neutralized and travels through the solid in an uncharged form. As they move through the material, they lose energy as a consequence of the multiple collisions that take place, at the same time that several electron interactions may occur in the material. At some point, a backscattering event can occur which reverses the trajectory of the atom and directs it out of the solid. But if a neutral atom leaves a solid, the LEIS instrument will have no way of detecting it. Fortunately, it turns out that when neutral noble gas atoms leave a solid, a fraction of them are reionised and can be detected. The resultant energy of the backscattered ion can provide chemical information about the surface as it can be directly related to the mass of the surface atom. As a result of these effects, LEIS provides a single-atomic-layer mass spectrum of the surface of the material, allowing the element identification.

The use of different noble gas ions lead to different sensitivities to surface atoms with different masses, generally, heavier atoms are generally better analysed by heavier probe ions (e.g., Ne^+, Ar^+, Kr^+) whilst in contrast, lighter ions (He^+) can resolve nicely the lighter elements, being less effective at resolving the heavier ones [92].
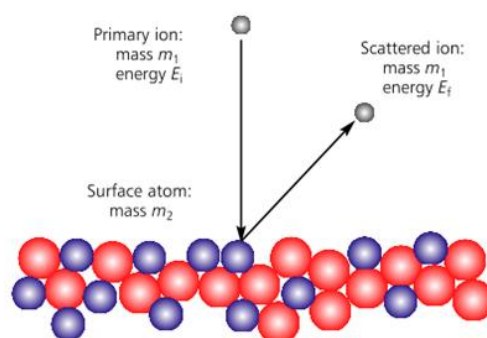
Figure 6. *Scheme of the ion scattering phenomenon occurring in LEIS* [93]*.*

RBS is just the high-energy version of LEIS, having the main difference in the penetrated depth (higher energy, higher penetration). Thus, the technique becomes more bulk-sensitive allowing the investigation of the chemical composition of deeper layers in a non-destructive way, since no destructive depth profile is performed [94].

Even if all the techniques described above are included in the same surface analysis family, all of them possess special and unique features that differentiate them one from the other. For example, the depth analysis or sampling area differs as it is function of the type of particle and energy of the incident beam, as well as the materials that can be studied. Because of that, usually different techniques are used in the investigations in order to obtain

complementary information, because normally, no single technique provides enough information to answer to a complex question when studying such thin films. The *Table 4* summarises some of the general features of the techniques mentioned above, as well as their special or unique characteristics.

Table 4. *Characteristics of some of the most common surface analysis techniques* [95,96].

Parameter	*XPS*	*AES*	*SIMS*	*ISS*
Primary radiation	Photons	Electrons	Ions	Ions
Secondary radiation	photoelectrons	Auger electrons	Secondary ions	Secondary ions
Analysed depth *(atomic layers)*	3 - 15	2 - 10	2 - 10	1 - 2
Detection limit *(% atomic layers)*	0.1 - 2	0.1 - 1	10-4 - 1	0.1 - 1
Quantitative analysis	Yes	Yes	Limited *(standards required)*	Partially
Special features	Detection of oxidation states	Higher spatial resolution	Higher sensitivity	Higher depth resolution

1.2.1.5 Depth profile using surface analysis techniques

The primary beam of the spectroscopic techniques above can penetrate few micrometres in the sample; however, the secondary produced beam can only travel a specific distance, called the attenuation length or the inelastic mean free path (λ), without suffering any inelastic collisions (function of the kinetic energy of the electron and the element). So, only the secondary particles that are coming from a depth less than the escape depth will not lose energy and will reach the detector (being part of the main peaks of the resulting signal in the spectra), whilst the others will suffer inelastic collisions losing all their energy or contributing to the background noise if they managed to arrive to the detector [83].

Regarding the depth information, it is usually interesting to complement superficial information with some knowledge of the layers that are underneath. This can be addressed in practically any surface analysis technique by using a coupled etching ion gun (normally based on Ar^+). Thus, the sample is destructively bombarded, independently of their primary beam, removing as a result some topmost atomic layers in such a way that a depth profile can be carried out by measuring sequentially whilst the sputtering goes on [81]. This allows to determine the chemical distribution as a function of the depth or even to estimate the thickness multilayers systems. Although such thickness is removed during depth profiles, it can be estimated as follows: the equipment is required to be previously calibrated using a

standard SiO_2 wafer to know the sputter rate of the specific equipment. Then, the sputter rate can be correlated by using relative correction parameters in order to transform the sputter rate corresponding to the SiO_2 standard to other metals or systems [97].

1.2.1.6 Spectroscopic Ellipsometry (SE)

In addition to the chemical composition of the Cr layer and its oxide layer, the thickness and homogeneity of the latter might be considered to be studied in order to evaluate their corrosion protection capabilities (typically the more homogeneous and thicker, the better for corrosion protection).

The spectroscopic ellipsometry is a contactless and non-destructive technique to study thin films, which is based on the change of the polarisation state that the light suffers when interacting with a material [98]. Analysing the changes in the polarisation state allows to determine parameters such as thickness and optical constants, as well as the chemical composition, crystallinity, anisotropy and uniformity in a more indirect way. The resolution of the thickness determination is ranging from the few angstroms to tens of microns [99]. The final output is obtained through mathematical modelling of the signal.

1.2.1.7 Transmission Electron Microscopy (TEM)

TEM is a microscopy technique in which a beam of electrons is transmitted through an ultra-thin sample. The interactions between the electrons and the atoms can be used to observe features such as the crystal structure or structure dislocations and grain boundaries. TEM can also be used to perform chemical analysis to study the growth of layers, their composition and defects in semiconductors. High resolution measurements can be used to analyse the quality, shape, size and density of quantum wells, wires, and dots. Sample preparation procedures are usually required (e.g., mechanical thinning or ion milling). If the sample is properly prepared, the measurement of the oxide thickness could be directly performed from the obtained microscopic image.

TEM is considered one of the most powerful techniques for determining thin film thickness because it measures the real thickness instead of obtaining data based on indirect calculations or assumptions, for this reason it is not necessary to build models that can conduct to subjective results, as most of the methods [100].

1.2.1.8 X-Ray Reflectivity (XRR)

When visible electromagnetic waves interact with a surface, the radiation is specularly reflected (same angle than incident one), diffusively reflected and refracted. In the case of

X-rays, total reflection occurs when the incident angle is smaller than the critical angle. Thin-film parameters can be determined, including thickness, density and surface or interface roughness by measuring the reflection intensity curves from grazing incident X-ray beams. The obtained results are analysed by fitting the measured data to a simulated curve, which is calculated using the recursive Parratt's formalism combined with the rough interphase formula [101]. In this way:

- The interference between the layers is observed as an oscillating signal (Kiessing fringes). The oscillation depends on the film thickness, thicker films present shorter periods of oscillations.

- The amplitude of the oscillation and the critical angle for total reflection provide information about the density of films. The amplitude shows the difference between the densities of the thin film and its substrate. The larger the oscillation, the larger density difference.
- The larger the roughness of a film, the faster the decay rate of its X-ray reflectivity and the larger interface roughness, lower oscillations.

1.2.1.9 Synchrotron radiation-based X-ray absorption spectroscopy (XAS)

The X-ray absorption spectroscopy (XAS) technique allows the study of atomic local structure and electronic states, as well as the elucidation of the chemical composition of individual elements in an alloy; this is carried out by studying energy shifts in the core and valence electron states as a result of the interactions of the X-rays photons with the surrounding atoms. XAS measurements require high intensity as well as coherent and tunable X-ray beams over a wide energy range; therefore, such measurements are usually carried out in synchrotron radiation facility.

A synchrotron is an accelerator of electrons that can produce synchrotron-based radiation; a scheme of such facility is shown in *Figure 7*. Electrons emitted by an electron gun are first accelerated in a linear accelerator and then transmitted to a circular accelerator where they continue increasing their velocity until finally reaching a certain high energy level. These high-energy electrons are then injected into a circular storage ring where they circulate in a vacuum environment at a constant energy for many hours. Afterwards, the electrons are accelerated and deviated in the storage ring by different magnetic components to generate the desired electromagnetic radiation, since the frequency of synchrotron radiation can cover the entire electromagnetic spectrum. When necessary, the radiation is guided

towards the experimental analysis rooms of the different beamlines, also called *endstations,* which are located tangentially to the storage ring in order to interact with the sample and perform the desired experimental measurement. Each beamline is designed for a specific type of research or for being used with a specific technique [102].
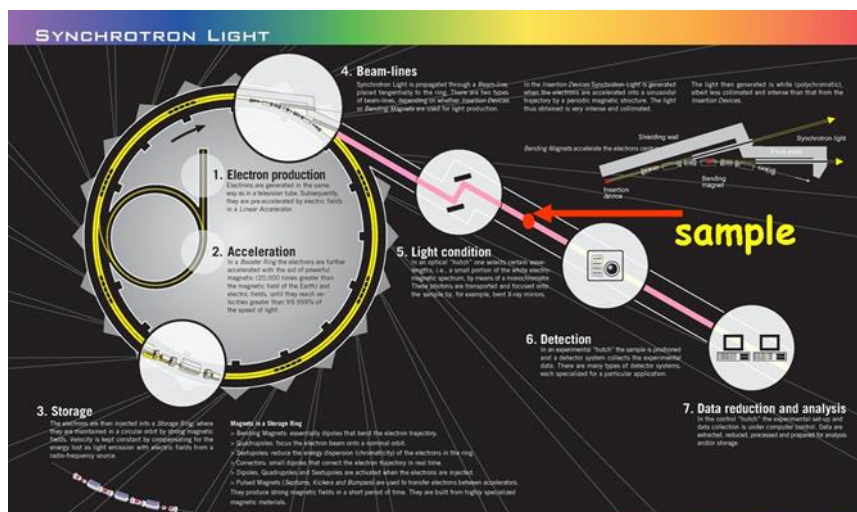
Figure 7. *Scheme of the radiation production process in a synchrotron accelerator facility* [103]*.*

The synchrotron radiation is featured for being able to provide X-ray photons with a million times higher intensity than a conventional X-ray tube. Moreover, it can be also tuned by using several slits, attenuators, crystal monochromators and mirrors that can allow controlling precisely parameters such as the bandwidth, photon flux, beam dimensions, focus and collimation. Thus, using synchrotron radiation becomes crucial to provide the proper scenario required to investigate these nanometric coatings and very thin oxide films, as well as, to resolve the possible limitations that can be found when using conventional techniques (e.g., energy resolution, sensibility, depth analysis, etc.).

Regarding to XAS technique, it is based on the same primary beam than XPS since X-rays are irradiated to the sample. As a consequence of the interaction of such X-ray photons with the matter the photoelectric effect takes place ejecting a photoelectron and leaving the atom in an excited state with an empty core-level hole. As explained before, the atom is relaxed immediately by the competition of two mechanisms: X-ray fluorescence and Auger emission [104,105]. In XAS no secondary generated beams are studied since it is based on the absorption effect of X-rays. Such measurements are made through the calculation of the absorption coefficient on the basis of the Lambert-Beer law. Therefore, the absorption coefficient can be determined by measuring the ratio between the incident and transmitted

photon intensity; there are two ways of making such measurement (depending the sample and the required accuracy level): monitoring the intensity of the (i) transmitted or (ii) fluorescent X-rays. Generally, transmission mode is preferred due to its ease and accuracy, whilst the fluorescence mode is more suitable for analysing low concentrated or more dilute samples [106].

Typically, the absorption coefficient decreases as a function of the energy of the incident X-ray photons and, at specific energies, abrupt discontinuities can be observed (the so called absorption edge), which represents the absorption of a photon and the consequent excitation of the core-electron [107,108]. The study of the absorption edge can provide additional information apart from the elemental identification as they contain a fine structure that, if analysed, can provide complementary electronic and structural information.

Different regions are distinguished in XAS, having the absorption edge as a reference (*Figure 8*): (i) X-ray Absorption Near Edge Structure (XANES or also called NEXAFS) and (ii) Extended X-ray Absorption Fine Structure (EXAFS). Whilst XANES gives information on the oxidation state, three-dimensional geometry, and local electronics of the elements, EXAFS provides information on the local geometry of the surrounding and nearest neighbouring atoms [88].
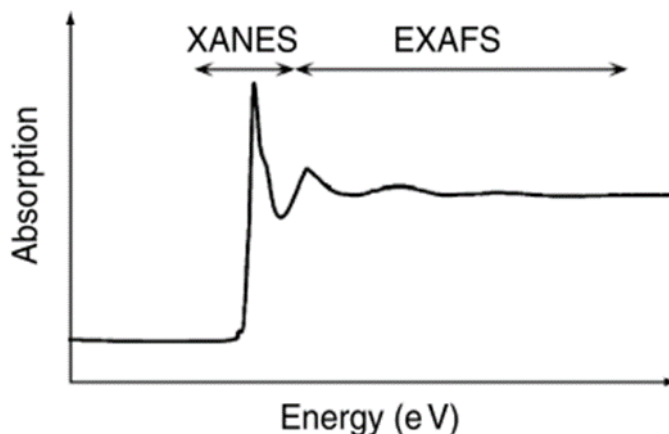
Figure 8. *Illustration of the XAS regions of interest: XANES and EXAFS* [107]*.*

Every element with a given electronic structure, surrounding atoms and phase, has a signature XANES spectrum, in fact, changes of the charge of the ions produce big chemical shift. Therefore, the use of standards for using a "fingerprinting" approach (measuring standards and comparing/matching their signals with the signal of the samples) can be a good methodology in order to identify the chemical components and oxidation states of the elements present in the sample.

1.2.2 Other complementary techniques

Despite the highly surface sensitive techniques described in the previous section, there are several other techniques that can study surfaces and provide useful complementary information when studying thin films.

1.2.2.1 Scanning Electron Microscopy (SEM)

SEM is a technique for high-resolution imaging of surfaces. It uses a focused beam of high-energy electrons that scan the surface of the samples and generates an image by detecting the emitted electrons. The signals that derive from the electron-sample interactions reveal information about the sample including external morphology, chemical composition, and crystalline structure and orientation of the materials that are present in the sample [109]. In most applications, data are collected over a selected area of the surface of the sample, and a two-dimensional image is generated that can displays spatial variations. SEM is also capable of performing analyses of selected local points on the sample when coupling with an Energy Dispersive X-ray analyser (EDX). This approach is especially useful for the qualitative or semi-quantitative determination of the chemical composition of surfaces [110]. The crystalline structure and crystal orientations can also be studied when coupling the microscope with a Backscattered Electron detector (BSE).

1.2.2.2 Profilometry

A stylus profilometer can measure the surface profile with the aim of characterising the roughness. Such profilometers are constituted by a mechanical probe or tip, which make direct contact with the surface, allowing the monitoring of the topography of the samples as the function of the scanning axis [111]. The vertical motion of the probe is turned into height information by a transducer that transforms the vertical motion into electrical signals, representing the surface profile. Thus, the roughness of the surface can be determined by using specific software.

1.2.2.3 X-ray Fluorescence (XRF)

This technique is similar to the EDX of the SEM because it irradiates the sample with X-rays, exciting and ejecting consequently electrons from the inner shell of the atom. This destabilises energetically the atom and the equilibrium is restored through the relaxation of electrons that are located at higher energy levels. In this relaxation process the excess of energy is released by the emission of X-ray fluorescence. The energetic difference between the ejected electron and the one that is relaxed (energy of the emitted X-ray photon) is characteristic of each chemical element, so the energy of the X-ray fluorescence is directly

related to the chemical element that is being studied [109]. Furthermore, most of the equipment can be calibrated with standards in order to determine simultaneously the chemical composition (of the bulk) and the thickness of multilayers systems, if suitable standards are used.

1.2.2.4 X-ray Diffraction (XRD)

XRD analysis is based on constructive interference of monochromatic X-rays and a crystalline sample. The X-rays are generated by a cathode tube, then they are filtered to produce monochromatic radiation and finally are collimated to concentrate and direct the X-rays towards the sample. The interaction of the incident X-rays with the sample produces constructive interference (and a diffracted beam) when the experimental conditions satisfy the Bragg's Law. This law relates the wavelength of the electromagnetic radiation to the diffraction angle and the spacing lattice in a crystalline sample. The characteristic X-ray diffraction pattern generated in a typical XRD measurement provides a unique "fingerprint" of the crystalline elements present in the sample [112]. When properly interpreted, by comparison with standard reference patterns and measurements, these fingerprints allow, among other applications, the identification of the crystalline phases of the elements present in the sample.

1.3 Semiconducting properties

Different methodologies and approaches were used for the study of the semiconducting properties of the oxide layers formed on top of the Cr electrodeposits.

1.3.1 Mott-Schottky

The Mott-Schottky analysis is proved to be a powerful methodology for *in-situ* analysis of oxide layers formed on metals and alloys. Mott-Schottky analysis is based on the fact that the oxide layers act like a semiconductor, so their semiconducting properties can be measured. According to the Mott-Schottky theory, the semiconducting properties of oxide films can be studied by measuring the capacitance of the interphase layer developed in the oxide film, i.e., the space charge layer (a double layer formed next to the outer part of the oxide) and the Helmholtz layer (double layer formed in the electrolyte near the oxide), as a function of the applied electrode potential when the electrode is immersed in an electrolyte. The experimental measured capacitance of a film can be described as [113,114]:

$$\frac{1}{C} = \frac{1}{C_{sc}} + \frac{1}{C_H}$$

(Equation 4)

Where C_{sc} is the capacitance of the space charge layer and C_H the capacitance of the Helmholtz layer. The Mott-Schottky approach assumes that the space charge capacitance is significantly lower than the Helmholtz capacitance ($C_{sc} <<< C_H$), so the $1/C_H$ parameter is assumed to be insignificantly low and consequently neglected in the *Equation 4*; as a result, the measured capacitance is assumed to be the capacitance of the space charge layer [65]. Therefore, the oxide film/electrolyte interphase may be described by the followings Mott-Schottky relations when the semiconducting film (oxide layer) is polarised at the depleted state [66,115,116]:

$$\frac{1}{C_{sc}^2} = \left(\frac{-2}{e\varepsilon\varepsilon_0 N_A}\right)\left(E - E_{fb} + \frac{k_B T}{e}\right)$$

Equation 5
for p-type semiconductors

$$\frac{1}{C_{sc}^2} = \left(\frac{2}{e\varepsilon\varepsilon_0 N_D}\right)\left(E - E_{fb} - \frac{k_B T}{e}\right)$$

Equation 6
for n-type semiconductors

Where ε is the dielectric constant of the oxide film, ε_0 is the vacuum permittivity (8.85×10^{-14} F cm^{-1}), *e* is the electron charge (1.602×10^{-19} C), E is the applied potential (V), E_{fb} is the flatband potential (V), k_B is the Boltzmann constant (1.38×10^{-23} J K^{-1}) and N_A/N_D are the charge carrier density (N_q) in the oxide layer, acceptor or donor respectively (cm^{-3}).

The application of the Mott-Schottky theory allows the determination of the semiconductor type and the main charge carriers, as well as the quantification of such carrier density and the flatband potential. The charge carriers are donors or acceptors species (depending of the semiconductor type), which in fact are point defects in the oxide layer that include different ion vacancies or interstitials. Typically, oxygen vacancies and cation interstitials are the main charge carriers in n-type semiconductors whilst cation vacancies are the main carriers in p-type semiconductors [117,118]. Generally, a lower donor or acceptor densities restrains the electron transfer at the oxide/electrolyte interphase, inhibiting electrochemical reactions and decreasing the oxide film dissolving or metal oxidation. In contrast, a high charge carrier density will lead to higher currents values, facilitating the oxide dissolution [118,119]. The flatband potential represents a region where predominant electronic defects establish the transition between p and n-type semiconductor; it determines the position of

the energy bands with respect to the redox potential of the electroactive ions present in the electrolyte.

1.3.2 Point Defect Model (PDM)

Although here are several theories and models to describe the passivity [120], nowadays the PDM, developed by Macdonald and co-workers [62,121], is perhaps the most well-known to study the growth and breakdown of passive films in order to understand their protection capabilities. As it was mentioned above, the oxide layers are generally considered highly disordered and defective oxide layers that contain point defects (metal and oxygen vacancies and cation interstitials according to the previous section). According to the PDM, the transport of such dopants through the oxide film is involved in the growth and breakdown of the oxide layer [122,123]. Anion vacancies and cation interstitials are created and consumed at the metal/film and film/electrolyte interphases respectively; whilst cation vacancies are created at the film/electrolyte interphase but are consumed at the metal/film interphase. The formation and annihilation of anion vacancies contribute to the film growth and cation vacancies contribute to the metal dissolution. So, the passivity breakdown is closely related to the concentration of cation vacancies at the metal/film interphase, and hence related to the flux of cation vacancies through the film [124]. Consequently, the first assumption of this model lies in the fact that the transport of point defects within the oxide film under the influence of both a concentration gradient and an electrical potential gradient, is necessary for the processes of film growth and breakdown. Another important assumption of the PDM is that the electric field strength across the film depends on the chemical and electrical properties, being independent of the applied potential and film thickness.

A key parameter when describing the transport of point defects or the kinetics of oxide film growth is the diffusion coefficient of the point defects. Such diffusivity parameter can be determined studying the dependency of the charge carrier density of the oxide layer as a function of the oxide film formation potential, using Mott-Schottky analysis in conjunction with the PDM. This kind of measurement requires the electrochemical formation of the oxide films at different passive potentials under controlled conditions in order to quantify the charge carrier density (by Mott-Schottky analysis) of each passive film, formed at different potentials; the native oxide layer is previously removed to provide a reproducible surface for the electrochemical oxide formation. Then the obtained results are fitted to the following exponential function [125,126].

$$\mathbf{N_q} = \boldsymbol{\omega_1} \cdot \mathbf{e^{-bE}} + \boldsymbol{\omega_2} \qquad \textit{(Equation 7)}$$

Where ω_1, ω_2 and b are unknown constants, N_q the calculated charge carrier density (acceptors or donors) from the Mott-Schottky analysis and E is the applied potential (V) used in the electrochemical oxide film formation.

Consequently, the diffusion coefficient can be calculated using the following equation:

$$\mathbf{D_0} = \frac{\mathbf{J_0}}{\mathbf{2K\omega_2}} = \frac{\mathbf{J_0RT}}{\mathbf{2F\omega_2k_e}} \qquad \textit{(Equation 8)}$$

Where:

$$\mathbf{J_0} = -\frac{\mathbf{i_{ss}}}{\mathbf{2e}} \quad \textit{(Equation 9)} \qquad \text{and} \qquad \mathbf{K} = \frac{\mathbf{k_eF}}{\mathbf{RT}} \qquad \textit{(Equation 10)}$$

being D_0 the diffusivity coefficient of the charge carriers *(cm^2 s^{-1})*, J_0 the calculated flux of charge carriers (A cm^{-2} C^{-1}), R the ideal gas constant (8.31 J K^{-1} mol^{-1}), T the temperature (K), F the Faraday constant (96485 C mol^{-1}) and k_e the electric field of the oxide film (typically considered 10^6 Vcm^{-1} [69]), e is the electron charge constant (- 1.6x10^{-19} C) and i_{ss} the determined mean value of the steady state passive currents (A cm^{-2}) obtained during the potentiostatic growth of the oxide layer.

1.4 Corrosion resistance properties

As it was mentioned before, the corrosion protection properties of Cr are well known to be conferred by the passivity of the native oxide layer that is spontaneously formed on their surface. In order to distinguish the key role of the oxide film, it is interesting not only to study the overall corrosion performance of the coating itself but also to try to isolate and evaluate the corrosion resistance of the oxide layer instead. Several conventional electrochemical techniques and methodologies are used for such characterisation.

1.4.1 Corrosion evaluation

Outdoor natural exposure, accelerated and electrochemical (conventional and localised) tests are the most common methodologies used to study aqueous corrosion of metals. Electrochemical techniques allow the study of the anodic (oxidation) and cathodic (reduction) reactions occurring on the metals at laboratory level in a controlled ambient and in a non-destructive or destructive way (depending on how much the system is disturbed

electrochemically). Thermodynamic and kinetic parameters can be obtained after evaluating/quantifying the performance of the samples under different aggressive environments (i.e., electrolytes), monitoring corrosion events with time, etc.

1.4.1.1 Accelerated corrosion tests

This type of corrosion tests can provide information of the corrosion resistance very quickly (usually from days to 1 - 2 months) in comparison to outdoor exposure tests or *in-situ* exposure during their use in their final applications (which will take years). Although the later provides reliable information about the lifetime before failure under real service conditions, such tests are very time-consuming. Accelerated corrosion tests offers an alternative of simulating aggressive environmental conditions, which in fact, are widely used in the industry as quality control test to validate the corrosion resistance performance of the samples, due to the speed of the measurement.

One of the most common accelerated corrosion tests is based on exposing samples to a fog inside a chamber under controlled temperature, they are known as salt spray tests and typically worked under the standard B117 [127]. The *Table 5* shows the conditions and electrolytes of some of the different tests that are used in order to simulate different corrosive environments [128].

Table 5. *Conditions of the salt spray tests, in accordance with the ISO 9227:2017* [129].

	Neutral Salt Spray (NSS)	Acetic Acid Salt Spray (AASS)	Copper-Accelerated Acetic Salt Spray (CASS)
Temperature (º C)	35	35	49
pH (adjusted with acetic acid)	6.5 - 7.2	3.1 - 3.3	3.1 - 3.3
NaCl (%)	5	5	5
$CuCl_2$ (%)	-	-	0.0205

The evaluation of the corrosion performance in such accelerated corrosion tests is carried out by periodic visual inspection of the surface appearance [130]. According to the visual examination, a semi-quantitative evaluation is done in which samples can pass the test only if they are not showing defects on the surface. However, the use of this kind of accelerated corrosion tests still presents some drawbacks, such as the reproducibility between specimens, the not short enough testing periods, the subjectivity during evaluation of the results and the lack of information about the reasons for passing or failing the test.

1.4.1.2 Open Circuit Potential (OCP)

The OCP provides information of the working electrode (i.e., sample to study) in a specific medium (electrolyte) with respect to a reference electrode in a two-electrode configuration cell when no external current is applied (open circuit). In fact, the OCP is a non-invasive measurement (without application of any external potential or current) at which the oxidation and reduction reaction rates are in equilibrium in a particular environment. Despite this parameter corresponds to the equality of reaction kinetics, it is usually used to discuss the thermodynamic trend of the sample to participate in electrochemical reactions (corrosion) with the electrolyte or surrounding media [131], where in general it is considered that a metal with a higher OCP is expected to be less prone to suffer corrosion reactions (more noble), whilst a lower OCP is a feature of metals with a higher trend to be oxidised (less noble). Studying the OCP variation as a function of the immersion time in a electrolyte can also provide some insights about the corrosion resistance behaviour of the studied samples; for example if the OCP increases with the time it could indicate that the surface is becoming passive due to the formation/growth of a protective oxide layer as a result of the exposure of the metal to certain electrolytes. In contrast, when the OCP decreases with time it is generally considered that the metal is being attacked [132].

Usually, samples are exposed to the electrolyte and the OCP is monitored until the system reaches an equilibrium. Although it depends on the couple system-electrolyte, typically 5 mV variation in several minutes is considered stable.

1.4.1.3 Linear Polarisation Resistance (LPR)

The LPR measurements are used for the calculation of the polarisation resistance (R_p), a widely used parameter for evaluating the corrosion performance and even for estimating the corrosion rate [133,134]. This technique is based on the mixed potential theory which claims that the cathodic and anodic reactions in a corrosion process at the metal-electrolyte interphase take place at a mixed or corrosion potential, so that the sum of all cathodic reaction rates equals the sum of all anodic reaction rates.

In a LPR experiment, typically, the current is measured as a result of sweeping the potential over a very small range and close to E_{OCP}, typically ± 10 mV vs E_{OCP}. Then a linear E vs i relationship is obtained and the R_p can be determined from the slope by applying the Ohm's Law.

1.4.1.4 Potentiodynamic polarisation curves (PDP)

Potentiodynamic polarisation curves measurements, unlike the OCP, are based on shifting the system from the equilibrium (i) by applying a potential and monitoring the current density (potentiostatic) or (ii) by applying a current and monitoring the resulting potential (galvanostatic). Potentiodynamic polarisation curves (referred as potentiostatic measurements) are obtained by pushing away the sample from the equilibrium (the sample it is polarised). As a result, the anodic or cathodic reaction rates can be modified, providing information about features such as passivation, pitting potentials or even current limiting values that are governing the corrosion process.

Aqueous corrosion events are electrochemical reactions that generally are controlled by the kinetics of the electron transfer reaction at the metal surface, which obeys the Tafel equation. Since a corrosion system is constituted by an anodic and a cathodic reaction, assuming that there are only two half reactions and combining their Tafel equations, the Butler-Volmer equation is formed [135]:

$$i = i_a + i_c = i_{corr}\left(e^{(2.3(E-E_{OCP})/\beta_a)} - e^{(-2.3(E-E_{OCP})/\beta_c)}\right) \qquad \textit{(Equation 11)}$$

Where, i is the measured current density, i_{corr} the corrosion current, E the applied potential, E_{corr} the corrosion potential and β_a/β_c the respective anodic and cathodic Tafel coefficients.

The Butler-Volmer equation (*Equation 11*) describes the electrochemical behaviour, providing zero current at the E_{OCP} and obtaining a total current contributed by cathodic and anodic reactions at potentials near E_{OCP}, having predominant contribution of one of them when applying potentials far from the equilibrium. The Tafel plot is generated when plotting the log I vs E in such a way that the corrosion current can be obtained graphically by extrapolating the linear sections of the cathodic and anodic branches. The corrosion current can also be calculated resolving numerically the resulting Butler-Volmer equation, by using mathematical software. However, a further simplification can be performed on the equation when restricting the equation to potentials close to E_{OCP} having as a result the Stern-Geary equation [136]:

$$i_{corr} = \frac{\beta_a\beta_c}{2.3R_p(\beta_a+\beta_c)} \qquad \textit{(Equation 12)}$$

Where, R_p is the polarisation resistance, a parameter that can be calculated from a LPR experiment (previous section). The Tafel coefficients (β_a/ β_c) can be determined from the slope of the linear regions of the anodic and cathodic branches in the corresponding Tafel plots.

It should be stressed that both the Tafel and Butler-Volmer equations are usually used for system controlled by charge transfer and cannot be used straightforward when dealing with passive metals like Cr due to the presence of the passive regions (current plateau as a function of the potential. In such cases, the corrosion resistance can be evaluated based on other electrochemical parameters characteristic of passive metals, like for example the current value of the passive region, also kwon as the passivation current (i_{pass}), which can provide insights about the stability of such systems [137,138].

1.4.1.5 Electrochemical Impedance Spectroscopy (EIS)

The EIS has been proven to be one of the most powerful non-destructive electrochemical techniques for both fundamental and applied research. It is normally used for studying corrosion mechanisms, kinetics of electrochemical reactions, adsorption phenomena, or for evaluating corrosion inhibitors [139].

The impedance (Z) is the equivalent of the resistance but in an Alternating Current (AC) circuit rather than in Direct Current (DC). The concept of resistance is the ability of an electrical circuit to resist the flow of electrical current. The well-known Ohm's Law defines the resistance as the ratio between the potential and the current (R= E/I), but this is valid when considering only one circuit element: resistors. In fact, this is a simplification since in the real world there are several factors that can impede the electron flow in an electrochemical cell, for example, geometrical aspects like defects or pores, different kinetics of reactions, diffusion of ions, etc. All of them can be considered to behave like resistors, capacitors and inductors, i.e., equivalent circuits of AC. In this way, in AC the resistance is now substituted by the impedance, which in fact is a complex number, as well as frequency-dependent [140,141].

The electrochemical impedance is measured by applying a small sinusoidal AC potential and measuring the resulting sinusoidal AC current. The applied potential perturbation and the generated current are different in amplitude and phase which according to mathematical transformations can be described by complex numbers, having the impedance a real (Z') and imaginary part (Z''), as it is shown in the next equation [141]:

$$Z\left(\omega\right) = Z'\left(\omega\right) + jZ''\left(\omega\right)$$

(Equation 13)

Due to the complex nature of the impedance, EIS data can be plotted in different ways (*Figure 9*), the most popular ones are (i) the Nyquist plot, real component (Z') vs. imaginary component (Z") and (ii) the Bode plot, impedance modulus IZI vs. frequency, or impedance phase angle vs. frequency.
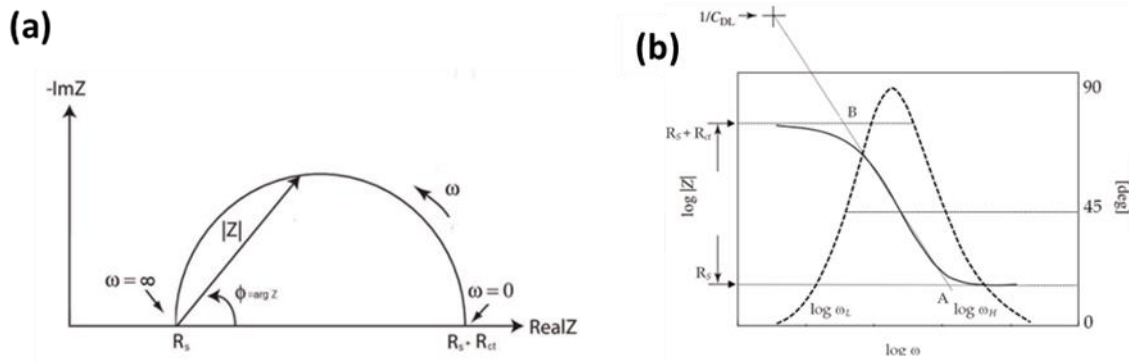
Figure 9. *Example of (a) Nyquist and (b) Bode plots for the EIS data presentation* [142].

The data obtained from EIS measurements is commonly analysed by fitting the obtained signals to an equivalent electrical circuit model built by combination of the already mentioned electrical elements. For example, most of the more common studied systems can be modelled by using a basic Randle equivalent circuit (*Figure 10*) where a resistor is used for defining the resistance of the solution (R_s) together with a parallel combination of another resistor which usually described the charge transfer resistance (R_{ct}) and a capacitor to represent the electrochemical double layer capacity (C_{dl}), formed as a result of adsorbed ions on the surface.
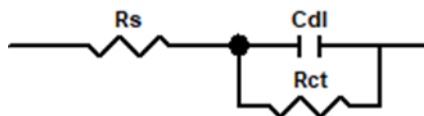
Figure 10. *Basic Randle equivalent circuit for EIS data fitting.*

Additionally, such capacitance values can be also used to estimate the thickness values (e.g., thickness of an oxide layer) using the following equation:

$$C = \frac{\varepsilon\varepsilon_0}{\delta}$$

(Equation 14)

Where C is the measured capacitance, ε is the dielectric constant of the oxide layer, ε_0 is the vacuum permittivity (8.85×10^{-14} F cm^{-1}) and δ is the thickness of the capacitor.

1.4.1.6 Critical chloride content

The critical chloride content is the chloride concentration threshold (C_{crit}) which is defined as the minimum amount of chloride ions that are required at the electrolyte-oxide interphase to initiate the depassivation and breakdown of the oxide film. Initially, this methodology was commonly used for the study of the corrosion caused by chlorides ions in steel rebars that are contained in concrete [143]; however, it is also suitable for the evaluation of the corrosion resistance of oxide films.

In such measurements, the breakdown of passivation is determined due to the action of chloride anions. This methodology lies in monitoring a specific electrochemical parameter (e.g., E_{OCP}, pitting potential, passivation current, corrosion current etc.) and studying its variation as a function of the chloride concentration in the electrolyte [144], an example is shown in the *Figure 11*. Usually, the value of the selected parameter is constant with the lower chloride concentrations until certain threshold, in which a dramatic change of the value is observed, due to the breakdown of the oxide film, caused by the chloride ions.
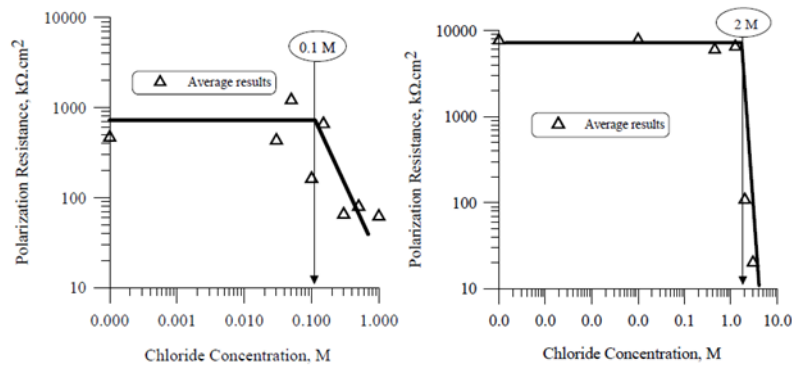
Figure 11. *Example of the critical chloride content methodology* [145]*.*

1.4.1.7 Passivation kinetics or current-time transients

One of the most characteristic features of protective oxide layers is the fast speed they show during their formation, granting to the metals with a unique "autorepairing" ability. Therefore, the study of the kinetics of such oxide films formation is a matter of interest and of great importance when investigating such oxide layers.

The growth kinetics of anodic oxide films usually starts with the chemisorption of hydroxyl ions (OH$^-$), which as a result of exchanging reactions with the metal ions in the surface,

forms oxide molecules. Further reactions yield to monolayers, homogeneous multilayers, or thick islands of oxides, depending on the ratio of lateral to normal growth. In the case of protective oxide films, usually homogeneous films with almost constant thickness are formed, even if local inhomogeneities may cause slight thickness changes [146]. The growth rate is equivalent to the current density of the oxide formation, which will depend on the electrode potential E, the time t, and the concentration of OH⁻.

In this way the passivation kinetic can be monitored according to the following equation [147]:

$$\mathbf{i(t) = A \cdot t^{-n}}$$

(Equation 15)

Where i(t) is the current density of the oxide film at certain t time, A is a constant and n is the passivation index. The latter parameter is an indirect way of measuring the oxide film formation velocity and it can be determined from the slope of the log i vs log t of the logarithm form of the previous equation:

$$\mathbf{\log i\,(t) = \log A - n \cdot \log t}$$

(Equation 16)

Typically, the *n* value varies in the range 0 - 1 in such a way that the higher this parameter is the faster the oxide layer formation is. Furthermore, its value also describes the type of oxide layer since oxide films with values similar close to 1 have been found to be compact, as well as highly protective. In contrast, *n* values ≤ 0.5 are characteristic of porous and less protective oxide layers [148–150].

Analogously to the PDM measurements, electrochemically formed oxide layers are studied in this methodology to have a reproducible surface for each test, so prior to performing the current time transient measurement the native oxide layer is usually removed. It must be taken into account that when applying a constant potential within the passive region, despite the oxide film formation, the current density can also be consumed by other events such as metal dissolution that compete with the oxide layer formation. Therefore, when measuring the current density under potentiostatic conditions the current evolution will indicate which event is predominantly taking place as a function of the potential application time. As it is illustrated in *Figure 12*, typically, 3 steps or stages can be identified during a current-time transient measurement.
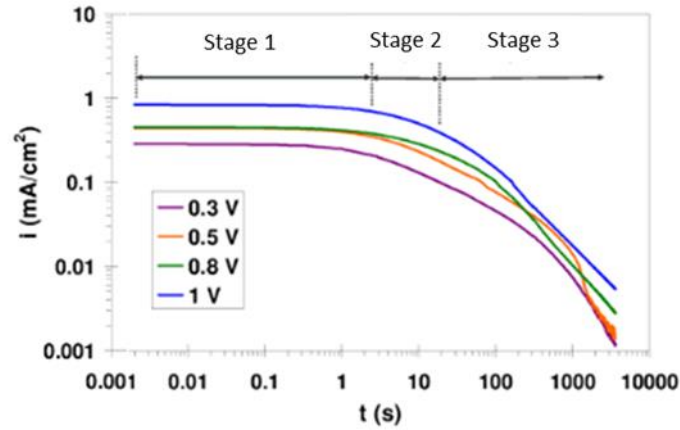
Figure 12. *Example of the passivation current evolution as a function of the passivation time* [151]*.*

In the first stage (*Figure 12*, stage 1), the current is constant with the time, showing a plateau which indicates that the oxide film formation and metal dissolution are equal. So actually, no oxide film is being formed because the metal surface is in equilibrium, continuously dissolving and reducing the metal. The second stage (*Figure 12*, stage 2) is a transition step in which the current starts to decrease very slowly. This, points out to a higher oxide layer formation rate in comparison to the metal film dissolution. After certain time, the oxide formation kinetic clearly dominates on the metal dissolution (stage 3 in the figure above) since the current density decreases very quickly with a clear linear dependence [151]. Generally, the study of the stage 2 is related to kinetics of the oxide formation in the very beginning of such process whilst the stage 3 is focused on the growth of the oxide layer as it occurs at higher times.

CHAPTER 2. MOTIVATION AND OBJECTIVES

Based on the fact that the well-known Cr(VI)-based electrodeposits have to be substituted due to environmental and health concerns (according to REACH compliance) and despite showing optimum corrosion protection capabilities, the industry is seeking for alternatives. Cr(III)-based electroplating baths have been found to fulfil most of the requirements even if they cannot completely replicate all the properties of the traditional Cr(VI)-based Cr coatings. However, such formulations are quite complex since they possess a more complicate electroplating mechanism, maintenance etc., and even today there are still some uncertainties around the properties of the obtained coatings. The industry has been pushed by the REACH to replace their Cr(VI)-based processes in a very short time and they turned very quickly to Cr(III)-based systems. In fact, most of them have introduced the Cr(III) empirically or even they added Fe salts to the process because it has been found to be beneficial for the electroplating process. Although this is one of the main reasons why there is still a high level of uncertainty about these coatings, it is becoming more complex due to the broad variety of Cr(III)-based electroplating baths which are showing very diverse formulations with different chemical components, additives and working conditions.

This Ph.D. research is focused on studying in detail the properties of Cr electrodeposits obtained from Cr(III)-based electroplating baths. Two different model Cr(III)-based electroplating baths were used to obtained the electrodeposits: generic chloride and sulphate-based baths, respectively. In parallel, Cr(VI)-based coatings have been obtained from a model Cr(VI)-based electroplating bath for comparison as well as a pure Cr standard. The idea is to generate enough knowledge to extrapolate to the more complex commercial electroplating baths (both, chloride and sulphate Cr(III)-based) in order to contribute to a next generation of decorative and functional Cr(VI)-free Cr(III)-based coatings, with a similar lifetime/durability and performance of the coatings obtained from Cr(VI)-based baths.

The uniqueness of this research is the following: (i) to isolate the electroplated decorative chromium layer from the substrate, (ii) to perform a detailed characterisation of the nanometric chromium and oxide layers, respectively, and (iii) to investigate the properties of the native oxide layer formed on such electroplated Cr layers. Therefore, sophisticated techniques able to provide information at nanoscale level have been used to fulfil the following main objectives:

1. To understand the effect that the different families of Cr(III)-based electroplating baths (chloride and sulphate-based) have on the physicochemical properties of the electroplated Cr layers and their native oxide layers, including the presence of additives such as Fe

2. To perform a detailed and tailored characterisation (composition, semiconducting and corrosion resistance properties) of the Cr layer and its native oxide in order to explain which feature is governing the performance of the electrodeposits, in terms of corrosion resistance for each type of coating.

The experimental approach followed for such study is illustrated below:
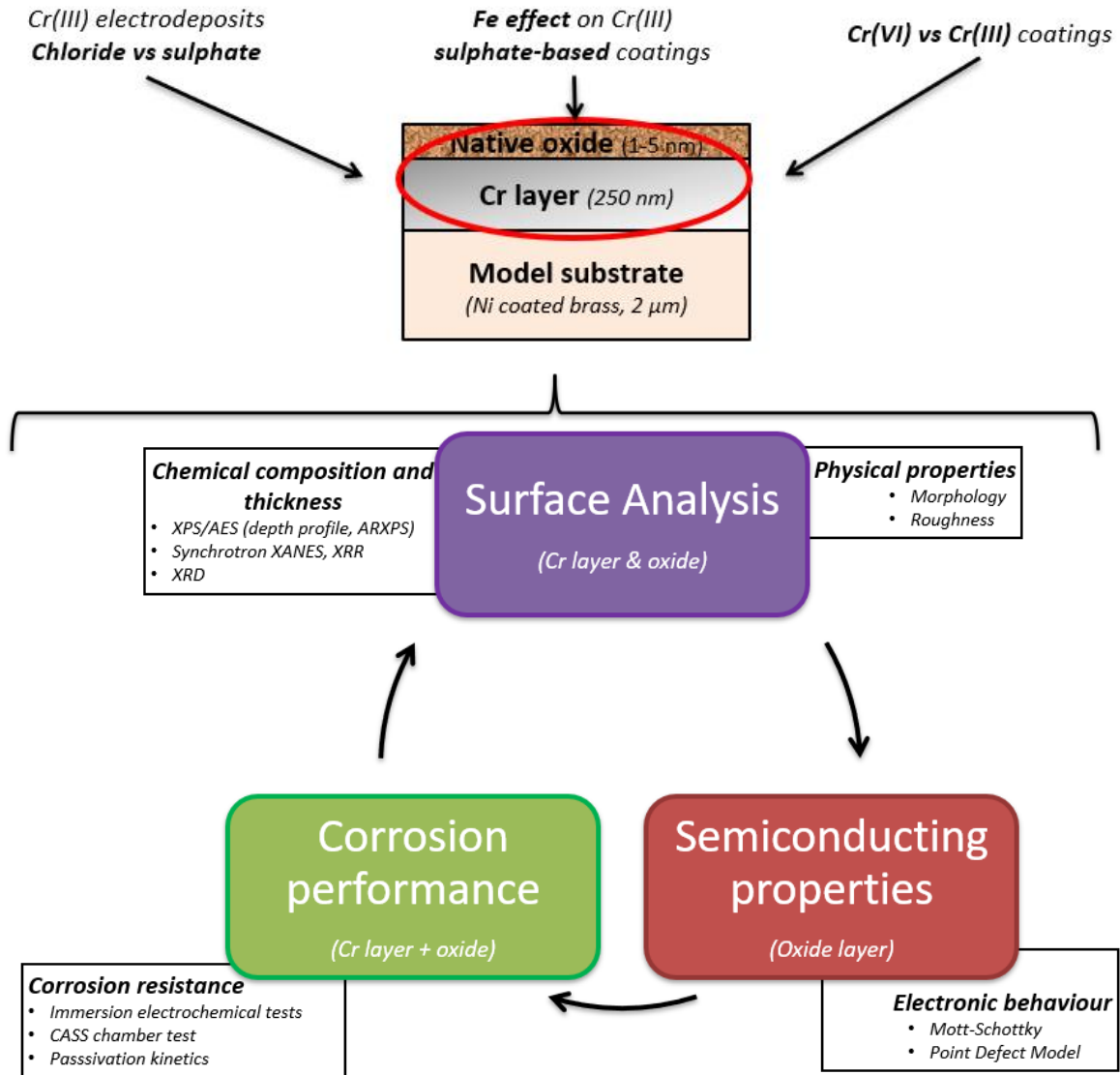
Finally, it should be stressed the high current interest and relevance of this topic as there have been several projects on the Horizon 2020 and Horizon Europe framework programme aimed to find suitable Cr(VI)-free alternatives for such decorative Cr coatings, as well as the industrial interest shown by ATOTECH Deutschland GmbH by triggering this Ph.D. research.

CHAPTER 3. EXPERIMENTAL TECHNIQUES AND METHODS

The detailed characterisation of the nanometric chromium layer and its oxide layer required the isolation of the topmost decorative chromium coating from the substrate (Ni coated brass); therefore, homogeneous, pore and defect-free metallic layers were obtained in order to assure that there was no effect of the underneath layers in any of the studied properties.

Two different model Cr(III)-based electroplating baths (chloride and sulphate-based) were used to obtain different Cr electrodeposits. Moreover, in order to improve the deposition rate of the electroplating process, sulphate-based baths were doped with different amount of Fe. Cr(VI)-based coatings were obtained from a model Cr(VI)-based electroplating bath for the sake of comparison as well a pure Cr standard.

All the measurements shown in this research are considered to be reproducible, in some cases the results are shown in tables constituted by mean values of several samples, including the standard deviation in parenthesis.

This chapter has been divided in three different blocks: (i) electroplating process of the coatings, (ii) surface analysis and (iii) electrochemical characterisation, which includes semiconducting properties and corrosion resistance evaluation.

3.1 Electrodeposition of the Cr coatings

Cr electrodeposits were obtained using model Cr(III) and Cr(VI)-based electroplating baths. Information about the setup, formulations and working parameters for obtaining such coatings are described below.

3.1.1 Sample preparation and activation

Brass plates coated with a single nickel layer were used as substrate to obtain the different decorative chromium coatings. Initially, the surface of each brass sample was prepared and activated as follows (*Figure 13)*: firstly, the brass substrate was immersed in an alkaline soak cleaner dissolution (Uniclean 154) to remove the heavy duty/dirt present on the surface, then a cathodic electrochemical cleaning was carried out using an alkaline dissolution (Uniclean 279) and finally the substrate was activated by immersion in an acidic dissolution (Uniclean 675) to promote the depassivation of the surface. Once the surface of the brass was cleaned and activated, a bright Ni layer (2 µm) was electroplated using a commercial electroplating bath (Unibrite 2002) in order to provide a smooth and continuous layer with the aim of increasing the adhesion of the posterior topmost Cr layer, as well as to develop a physical barrier between the brass substrate and the Cr layer (avoiding the Cu from the brass to contaminate the Cr(III) bath).
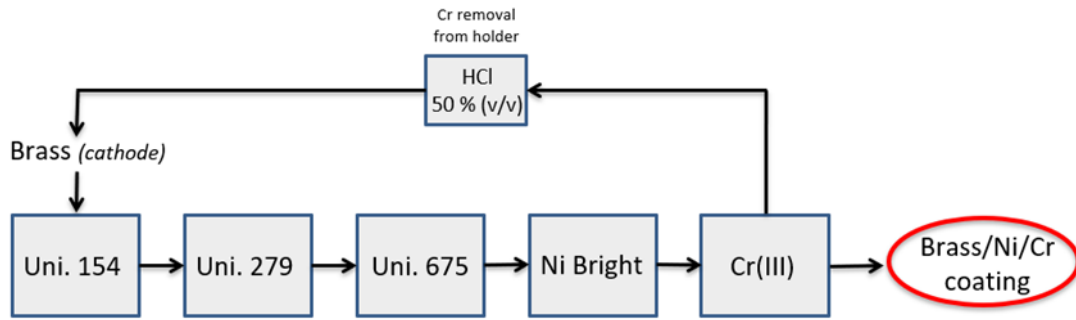
Figure 13. *Cleaning, activation and electroplating sequence of the brass substrate.*

Since the samples were electroplated using a metallic holder (*Figure 14 (a))*, the remaining Cr was stripped from the holder after each electroplating sequence by immersion in a 50 % HCl (v/v) dissolution for 3 min for the sake of its continuous reuse, avoiding its thickening (which could affect to the formal applied current density on the sample). The Ni was eventually stripped using the same methodology but with a HNO_3 dissolution.

The *Table 6* gathers chemical components/concentrations of the above-described activation dissolutions/baths, as well as their optimised working conditions.

Table 6*. Chemical composition and working conditions of the Uniclean and Unibrite 2002 dissolutions, used for the cleaning and activation of the substrate.*

Solution	*Chemical component*	*Concentration (gL^{-1})*	*Working conditions*
Uniclean	154	30	Immersion for 3 min at 60 °C
	279	70	10 Adm^{-2} (stainless steel electrode) for 30 s at R.T.
	675	60	Immersion for 3 min at room temp.
Unibrite 2002	H_3BO_3	40	Dummy plating 1.3 Ah/L Strong air agitation T: 55 °C, pH 3.5 - 4.0 Anode: Ni sheet (2:1 anode to cathode ratio) 6 Adm^{-2}, 10 min
	$NiSO_4·6H_2O$	270	
	$NiCl_2·6H_2O$	40	
	Nickel Carrier A-5	22	
	Nickel Additive SA-1	7	
	Unibrite 2002 brightener	0.35	
	Wetting Agent Ni835	1	

3.1.2 Cr electroplating setup

The cathode consisted of a 4x4x0.1 cm mirror finish brass sheet (63.30 % Cu, 36.66 % Zn, 0.012 % Ni, 0.013 % Fe, 0.004 % Pb, 0.002 % Sn and 0.001 % S) which was coated with 2 µm of a single bright nickel layer (Unibrite 2002) and plated by both sides (0.32 dm^2 of total area). A homemade Cu-based active shielding holder was used to homogenise the current distribution at the cathode and to avoid burning the sample due to possible current spikes at the edges (*Figure 14 (a)*). Air bubbling was used for the agitation of the baths in order to provide a suitable air flow for the electrodeposition process and it was achieved by building suitable homemade pipes, according to the dimensions of the plastic containers (*Figure 14 (b))*. These homemade parts are shown together with a general overview of the used electroplating setup in the *Figure 14 (c)* for both, the activation and electroplating process.
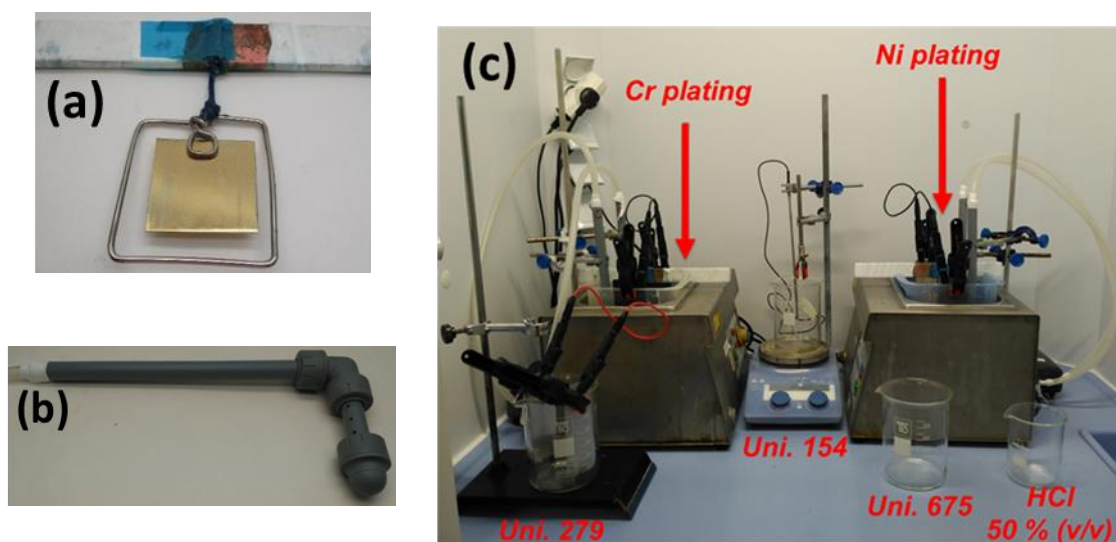
Figure 14. *Homemade (a)active shielding holder and (b) air agitation pipes used in the electroplating. (c) Overview of the cleaning, activating and electroplating setup.*

3.1.3 Electroplating baths and sequence

Several Cr systems were studied in this Ph.D. The chemical composition and working conditions of the different used Cr baths are shown in the *Table 7*. Two different Cr(III)-based electroplating baths were used (2.5 L), as well as one Cr(VI)-based bath (1.75 L) in order to have a traditional Cr(VI)-based Cr coating as reference system. All the chemicals used for the preparation of the electroplating bath formulations or for preparing any other dissolution required for other experiments were reagent grade or higher.

Table 7. Chemical composition of the model electroplating baths used in the deposition of the topmost Cr layer.

Model bath	Chemical component	Concentration (gL^{-1})	Working conditions
Chloride Cr(III)	$CrCl_3 \cdot 6H_2O$	107	*Dummy plating 1.3 Ah/L Slight air agitation* *T: 30 °C, pH 2.5 - 3.3 Anode: Graphite (2:1 ratio) 10 Adm^{-2}, 4 min*
	H_3BO_3	49	
	NH_4Cl	53	
	KCl	75	
	NH_4Br	10	
	HCOOK	67	
	CH_3COONa	14	
Sulphate Cr(III)	$Cr_4(SO_4)_5(OH)_2$ *(Basic chromium Sulphate)*	143	*Dummy plating 2.5 Ah/L Strong air agitation* *T: 60 °C, pH 3 Anode: Graphite (2:1 ratio) 10 Adm^{-2}, 15 min* *(Deposition time reduced to 13, 8 and 5 min, respectively as a function of the added Fe)*
	H_3BO_3	50	
	Na_2SO_4	110	
	K_2SO_4	90	
	$HOC(COONa)(CH_2COONa)_2 \cdot 2H_2O$ *(Trisodium citrate dihydrate)*	103	
	NH_2CSNH_2 *(Thiourea)*	0.01	
	$C_7H_4NNaO_3S$ *(Sodium saccharin)*	2	
	$FeSO_4 \cdot 7H_2O$	0, 0.02, 0.27, 1.1 *(0, 8, 100, 400 ppm Fe)*	
Cr(VI)	CrO_3	240 g/L	*Dummy plating 1 Ah/L No agitation* *T: 46 °C Anode Pb-Sn (1:1 ratio) 16 Adm^{-2}, 10 min*
	H_2SO_4	1 mL/L	

The pH of the Ni and Cr electroplating baths were adjusted using 10 % (v/v) H_2SO_4, NaOH and NH_3. Prior to obtain the coatings, every electroplating bath was stirred for 1 day after its preparation and further activated by dummy plating, carried out by applying the working conditions for 1-2 hours on a sample; this was done to remove beforehand the possible impurities of the used chemicals (the obtained dummy plated sample is discarded). All the optimised working conditions were stablished in order to obtain Cr coatings with an approximate thickness of 250 nm, whilst preserving a good aesthetic appearance.

Finally, coatings doped with Fe were obtained to reduce the deposition time. Different amounts of iron ($FeSO_4·7H_2O$) were added to the sulphate-based Cr(III) bath in order to study its impact on the coatings (see chapter 4.2) at three different levels: low, intermediate (close to the added Fe concentration in commercial baths) and high concentration in the bath. For simplicity, the obtained samples using the different Fe-doped baths will be referred as follows: Fe0 (non-iron containing reference), Fe8 (+8 mg/L Fe), Fe100 (+100 mg/L Fe) and Fe400 (+400 mg/L Fe).

3.1.4 Sample preparation of the Cr standard

Additionally, a 99.95 % purity Cr standard foil was acquired from Goodfellow as a pure bulk reference material. The Cr standard was cut and embedded in hot resin, afterwards it was grinded and polished to equalise its roughness to the one of the Cr electrodeposits (approximately 10 - 20 nm R_a, measured by profilometer and confirmed by AFM). An automatic Phoenix 4000 grinder and a polisher from Buheller was used. The standard was grinded and polished using the following procedure:

(i)   Grinding: 4000 µm silicon carbide paper
(ii)   Polishing: 3 µm silicon carbide paper
(iii)   Polishing: 1 µm silicon carbide paper

All the steps were applied for 5 min, working at 125 revolutions per minute and with a 20 N force. The grinding was carried out only the first time and eventually when the surface was heavily affected by the measurements carried out, in general, after each electrochemical measurement the polishing steps was found enough for the surface preparation.

3.2 Surface Analysis

Although the use of the techniques such as SIMS and ISS provide the highest sensitivity and depth resolution respectively, the use of AES and XPS/ARXPS was found to provide useful enough information.

3.2.1 Chemical composition analysis. XPS and AES

The chemical composition and oxidation state was studied by Auger Electron Spectroscopy (PHI-650, AES) and X-ray Photoelectron Spectroscopy (PHI 5000 Versaprobe II, XPS). AES measurements were carried out using 5 keV excitation energy whilst XPS measurements were performed using a monochromatic Al $K_α$ X-ray radiation (1486.6 eV

and 25 W); in both cases the used take-off angle was 45 °. Charge compensation was applied by an electron and ion flood gun (automatically tuned by the device) during the measurements conducted with the PHI 5000 Versaprobe II XPS, whilst the charge compensation was achieved by a manually controlled electron flood gun for the measurements carried out with the PHI 650 AES; the current of the flood gun was gradually increased in order to set the maximum of the C 1s peak to 284.8 eV.

Depth profile experiments were performed using a coupled monoatomic Ar ion gun with 3 and 1 kV in the case of AES and XPS measurements, respectively. The sputter rate corresponded approximately to 25 and 3 nm/min (corresponding to 3 and 1 kV Ar ion gun energy respectively) according to a calibration performed on a SiO_2/Si reference standard measured with such equipment. The fastest sputtering was used to study the Cr layers themselves (AES measurements). In contrast, special attention was paid on the native oxide film by carrying out XPS depth profile measurements using the softer and slower Ar ion sputtering rate.

AES results were analysed using the PHI Multipak software (v 9.8.0.19) and XPS curve fitting was performed using CasaXPS (v 2.3.19 PR1.0). PHI sensitivity factors were used for AES analysis together with a Shirley background subtraction for the peak fitting of XPS. Survey and high-resolution spectra of elements such as Cr, C, O and Fe were used for the data analysis. All the measured spectra were corrected to the metallic Cr $2p_{3/2}$ peak (574.2 eV) as the adventitious C peak from the C1s spectrum was only observable at the surface and not in the deepest measurements.

Different kind of measurements were carried out using AES and XPS with different conditions and aiming to obtain different information.

Typically, as a preliminary study of the surface, two AES survey scans were carried out on, before and after performing a cleaning etching with Ar ions, respectively, in order to obtain the composition of the surface with and without the presence of adventitious carbon. Secondly, a fast sputter rate AES depth profile was carried out to investigate the distribution of such chemical elements through the electroplated Cr layer (as a function of the depth). The depth profile was stopped after reaching the underneath Ni layer.

Regarding the XPS measurements, besides XPS depth profiles used a slower sputter rate, three different measurements were typically done: without any Ar ion sputtering (referred as "*as obtained*"), and after etching the surface approximately 10 nm (referred as *"etched surface*"). Because of the high intensity difference between the measurements of the Cr $2p_{3/2}$ and Fe $2p_{3/2}$ peaks before and after the sputtering, their high-resolution spectra are

presented in the min-max normalised way (maximum value is given 1 and 0 value to the minimum) to make easier their qualitative comparison by using the same modified scale.

The XPS measurements carried out on the Cr $2p_{3/2}$ aimed to the deconvolution of the Cr-O peak were acquired after performing a cleaning sputtering of the surface (6 s of Ar ion etching, corresponding to approximately 0.3 nm of superficial removal) instead of on the *as obtained* surface since a noisy signal was obtained due to the presence of an adventitious carbon an organic contamination layer. Such deconvolution is very dependent of the quality of the signal and, in fact, could affect dramatically to the fitting and the further quantification. Therefore, a soft sputtering was performed to get rid of the contamination layer, assuming that the native oxide layer will be minimally affected.

3.2.2 Synchrotron radiation based XAS measurements

Synchrotron measurements were performed at the BL29 beamline (BOREAS) of the ALBA Synchrotron light facility located in Cerdanyola del Vallès (Barcelona, Spain). X-ray absorption measurements were carried out at the X-ray Absorption Spectroscopy and magnetic circular dichroism endstation (HECTOR).

XAS measurements were carried out using a combination of Total Electron (TEY) and Total Fluorescence Yield (TFY) modes (larger analysed depth) on the Cr and Fe L-edge as well as on the C and O K-edge in order to investigate the compounds that were present in the electroplated Cr layers and on their oxide layers. Additionally, in some cases, the samples were bombarded with an Ar ion gun prior the measurements in order to get rid of the superficial contamination layer. Together with the Cr electrodeposits, powder standards (the CrO_3 and Cr_2O_3 chromium oxides, together with the $Cr_{23}C_6$ and Cr_3C_2 chromium carbides) were measured as well in order to identify the signals of the samples.

The samples were attached to the holder using double sided Cu tape and the powder standards were dispersed in ethanol, previously to being drop casted on the holder. Similarly to the XPS high-resolution spectra, the obtained data was normalised (min-max normalisation) to make the comparison of the samples and the standards easier.

3.2.3 Thickness of the oxide layer determination

Although XRR measurements were performed, results were not able to provide information about the thickness and density of the oxide layer and the obtained results only were able to provide information about the roughness. Additionally, estimation of the native oxide layer using ellipsometry was found to be very dependant of the used model, as well as, on the

parameters included during the fitting (e.g., roughness of the sample or thickness of the electroplated Cr layer). Therefore, the thickness was estimated by XPS measurements, using the Carlson and Strohmeier equation (*Equation 2*).

XPS measurements of the non-sputtered surface were used to calculate the area percentage of the metallic Cr and Cr oxide signals (I_m, I_{oxide} in the equation, obtained from the Cr-Cr and Cr-O components of the Cr $2p_{3/2}$ peak). The inelastic mean free paths of Cr and Cr oxide (λ_{Cr} and λ_{Cr2O3}) were calculated and extracted from the NIST Electron Inelastic-Mean-Free-Path-Database (SRD 71), corresponding to 1.55 and 1.83 nm respectively. The volume density of the Cr and Cr oxide were fixed in 7.19 and 5.22 g/cm^3, respectively and the take-off angle was 0.785 radians (corresponding to the 45 º take-off angle used during the XPS measurements).

3.2.4 Other complementary techniques

3.2.4.1 X-ray fluorescence (XRF)

An Energy Dispersive X-ray Fluorescence spectrometer (Fischerscope XDV-SDD) was used for a rapid verification of the chemical composition of the Cr layer in order to assess the reproducibility of the obtained Cr coatings, as they were obtained. The thickness of the electroplated Ni and Cr layer was also obtained using standards as a quality control of the electroplating process.

3.2.4.2 Profilometry

The roughness was obtained by contact profilometry using a profilometer Talysurf Intra 50 mm from Taylor Hobson. The measurements were carried out following the indications of the UNE-EM ISO 4288 [152].

3.2.4.3 Field Emission Scanning Electronic Microscope (FE-SEM)

The morphology of Cr coatings was investigated by using a JSM-7100F FE-SEM from JEOL. The chemical composition of the coatings was investigated by using the coupled EDX; chemical analysis and micrographs were acquired at 15 kV.

3.2.4.4 X-ray diffraction (XRD)

The crystallinity of the coatings was explored by using a D8 Advance equipment from Bruker to obtain their X-ray diffraction pattern. The measurements were carried out using a Cu Kα radiation source (λ= 1.54060 Å) in the 25 - 100 ° 2θ range and using a 0.02 ° step size and 10 s step time. Due to the nanometric thickness of the Cr electrodeposits, the XRD patterns

were obtained using grazing incidence configuration instead of the conventional Bragg-Brentano (θ/2θ) configuration, fixing the incidence angle to 4 ° and varying the detector angle in order to enhance the signal from the topmost Cr layer, avoiding any masking effects due to the substrate signal. Due to the deep penetration of XRD measurements (ranged in the microns rather than in the nanometre scale), thicker Cr layers (2 - 5 µm thickness instead of 250 nm) were electroplated exclusively for these measurements to avoid the high signal volume coming from the substrate, assuming that the crystallinity of the samples will be similar regardless the increased thickness of the metallic electroplated layer. However, due to the particular features of each model electroplating bath, setup and working conditions used, the sulphate-based Cr(III) electroplating bath, resulted to be less efficient and it was more difficult to obtain thicker Cr coatings in comparison to the chloride system. Thus, a small contribution of the substrate could be observed in the sulphate-based coatings whilst no Ni or brass signals are expected to be found in the chloride one due to their different Cr thickness (approximately 2 vs 5 µm respectively).

3.3 Electrochemical characterisation

Electrochemical measurements (i.e., potentiodynamic polarisation curves, linear polarisation resistance, Mott-Schottky and passivation kinetics) were performed on a standard three-electrode glass cell, using a Biologic VSP-300 multichannel and a PGSTAT 30 AUTOLAB potentiostat (only for passivation kinetics measurements). The Cr electrodeposits were used as working electrodes (1 cm^2 exposed area), a Pt mesh was used as counter electrode and a Saturated Calomel Electrode (SCE, KCl saturated) as reference electrode (E_{SCE}= + 0.244 V vs SHE); all the potential values shown in this work are referred to SCE. A borate buffer solution of pH 8.4 (0.3 M H_3BO_3 + 0.075 M $Na_2B_4O_7 \cdot 10$ H_2O) was used as electrolyte for the characterisation of the native oxide layer. The borate buffer electrolyte (BB), as well as NaCl electrolyte (concentrations from 10^{-3} to 1 M)) were used to evaluate the corrosion resistance of the coatings by the linear polarisation resistance (LPR and PDP) measurements. All the measurements were conducted at room temperature (25 ºC) and the OCP was monitored for 1h before the different electrochemical measurements listed below, except for the PDM, passivation kinetics measurements where no OCP was monitored, as well as the critical chloride content where 18 h of OCP were used instead. Additionally, accelerated corrosion test (CASS) was used for evaluating the corrosion resistance performance as it is carried out in the industry.

3.3.1 Semiconducting properties

Semiconducting properties of the native oxide layers were studied using the (i) Mott-Schottky approach, to study the concentration of point defects of the oxide films and the (ii) Point Defect Model for an additional analysis on the diffusion of such point defects through the oxide layer. These measurements were carried out using the pH 8.4 borate buffer solution.

3.3.1.1 Mott-Schottky

Mott-Schottky experiments were made through multi-frequency Electrochemical Impedance Spectroscopy (EIS) measurements by polarising the sample at different potentials within the passive region (previously determined by potentiodynamic polarisation curve), starting from the E_{OCP} until 0.6 V with 25 potential steps. Due to the larger passive region observed when adding Fe, the measurements were extended up to 1 V with 38 potential steps for the Fe400 sample. The potential steps were also increased to 60 when studying the Cr(VI)-based coating in order to have enough experimental data to perform the fitting of the linear region. Each EIS measurement was recorded in the 1 MHz - 100 mHz frequency range with 7 points per decade and 10 mV sinus amplitude disturbance. The coatings were exposed to the borate buffer electrolyte for 1 h prior to the Mott-Schottky measurement. The capacitance data was extracted from each EIS measurement at 1.233 kHz, since that frequency value was confirmed to be descriptive of the sample (not belonging to other external events/mechanisms, like pores or electrochemical reactions of the electrolyte) and was considered to be high enough (typically 1 to 10^2 kHz) to exclude the influence of leakage currents and interference of surface states phenomena, according to the assumptions of the Mott-Schottky [153,154]. The capacitance was calculated from the imaginary part of the impedance, assuming a pure capacitance behaviour, according to the following equation:

$$\mathbf{Z}'' = \frac{-1}{2\pi fc}$$

(Equation 17)

Where Z'' is the imaginary part of the impedance, f is the used frequency and c is the speed of light (3×10^8 m s^{-1}).

The charge carrier density was calculated from the *Equation 5* and *Equation 6* using a dielectric constant value of 12 for both chromium and iron oxide [72,73,116].

These measurements were carried out immediately after the obtaining of the sample.

3.3.1.2 Point Defect Model (PDM)

The PDM measurements were carried out according to the electrochemical procedure shown in *Table 8*. The step 1 was performed for the sake of the reproducibility of the surface, as a quality control by comparing the OCP value of each tested sample. The step 2 and 3 were focused on reducing and removing the native oxide layer sequentially in order to provide a reproducible surface for each experiment.

Table 8. Electrochemical procedure used for the Point Defect Model measurements.

Electrochemical protocol	*Measurement conditions*
1. OCP	5 min
2. Potentiodynamic polarisation curve	From E_{OCP} to - 1 V (100 mV/s)
3. CV (Cyclic voltammetry)	From - 1 V to - 0.8 V, 30 cycles (100 mV/s)
4. CA (Chronoamperometry) Passivation	- 0.1 V to 0.3 V range every 100 mV, for 9 h
5. Mott-Schottky	See Mott-Schottky section

The potential applied in the step 4 aimed to formed electrochemically an oxide layer, promoting the passivation (the potential was applied until stabilisation of the monitored steady state current, after 9 h). Finally, the charge carrier density was measured using the procedure described in the previous Mott-Schottky section. The steps 2 to 5 were carried out in a loop, removing the oxide layer and forming a new one to finally measure the semiconducting properties by Mott-Schottky, until passivating the surface at every potential, from the - 0.1 to 0.3 V range, every 100 mV.

3.3.2 Corrosion resistance

The corrosion performance of the different Cr systems was evaluated using conventional electrochemical techniques (OCP, LPR, PDP) as well as studying the critical chloride concentration for the breakdown of the oxide layer and the kinetics of the oxide formation. Although the borate buffer and 0.1 M NaCl electrolytes were mainly used, several concentrations of NaCl (0.001 M, 0.01 M, 0.1 and 1 M) were also used in order to find the critical chloride content that could promote the breakdown of the oxide layer.

3.3.2.1 Conventional techniques (OCP, LPR, PDP)

The corrosion performance was studied by using an electrochemical procedure (*Table 9*) constituted by a sequence of several non-destructive measurements (OCP and LPR). Such

measurements were carried out by immersing the Cr coatings in the electrolytes immediately after the obtaining of the samples (to avoid any uncontrolled aging effect on the surface).

Table 9. *Electrochemical procedure used for the corrosion resistance evaluation of the Cr coatings.*

Electrochemical protocol	Measurement conditions
1. OCP	1 h
2. LPR	$\pm$ 10 mV vs E_{OCP} (0.166 mV/s scan rate)
3. OCP	2 min
4. PDP	E_{OCP} to +0.6 V, 0.166 mV/s

The PDP were carried out by making anodic sweeps at the end of each experiment as a destructive test. PDP and LPR measurements were carried out according to the ASTM G5-94 [155]. The corrosion performance was evaluated in both, borate buffer pH 8.4 and 0.1 M NaCl electrolytes.

3.3.2.2 Critical Chloride content

The resistance of the passive film was evaluated by monitoring the evolution of the R_p (obtained from the LPR test) as a function of the chloride concentration in the electrolyte. Thus, the protectiveness of the oxide was evaluated by means of the critical chloride concentration, indicating the breakdown of the passive layer. These experiments were carried out using different NaCl dissolutions comprised in the 10^{-3} - 1 M range. In these measurements the R_p values were obtained from LPR experiments performed after 18 h OCP time, since some differences were emphasised between the studied Cr(III) coatings when the immersion time was increased.

During the analysis of the corrosion resistance properties of the it was found that the time elapsed from the obtaining of the sample to its analysis (their aging under uncontrolled conditions) had a strong effect, increasing the corrosion resistance of the coatings and showing different trends for the studied samples. This aging effect was only studied in the critical chloride content methodology.

3.3.2.3 Passivation kinetics or current-time transients

The protective features of the native oxide layers were also investigated by studying their passivation kinetics in the borate buffer (pH 8.4) electrolyte. Current-time transients were monitored whilst applying a passive potential. Due to the fast nature of such measurements, a very high data collection rate is required, and for that reason the passivation kinetics were carried out using a PGSTAT 30 Autolab potentiostat, following the procedure in *Table 10*.

Table 10. *Electrochemical procedure for the passivation kinetics measurements.*

Electrochemical protocol	Measurement conditions
1. CV	From - 0.5 V to - 1 V, 10 scans (10 mV/s)
2. CA	- 0.9 V, 5 min
3. CA	0.2 V, 5 s Acquisition rate f=1 kHz (1 point/ms)

Similar to the PDM measurements, step 1 aims to reduce and remove the native oxide layer in order to have a reproducible surface. The second step was performed to check the stabilisation of the surface, as well as the reproducibility between samples, by monitoring the current at such cathodic potentials. Finally, in the third step a passivation potential was applied for a very short time (5 s) in order to measure the current evolution during the passivation. The used passivation potential (0.2 V) lies approximately in the middle of the passive region of all studied samples.

3.3.2.4 Copper Accelerated Acetic Acid Salt Spray (CASS) test

CASS accelerated corrosion tests were run in a Saltevent SC500 Weiss cabinet according to ISO 9227:2017 [129], which suggests an exposure at 49 ºC to a fog of CASS electrolyte, being a pH 3.1 solution containing 50 g/L NaCl + 0.26 g/L $CuCl_2 \cdot H_2O$ [156]. The visual evaluation of the samples was periodically performed every 24 hours, and the examination criteria was based on the ISO 10289 [130]. The samples were considered to pass the test when no defects were observed on their surface, if so, they were considered as failed, putting them aside from the running test and indicating the time that took for that sample to fail.

CHAPTER 4. RESULTS AND DISCUSSION

4.1 Trivalent chromium coatings: chloride vs sulphate-based systems

Two different coatings were obtained using model trivalent chromium-based electroplating baths, chloride and sulphate-based electrodeposits, in order to study their corrosion resistance avoiding the influence of the substrate. A pure Cr standard was also tested as a reference system. The characterisation of the coatings was devoted not only to the Cr layer but also to its native oxide layer. On the one hand, the physicochemical properties of the surface were investigated using Field Emission-Scanning Electron Microscopy (FE-SEM), X-Ray Diffraction (XRD), X-ray Photoelectron Spectroscopy (XPS), Angle Resolved XPS (ARXPS) and Auger Electron Spectroscopy (AES). On the other hand, Mott-Schottky and Point Defect Model (PDM) measurements were carried out to obtain information about the semiconducting properties of the oxide layer, whilst the corrosion resistance was evaluated by accelerated corrosion test (CASS chamber test) and different electrochemical methodologies, such as Linear Polarisation Resistance (LPR) and Potentiodynamic Polarisation (PDP) tests using different electrolytes (borate buffer pH 8.4 and NaCl electrolytes). Although results revealed a similar morphology (crack-free Cr coatings), composition (Cr-C layer) and semiconducting behaviour (p-type), the main differences consisted in the lower C concentration, the presence of S in the composition and the certain crystallinity in the structure of the sulphate-based coating. Chloride-based coatings showed a slightly better corrosion resistance using non-aggressive electrolytes (borate buffer pH 8.4); however, when increasing the aggressiveness of the electrolyte (NaCl) both coatings exhibited a similar behaviour except for the 1-year-aged samples, where the sulphate-based Cr electrodeposits presented a better corrosion performance.

4.1.1 Electroplated Cr layer

4.1.1.1 Composition of the Cr layer by AES

The AES depth profile of the Cr standard, (*Figure 15* (a)) showed, as expected, a strong predominant Cr signal, together with an unexpected residual C signal. FE-SEM observations revealed that such C presence corresponded to superficial contamination of carbon particles (images not shown here), probably caused during the grinding process. Therefore, for the sake of comparison, the Cr standard is considered to be constituted by a mainly pure Cr chemical composition. In addition, certain oxygen concentration was found inside the bulk Cr, which remained constant after approximately 5 min of sputtering (later discussed in this section).
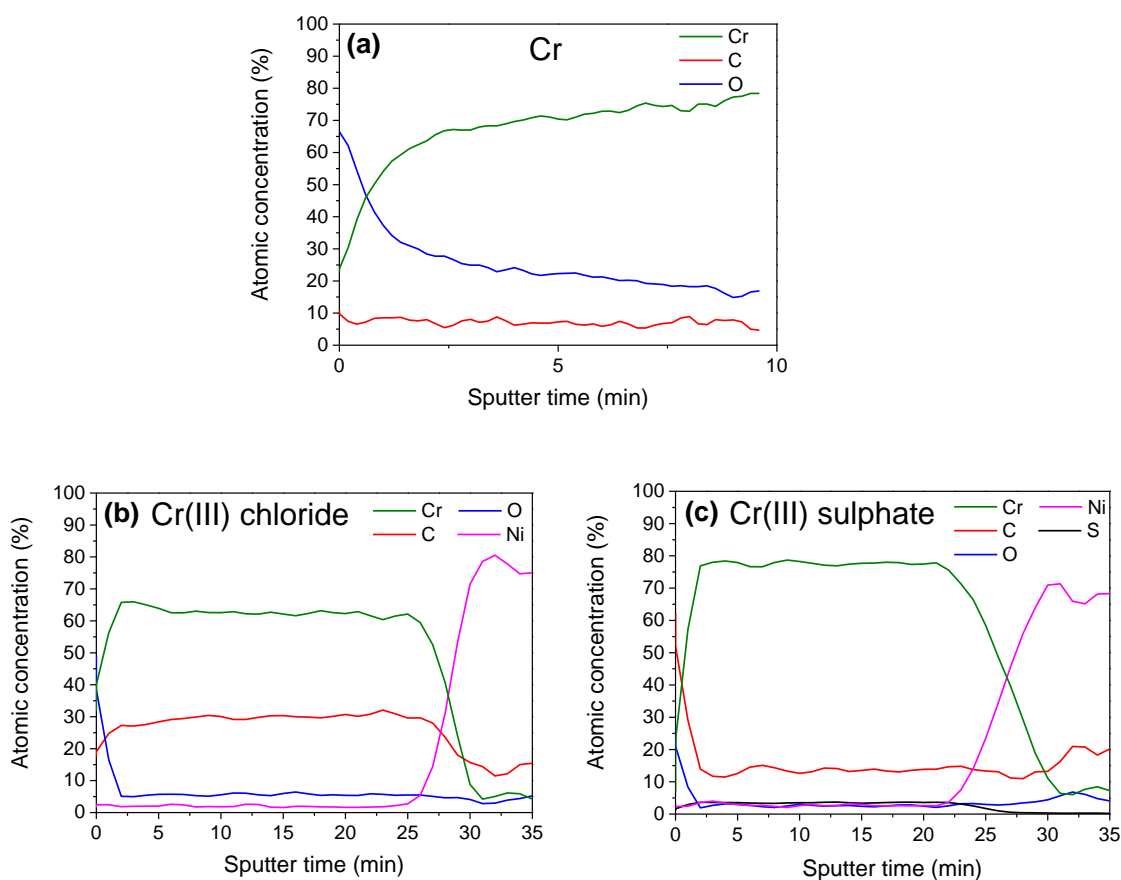
Figure 15*. AES depth profile of the (a) Cr standard and the Cr(III) systems: (b) chloride and (c) sulphate-based coatings.*

Regarding to both Cr coatings (*Figure 15* (b) and (c)), three different regions were identified in their AES depth profiles: (i) the surface (0 - 2 min of sputtering), corresponding to the chemical contribution of the oxide layer together with adsorbed species corresponding due to adventitious carbon or other exogenous organic species from the atmosphere, (ii) the Cr layer (2.5 - 25 min of sputtering) and (iii) the underneath Ni layer (beyond 25 min of sputtering). According to such AES depth profiles, both Cr(III)-based coatings revealed a homogeneous distribution of the different elements through the electroplated Cr layer, but a higher C concentration (approximately 30 vs. 15 % at.) was observed for the chloride-based coating.

4.1.1.2 Composition of the Cr layer by XPS

Initially, the quantification of the elements was done by AES, XPS and SEM-EDX. Different results were obtained (not shown here), which probably were attributed to (i) the high penetration of the beam in the SEM-EDX (deeper analysed volume than the others) and to (ii) the differences in the sensitivity factors that are used in AES and XPS analysis [157].

Furthermore, a strong overlapping of the Cr1 and O1 signals was observed in the AES measurements due to their proximity in energy which could compromise the quantification of these elements (Figure 47, Appendix A). As a consequence, the detailed quantification was made by XPS (XPS depth profiles displayed similar results in comparison to AES ones). The Table 11 shows the summary of the chemical composition for both Cr(III)-based coatings and the Cr standard, including values without and with a preliminary cleaning sputtering (etching up to 10 nm in the surface, which was found to be representative of the whole Cr layer).

Table 11. *Chemical composition, measured by XPS, of the surface and of the Cr layer (after etching approximately 10 nm).*

Sample	*atomic %*	*Cr*	*C*	*O*	*S*
Cr	*Surface*	5.6 (-)	72.2 (-)	22.2 (-)	-
	Etched	63.8 (-)	22.5 (-)	13.7 (-)	-
Cr(III) chloride	*Surface*	8.5 (5.2)	54.5 (21.4)	37.1 (16.1)	-
	Etched	70.1 (0.6)	20.2 (0.1)	9.7 (0.6)	-
Cr(III) sulphate	*Surface*	11.2 (2.6)	45.4 (6.5)	41.0 (4.2)	2.5 (0.4)
	Etched	78.2 (0.4)	11.1 (3.1)	7.9 (0.4)	3.0 (0.8)

The chemical composition of the surface (*as obtained* samples, without any Ar ion sputtering) of all samples is mainly constituted by a high C and O concentration, due to the presence of the oxide layer as well as the already mentioned superficial contamination layer (e.g., adventitious carbon and exogenous adsorbed organic contaminants) [158,159]. The high deviation of these values is attributed to the stochastic variation of such superficial contamination layer. After sputtering, although it was expected to remove the oxygen contribution on the etched surface, some residual O was still found in the Cr layer of both coatings, and even in the Cr standard, as previously shown by AES (*Figure 15*). This oxygen concentration was also found to be increased when the elapsed time between the sputtering step and the next measurement was extended (Figure 47, Appendix A). Considering this, the detected oxygen amount was attributed to the high reactivity and ability of Cr to form spontaneously an oxide layer (even inside the ultra-high vacuum chamber at very low oxygen concentrations) [160], since similar concentration plateaus were observed after etching all the studied samples (ranging the 8 - 14 % at. O).

Besides the oxygen, relatively high C concentrations were found in the Cr layer of both coatings. This is in agreement with previous studies that also investigated Cr(III)-based electrodeposits, where certain organic additives were deposited together with the Cr during

the electroplating process [37,46,47,161]. In fact, as pointed out in the AES depth profiles, the chloride-based Cr electrodeposits possess an approximately two times higher C concentration in the Cr layer. The unexpected high C concentration on the etched surface of the Cr standard was attributed, as mentioned before, to a C particle contamination which was later observed by FE-SEM. Additionally, traces of S were observed on the surface and inside the Cr layer of the sulphate-based Cr coating, probably related to some ad/absorbed sulphate-based salts from the electrolyte (*Table 7*).

XPS high-resolution spectra were measured in order to study the oxidation state and the surrounding chemistry of the chemical elements present in the coatings. The *Figure 16* shows representative XPS high-resolution spectra of the Cr $2p_{3/2}$, C 1s and O 1s, as well as the S 2p peak only for the Cr(III) sulphate-based coating (the same trend was observed for both Cr coatings, although S was not detected in the chloride system). The high-resolution spectra of the Cr standard are not discussed here (Appendix A).
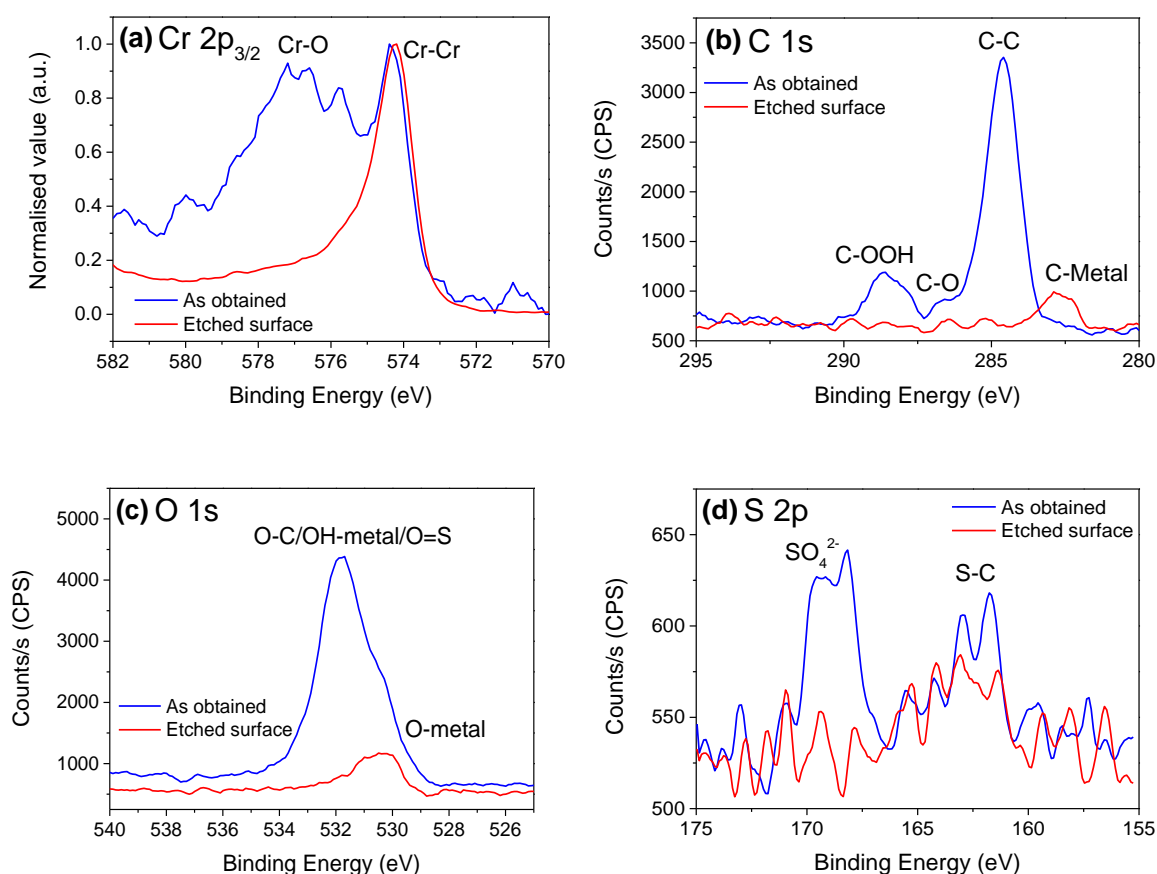

Figure 16. *Representative XPS high-resolution spectra of (a) Cr $2p_{3/2}$, (b) C 1s, (c) O 1s and (d) S 2p of the electroplated Cr(III)-based coatings, as a function of the sample's depth.*

The surface of the *as obtained* samples presents in the Cr $2p_{3/2}$ spectra a strong Cr-O component (576.8 eV), which corresponds to Cr oxide/hydroxide species of the native oxide layer, together with a weaker metallic Cr component (574.2 eV) [30,44,46,47]. The O 1s peak for the *as obtained* surface shows a broad signal constituted by O-C (531.8 eV) and O-metal (530.2 eV) components [46,47,56]. The former disappears due to the sputtering of the organic adsorbed contamination and the O-metal component decreases as a function of the etching, since to the native oxide layer is removed (the residual O-metal component was attributed, as mentioned before, to a repassivation issue inside the XPS vacuum chamber as explained before). The O-C signal of the *as obtained* surface is expected to be also including or masking an smaller OH-metal component located at approximately 533.5 eV [162–164], corresponding to Cr hydroxides at the outer part of the oxide layer and an additional O=S peak (532.5 eV), related to the SO_4^{2-} observed in the S 2p peak, which is discussed later [165].

Regarding the C 1s spectra, a broad C-OOH peak (288.6 eV) and a sharp C-C (284.6 eV) peak with a shoulder corresponding to C-O peak (285.6 eV) are observed in the *as obtained* surface. This is in agreement with the presence of a topmost carbon and organic contamination layer at the surface, as observed in the previous O 1s spectra. These elements disappeared after etching the surface and a new peak appears at 282.7 eV, corresponding to carbide carbon or C-metal [46,47,55]. This fact indicates that the obtained Cr electrodeposits are formed by chromium carbide instead of by a pure Cr layer [36,166]. According to the S 2p high-resolution spectra, adsorbed SO_4^{2-} salts (S-O peak at 168.9 eV) can be observed in the *as obtained* surface. After etching the sample, these adsorbed sulphates are removed and a new peak appears at 162.5 eV, corresponding to S=C [47,55]. This signal is believed to correspond to the thiourea organic additive (also called carbamide, CH_4N_2S) that is used in the sulphate-based electroplating bath (*Table 7*), which may get occluded inside the Cr layer during the electroplating process of the sulphate-based system.

4.1.1.3 Morphology

The surface morphology of the Cr(III)-based coatings was explored by means of FE-SEM. Micrographs (*Figure 17* (a) and (b)) revealed that both Cr electrodeposits present a microcrack-free and nodular surface morphology, which is typical of the Cr(III)-based electrodeposition mechanism [4,56,167,168]. Cross-section micrographs were also obtained (*Figure 17* (c)) to confirm the thickness values of the electroplated Ni and Cr layers as initially they were estimated by XRF.
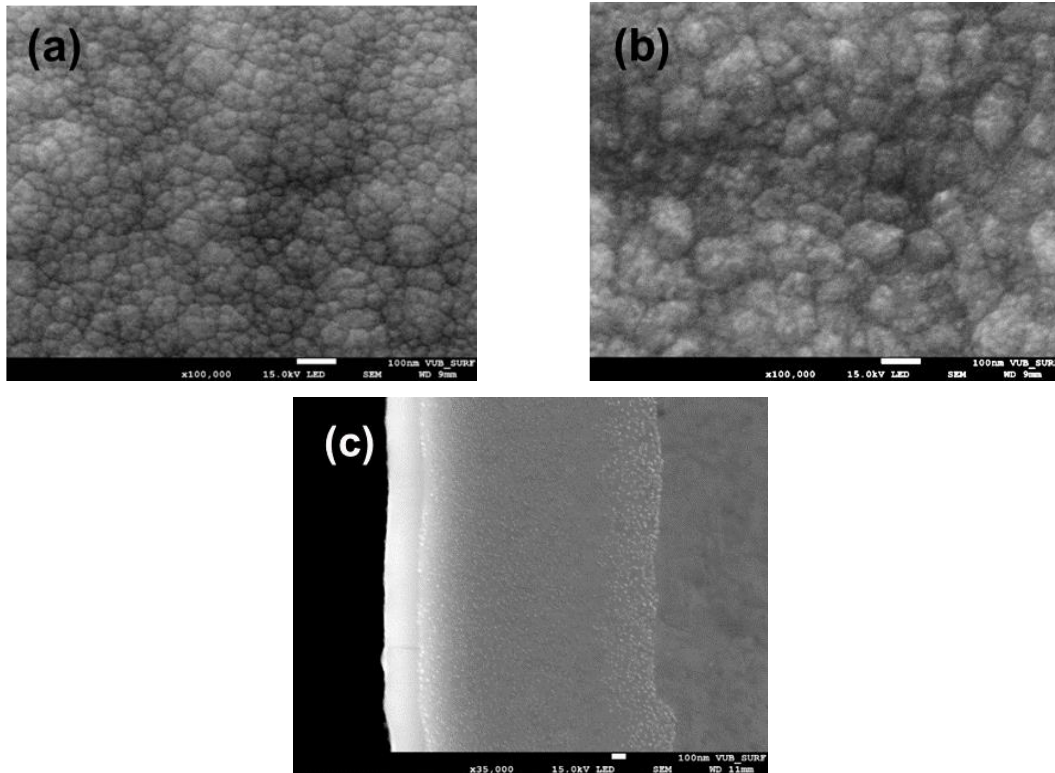
Figure 17. *Surface morphology of the Cr(III)-based electrodeposits: (a) chloride and (b) sulphate-based systems. Representative (c) cross-section of the chloride-based Cr coating.*

4.1.1.4 Crystalline structure

The crystalline structure was investigated by XRD. The *Figure 18* shows the different diffractograms used for the peak indexing.
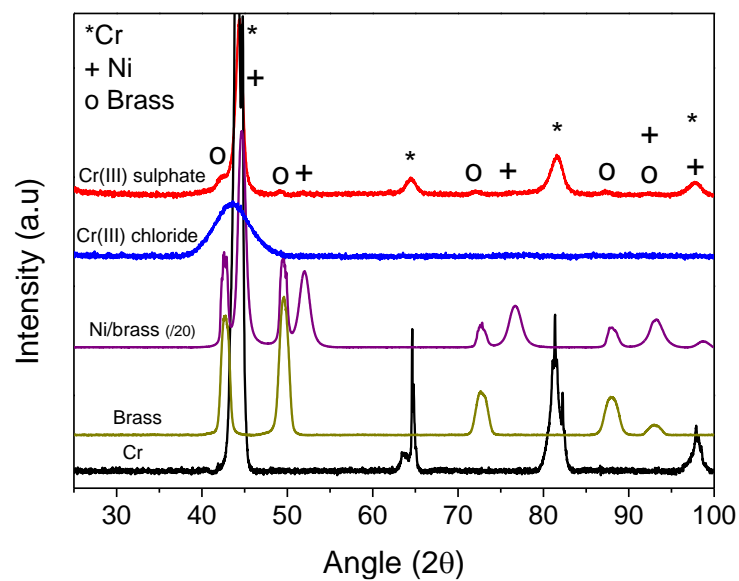
Figure 18. *XRD diffractograms of the Cr(III)-based Cr coatings, together with some standards of the underneath Ni layer and brass substrate, as well as the pure Cr.*

The Cr, Ni and Ni/brass (signal divided by 20 due to the high intensity obtained in its measurement, for the sake of the qualitative comparison) samples were measured as internal standards where the peaks 42.6; 49.6; 72.6; 87.9 and 93.0 º were believed to correspond to the brass substrate of the Ni/brass sample.

The sulphate-based Cr(III) electrodeposit shows sharper peaks, an intrinsic feature of a more crystalline structure. The more intense peaks located at approximately 44.4, 64.4, 81.5 and 97.7 º corresponds to the main peaks of the Cr standard, although certain contribution of the Ni underneath could be expected for the ones located at 44.4 and 97.7 º, respectively. Additional smaller peaks were found in the sulphate-based coating, which were attributed to signals coming from the underneath Ni layer and brass substrate: the peaks 42.6, 49.6, 72.6, 87.9 were found to correspond solely to the brass substrate whilst peaks 51.8 and 76.4 º were attributed to Ni. In contrast, the chloride-based Cr(III) coating possess a more amorphous structure due to the presence of a wide and broad peak. centred at 43.6 º, (main peak of the Cr and Ni). The absence of signals from the Ni and brass substrate in the chloride-based coating can be explained due to the higher thickness of Cr layer for this sample (5 vs 2 µm) due to the less efficiency of the sulphate-based electroplating bath as it was explained in the 3.2.4.4 section).

The more amorphous structure of the chloride system can be explained in terms of its higher C content, in comparison to the sulphate-based Cr(III) coating (*Figure 15*, *Table 11*). Generally, Cr-C coatings are amorphous, usually favoured by the higher C content. This is caused by the doping of C in the natural crystal lattice of the Cr that disturbs the crystalline setting order of the Cr atoms, making as a consequence, a more amorphous Cr layer [46,50].

In spite of the fact that both coatings have shown the presence of carbides by XPS (*Figure 16* (b)), no carbide phases were detected in any of the Cr(III)-based coatings. This could be caused because such carbides are in an amorphous form, being XRD unable to detect them.

4.1.2 Native oxide layer

4.1.2.1 Chemical composition of *as obtained* samples

XPS depth profiles were conducted with a lower sputter rate in order to elucidate the chemical elements (distribution and concentration) present in the oxide films of both Cr(III)-based coatings (*Figure 19*). The XPS depth profile of the Cr standard is shown and discussed in the Appendix A. Similar results were obtained in comparison to the previously carried out AES fast depth profiles (*Figure 15*).
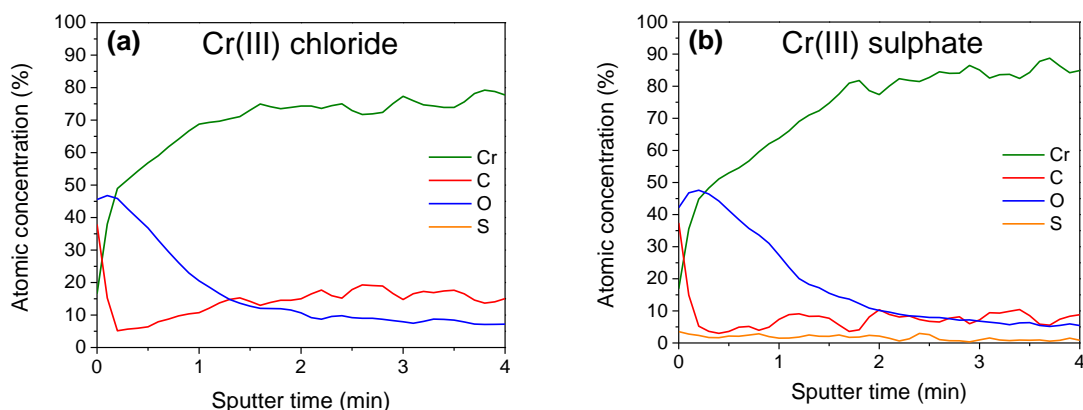
***Figure 19**. XPS depth profiles using a slower sputter rate to study the native oxide layers formed on (a) chloride and (b) sulphate-based systems.*

In addition to XPS depth profiles on the native oxide layer, the Cr $2p_{3/2}$ high-resolution spectra was analysed in detail. A specific deconvolution was carried out on the Cr $2p_{3/2}$ peak to quantify the contribution of the Cr oxide and hydroxide species from the Cr-O peak. Although the deconvolution of the Cr-O peak into a two components (oxide and hydroxide) is usually done by some authors [46,72,146], it is known that the Cr presents multiplet-splitting (due to the coupling between unpaired electrons from the core to with other unpaired electrons from the outer shell), making the deconvolution more complex. Such deconvolution was performed (*Figure 20*) according to the suggestions of some authors, who based their studies on theoretical and empirical data [169].
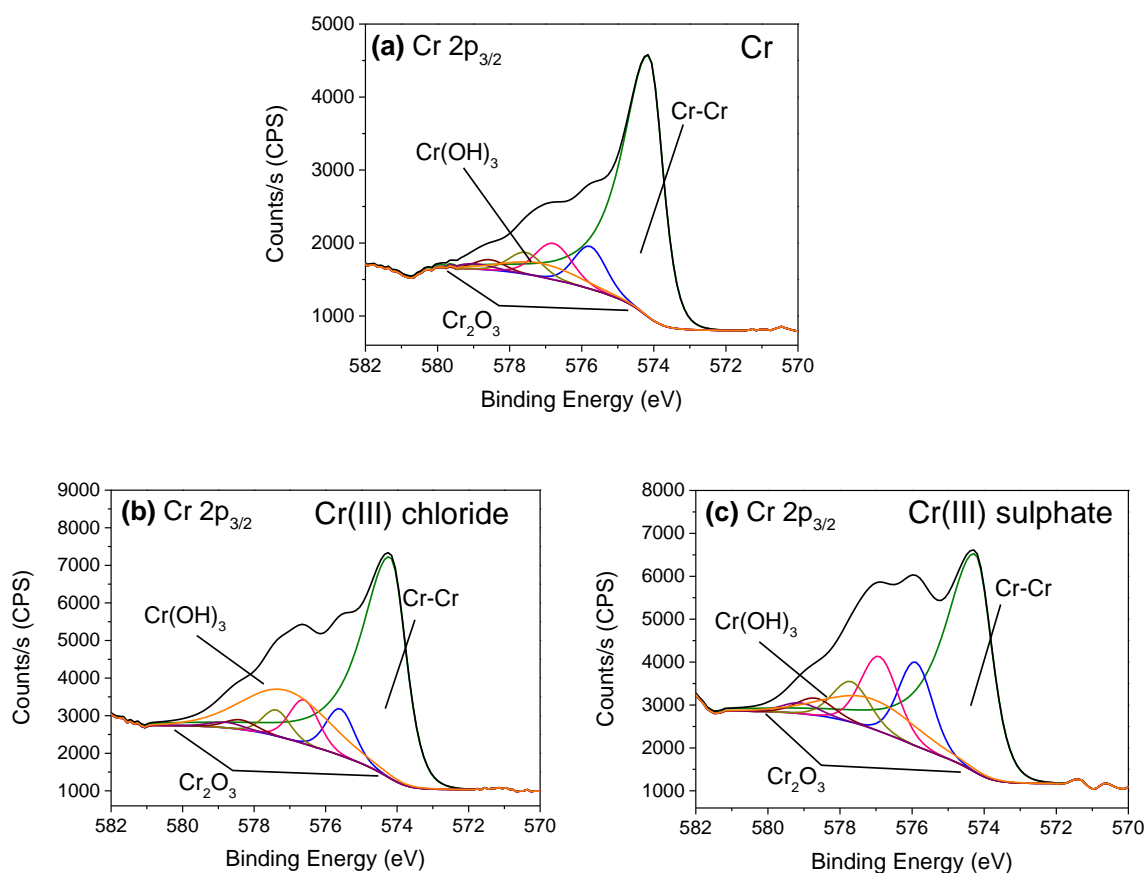
Figure 20. *Deconvolution, considering the multiplet-splitting effect, of the Cr 2p$_{3/2}$ peak of the (a) Cr standard (b) Cr(III) chloride and (c) Cr(III) sulphate-based coatings.*

The *Figure 20* shows the high-resolution spectra of Cr 2p$_{3/2}$ peaks of the native oxide layer from the different systems. The Cr oxide/hydroxide concentration (Cr-O component) was much higher (in terms of intensity and area) for the sulphate-based Cr coating whilst the lowest value is observed for the native oxide layer formed on the Cr standard. Moreover, the chloride system seems to possess the higher Cr hydroxide contribution among the three systems. These qualitative observations were confirmed in the *Table 12*, where the concentration of the Cr-oxide and hydroxide components of the native oxide layer are distinguished and quantified according to the deconvolution (taking into consideration the multiplet-splitting effect on the Cr 2p$_{3/2}$ spectra).

Table 12. *Analysis of the Cr 2p$_{3/2}$ peak deconvolution of the Cr standard and Cr(III)-based coatings.*

Atomic %	*Cr-Cr*	*Cr-O*		*Cr$_2$O$_3$*	*Cr(OH)$_3$*
Cr	62.3 (-)	37.7 (-)		32.2 (-)	5.5 (-)
Cr(III) chloride	51.8 (3.2)	48.2 (3.2)		13.8 (6.6)	34.3 (3.2)
Cr(III) sulphate	42.4 (1.3)	57.6 (1.3)		25.7 (6.6)	31.9 (5.3)

Native oxide layers formed on both Cr(III)-based coatings have approximately a 50 - 60 % of Cr oxy/hydroxide concentration (Cr-O component), showing an slightly higher general Cr-O concentration for the sulphate-based coating. Although both samples are showing a similar Cr-hydroxide content (34.3 and 31.9 %, respectively), the amount of oxide is slightly higher for the sulphate-based samples (25.7 vs. 13.8 %). Interestingly, despite showing the lower Cr-O concentration (37.7%), the Cr standard sample is mainly formed by Cr-oxide rather than Cr-hydroxides.

4.1.2.2 Thickness

The *Table 13* gathers the estimated values of the thickness of the native oxide layers using the Carlson equation (*Equation 2*).

Table 13. *Native oxide layer thickness estimated by XPS (Carlson equation).*

Sample	Native oxide layer thickness (nm)
Cr	0.9 (-)
Cr(III) chloride	1.0 (0.1)
Cr(III) sulphate	1.6 (0.3)

According to the table above, the thickness values of the native oxide layers are ranged around 1 - 2 nm, which is in agreement with previous studies [69,170,171]. Similar values were obtained for the oxide layer formed on the surface of the standard Cr and the chloride-based Cr(III) coating (0.9 and 1 nm, respectively), whilst the sulphate-based system showed a slightly thicker native oxide layer (1.6 nm). Such difference can be explained according to the previous XPS measurement (*Figure 20* and *Table 12*) where the Cr-O component was increasing in the following order: standard Cr < chloride-based coating < sulphate-based coating, showing a positive correlation between the Cr-O concentration and the thickness of the native oxide layer.

4.1.3 Semiconducting properties of the oxide layer

4.1.3.1 Mott-Schottky

Polarisation curves in borate buffer (pH 8.4) electrolyte were carried out prior to Mott-Schottky measurements in order to identify the passive region. The *Figure 21* shows the anodic branches in the borate buffer electrolyte (pH 8.4).
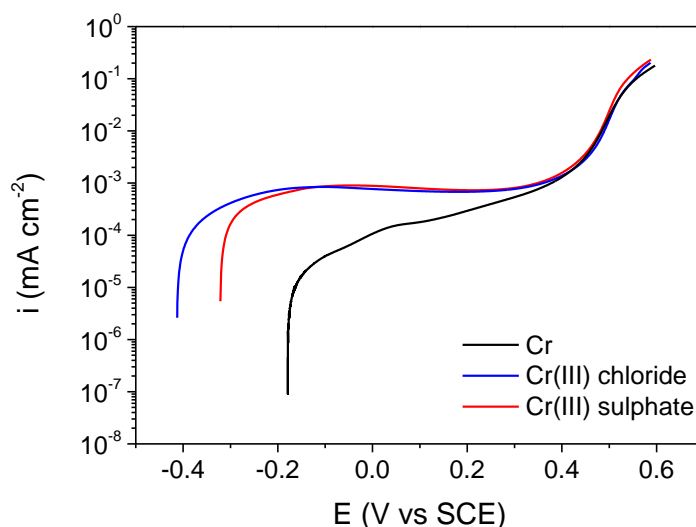
Figure 21. *Polarisation curve (anodic branch) of the Cr standard and Cr(III)-based coatings in borate buffer electrolyte (pH 8.4).*

The polarisation curves above showed a similar passive region for both Cr(III)-based coatings (approximately from - 0.4/- 0.3 to + 0.4 V) in which the current density is constant (approximately $8x10^{-4}$ mA cm^{-2}). Although the presence of a passive region is not clearly observable for the standard Cr, its significant lower current density value in comparison to the Cr(III)-based coatings (around 1 order of magnitude lower) confirms its passive behaviour. According to the anodic branches, both Cr coatings present a similar breakdown potential (corresponding to the start of the transpassive region) to the Cr standard located around 0.5 V in the borate buffer electrolyte. Regarding the E_{corr}, it can be observed the following increasing order to more noble values: - 0.412 V for the chloride-based coating < - 0.320 for sulphate-based coating and < - 0.180 V for the Cr standard. In general, the lower passivation current and the more positive E_{corr} of the Cr standard may initially indicate a more protective ability in comparison to the Cr coatings. If both Cr electrodeposits are compared, the only difference that can be observed is the E_{corr}, most probably due to the different chemical composition of their Cr and native oxide layers (*Table 11* and *Table 12*).

The *Figure 22* shows the Mott-Schottky plots where a similar and common trend can be observed for all systems: a negative slope, characteristic of p-type semiconductors, being the chromium vacancies (V_{Cr3+}) the main charge carriers or point defects in the native oxide layers. The presence of such defects in the Cr oxide layer are acting as acceptor dopants [60,72,172].
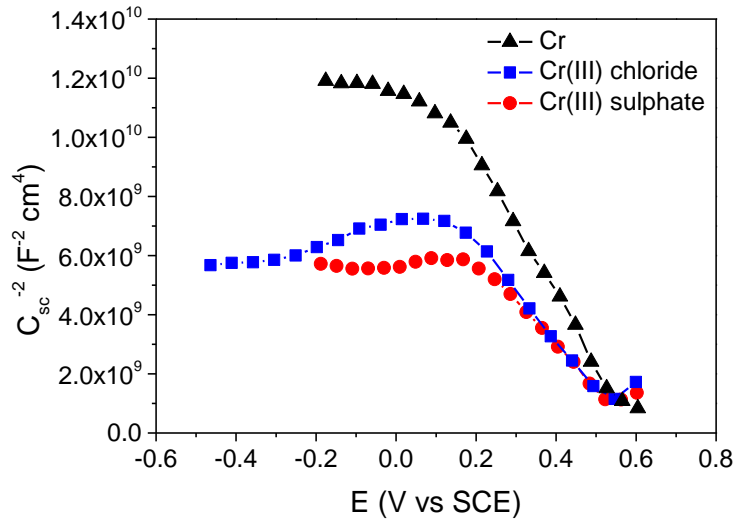
Figure 22. *Mott-Schottky plot of the Cr(III)-based coatings and the Cr standard in borate buffer (pH 8.4).*

The charge carrier density and the E_{fb} were calculated using the *Equation 5* (*Table 14)*. The fitting was carried out on the linear range of the Mott-Schottky plot, in the ranges: 0.17 - 0.53 V for the Cr standard, 0.22 - 0.49 V for the chloride-based coating, and 0.28 - 0.52 V for the sulphate system. The charge carrier density provides information about the concentration of point defects that are present in the oxide film (also related to its electronic and electrochemical activity). In theory, a lower donor and/or acceptor density limits the charge transfer. On the contrary, a high charge carrier density leads to a higher passive current density (it facilitates the oxide film dissolving and breakdown) [118,119].

Table 14*. Electronic properties calculated from the Mott-Schottky plot for the Cr standard and Cr(III)-based coatings.*

Sample	N_A *(x10^{20} cm^{-3})*	E_{fb} *(V vs SCE)*	*Semiconductor type*
Cr	4.8 (0.1)	0.60 (0.04)	
Cr(III) chloride	6.9 (0.2)	0.56 (0.01)	p
Cr(III) sulphate	8.0 (0.3)	0.57 (0.01)	

According to the table above, the calculated N_A are around 10^{20} cm^{-3} for all the systems, which corresponds to typical values of heavily doped oxide films in comparison with classical semiconductors like Si or Ga. Such values are in agreement with the ones obtained in other studies performed on Cr or Cr-Fe alloys, which are usually in the range 10^{19} to 10^{22} cm^{-3} [60,70,72,73,115]. The native oxide layer formed on the Cr standard stands out as the less defective system, due to its lower charge carrier density. This is consistent with the lower current values and the more positive E_{corr} observed [173,174] in the polarisation curve

(*Figure 21*). In contrast, both Cr coatings present higher N_A values, where the chloride system seems to have a slightly lower concentration of point defects in comparison to sulphate (6.9 and 8.0×10^5 cm^{-3} respectively). The more defective native oxide layer observed for the sulphate-based Cr coating could be related with the presence of adsorbed S on its surface, as previously observed by AES and XPS measurements (*Figure 15* and *Table 11*). The presence of S could hinder the oxide layer formation, leading to a more porous or defective oxide film, as shown by its lower N_A value; a similar detrimental effect was found in the chromium oxide layer of the stainless steel [113].

Regarding the E_{fb}, potential both Cr(III)-based Cr coatings are showing similar values (0.56 and 0.57 V, respectively) and close to the standard Cr (0.60 V), which probably points out to the presence of a native oxide layer of similar chemical nature for all the systems [69], i.e., a native oxide layer constituted by a pure Cr-oxide/hydroxide single layer (*Figure 20*).

4.1.3.2 Point Defect Model

Point Defect Model (PDM) measurements were performed in order to provide complementary information about the charge carrier density/point defects present in the oxide layers and how they can migrate through the native oxide layer. It should be noted that these kinds of measurements are based on the study of electrochemically formed new oxide layers at different passivation potentials (the native oxide layer is removed).

The *Figure 23* shows the evolution of the donor density (N_A) as a function of the film formation potential which trend is consistent with results studying similar systems [69,124].
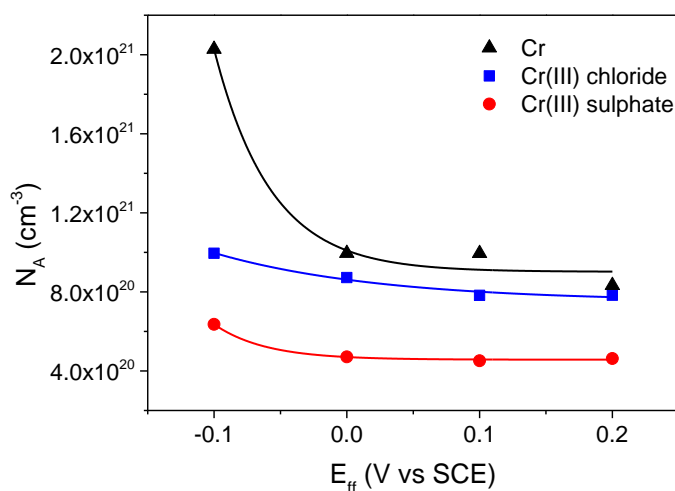
Figure 23. Charge carrier density evolution of the Cr(III)-based coatings and Cr standard as a function of the film formation potential.

The data was fitted according to the *Equation 7* (experimental fitting shown in the graph), the *Table 15* shows the results. Parameters such w_1, w_2 *and b* were obtained from the experimental fitting and were used to calculate the diffusion coefficient (D_0), according to *Equation 8, 9 and 10.* The discussion of the results was carried out in terms of the D_0 and the steady state current (i_{ss}) values.

Table 15. *Results on the ion migration properties obtained from the fitting of the Point Defect Model data.*

	Cr	Cr(III) chloride	Cr(III) sulphate
w_1 *(cm^{-3})*	1.1×10^{20}	1.1×10^{20}	1.3×10^{19}
b (V^{-1})	23.44	8.0	25.8
w_2 *(cm^{-3})*	9.0×10^{20}	7.5×10^{20}	4.6×10^{20}
$K_e = \varepsilon_L$ *(V cm^{-1})*		1×10^{6}	
i_{ss} *(A cm^{-2})*	1.7×10^{-8}	3.1×10^{-8}	1.0×10^{-8}
D_0 *(cm^{2} s^{-1})*	7.2×10^{-19}	1.6×10^{-18}	8.8×10^{-19}

Similar steady state current values (around 10^{-8} A cm^{-2}) were obtained for all the systems decreasing in the following order: 3.1×10^{-8} A cm^{-2} chloride-based coating > 1.7×10^{-8} A cm^{-2} Cr standard > 1.0×10^{-8} A cm^{-2} sulphate-based coating. Regarding the D_0, a higher value was also obtained for the chloride-based Cr coating (1.6×10^{-18} cm^{2} s^{-1}) in comparison to the sulphate system (8.8×10^{-19} cm^{2} s^{-1}) and the Cr standard (7.2×10^{-19} cm^{2} s^{-1}). In theory, a low passivation current and diffusivity coefficient denotes a more protective oxide layer [175]. According to these results, the chloride system might provide a lower protection, (higher i_{ss} and D_0) than the Cr standard and the Cr(III) sulphate-based systems (lower i_{ss} and D_0 values). However, it seems to be a controversy between Mott-Schottky and PDM results: the oxide layer formed on the sulphate-based Cr coating was the system with the highest acceptor density or point defects in Mott-Schottky (*Table 14*) whilst it is the system with the lower acceptor density (PDM, *Figure 23*). This discrepancy could be caused because in Mott-Schottky the native oxide layer was explored whilst in PDM a fresh electrochemically formed oxide layer after removing the native oxide was studied (further discussed in the Annex B); furthermore, some authors observed significant differences in the chemical composition of the native and passive films on the same surface [176–178]. Therefore, Mott-Schottky reveals the presence of a more defective native oxide layer in comparison to the one formed electrochemically in PDM for the sulphate-based system. Such controversy can be justified by the presence of traces of S in the native oxide layer (according to AES and XPS measurements) which, as mentioned before, could be causing the formation of a more defective native oxide layer; the removal of such native oxide layer could also have removed

totally o partially the adsorbed S, leading to a new less defective fresh oxide film. This hypothesis was confirmed by removing the native oxide layer electrochemically and performing a Mott-Schottky measurement on the new formed oxide film, whose point defects were decreased for the sulphate-based system whilst an increase was observed for the chloride system (see Appendix B).

Finally, the Cr standard shows the lower acceptor density in PDM and the lower diffusion coefficient which is in agreement with the findings observed in the Mott-Schottky. In this case, the Cr standard is polished after each experiment and it seems that, independently of the way that such oxide layer is formed, the semiconducting properties studied in Mott-Schottky and PDM are in agreement.

4.1.4 Corrosion resistance evaluation of the Cr layer and oxide film

4.1.4.1 Kinetics of the oxide layer formation

The *Figure 24* shows the evolution of the current as a function of the time, also called current-time transients, which are used to carry out kinetic studies on the oxide formation. The *Table 16* shows the results after a linear fitting in the range of 20 - 60 ms (which corresponds to the oxide formation stage).
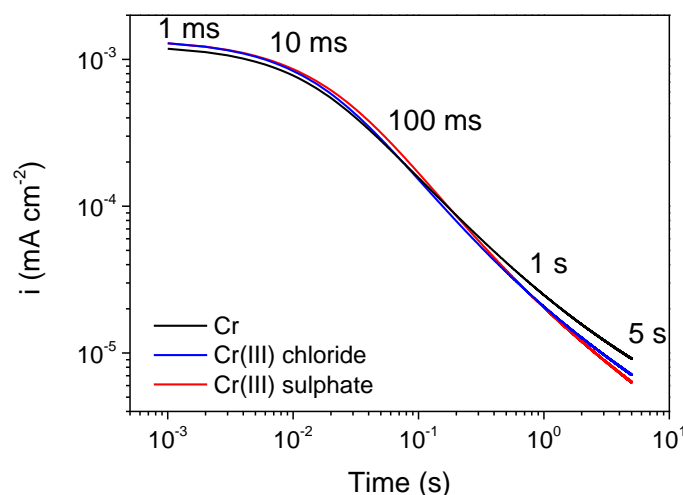
Figure 24. *Passivation kinetics or current-time transients measurements of the Cr standard and the Cr(III)-based Cr coatings.*

Table 16. *Obtained parameters from the linear fitting of the passivation kinetics measurements.*

Sample	n	i_0 (mA cm^{-2})
Cr	0.74 (0.04)	1.3 (0.2)
Cr(III) chloride	0.78 (0.01)	1.4 (0.1)
Cr(III) sulphate	0.74 (0.06)	1.4 (0.2)

As mentioned in the Introduction, these two parameters were used for discussion: the slope (passivation index, referred as *n)* which is proportional to the kinetics of the oxide formation and the resulting passivation current of the initiation of the passivation (referred as i_0 from now on). Similar time-current transients were observed in the *Figure 24*, as well as similar i_0 and *n* values (*Table 16*). This indicates that all the systems have similar oxide formation kinetics. Usually, *n* values close to 1 indicates a fast oxide formation kinetic and characteristic of an compact and protective oxide layer [148–150].

According to the protocol described in the Experimental chapter, analogously to PDM, the passivation kinetics measurements also require to remove the native oxide layer prior to the passivation, therefore, similar trends to the ones observed in PDM will be expected. However, it must be taken into consideration that the measurements of the passivation kinetic is very fast (few seconds or even less than 1 second according to the fitting performed in this study). So, in current-time transients, only the inherent properties to the very beginning of the oxide layer formation are studied whilst in PDM the passivation potential is applied for much longer times (9 h), leaving the oxide layer to be completely formed. That is the reason why the differences mentioned in the PDM measurements were not observed in the passivation kinetics, even if both methodologies are based on a similar protocol.

4.1.4.2 Corrosion resistance evaluation

4.1.4.2.1 Corrosion resistance evaluation in borate buffer electrolyte

LPR measurements were performed in borate buffer electrolyte (pH 8.4) and the polarisation resistance (R_p) was determined (*Table 17*) after linear fitting.

Table 17. *Polarisation resistance values obtained from the LPR measurements.*

| Samples	R_p (x10^5 Ω cm^2)
Cr	6.6 (1.0)
Cr(III) chloride	2.6 (0.6)
Cr(III) sulphate	1.0 (0.1)

The Cr standard possesses the highest polarisation resistance in the borate buffer electrolyte (6.6×10^5 Ω cm^2), which is in agreement with the low current values observed in the anodic branch of the polarisation curve (*Figure 21*), the lower defects found in Mott-Schottky (*Table 14*) and the lower diffusion coefficient observed in PDM (*Table 15*). Both Cr(III)-based coatings exhibit a lower R_p in comparison to the Cr standard (2.6 and 1.0×10^5 Ω cm^2 for the chloride and sulphate system respectively). Even if the differences between both Cr electrodeposits is small, it seems that the chloride-based system possess a slightly higher R_p indicating a possible better corrosion performance than the sulphate-system. The lower corrosion resistance of the sulphate system can be caused by the presence of adsorbed S [113], found by surface analysis (*Figure 15* and *Table 11*) which, as mentioned before, could have affected to the oxide film formation, leading to a more defective native oxide layer (N_A, *Table 14*). This, together with the fact that the Cr layer, electroplated by using the sulphate-based Cr(III) electroplating bath, resulted in a more crystalline structure (more presence of grain boundaries, which can act as potential corrosion sites or local points to initiate pitting corrosion) could explain the slightly lower corrosion performance of the sulphate system when comparing to the chloride one [51,179].

4.1.4.2.2 Corrosion resistance evaluation in NaCl-based electrolytes

Additional experiments were carried out to explore the corrosion behaviour under different close to service conditions scenarios. Three complementary experiments were performed varying the aggressiveness of the environment: (i) Copper Accelerated Acetic Acid Salt Spray (CASS) as the most aggressive test commonly used for evaluating such decorative coatings in the automotive industry, (ii) Potentiodynamic Polarisation (PDP) in 0.1 M NaCl electrolyte and (iii) critical chloride content test, varying the concentration of NaCl in order to provoke the breakdown of the passive layer where the R_p was obtained by LPR.

- ***Copper Accelerated Acetic Acid Salt Spray (CASS) test***

The Cr(III)-based coatings were also tested in the CASS chamber (typical test in the industry) in order to study their corrosion resistance under accelerated conditions. The evaluation was carried out by visual examination according to a standard methodology mentioned in the Experimental section; such evaluation was done every 24 h. rinsing and drying the samples previously. The *Figure 25* shows the pictures of the evolution of the samples in the CASS chamber after 48, 72 and 96 h.
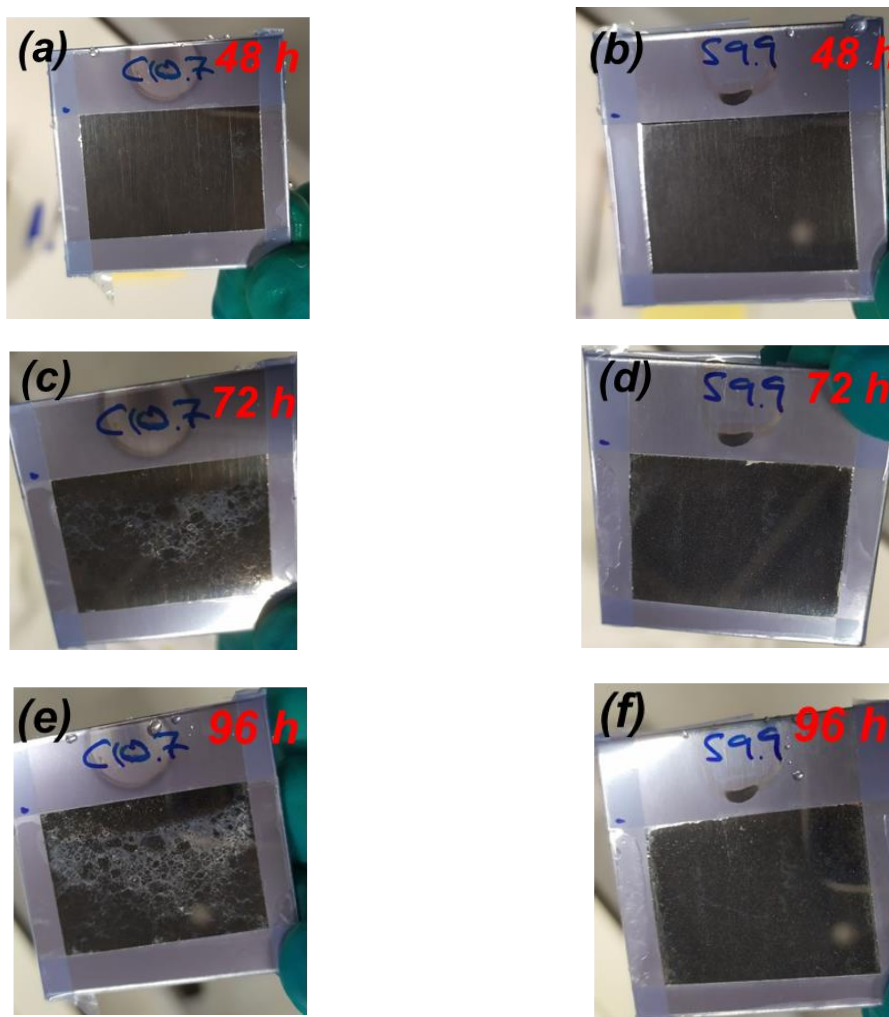
Figure 25. *Visual examination of the Cr(III)-based coatings (chloride, left column and sulphate right column) after (a, b) 48, (c, d) 72 and (d, e) 96 h of exposition to the CASS chamber.*

A similar appearance is observed for all samples, without exhibiting any corrosion pits or visual damage of the surface (pictures not shown) after 24h. However, white rust was observed in both Cr(III)-based Cr coatings, together with smaller red pits only observed in the sulphate one after 48 h. The red and white corrosion products are believed to be caused by the oxidation of the substrate, Cu and Zn respectively: (i) the observed reddish corrosion products are also known as "red rot" which are constituted by Cu residues that came off as a result of the zinc leakage during the dezincification of the brass, and (ii) the white rust was caused by the oxidation of the Zn which formed white Zn hydroxides residues. After 72 and 96 h such defects further increased, pointing out both Cr coatings failed between 24 and 48 h. However, the corrosion had a less visual impact for the sulphate-based system, showing more homogeneously spread pits.

Usually, if commercial samples having a multilayer nickel-chrome configuration are tested, these kinds of defects are not observed. This different behaviour between commercial and coatings studied in this research may be due to:

(i) The presence of different Ni thickness and number of Ni layers underneath. Ni layers in commercial systems are usually 5 times thicker (10 µm in the commercial samples vs 2 µm for the model systems obtained in this work); isolating more efficiently the topmost decorative Cr layer from the substrate. Moreover, three different nickel layers are commonly used instead of a single one (*Figure 1*).

(ii) The absence of micropores/microcracks, which could unable the proper distribution of the corrosion current along the surface of the sample (through such micropores/microcracks) and therefore, the corrosion attack could be located and focused in singular spots/points, reaching more easily even to the substrate.

Therefore, the CASS chamber test seems not to be suitable to evaluate the chromium coating itself. Due to the intrinsic features of the samples (substrate, intermediate nickel layer and the distribution and thickness of the electroplated Cr layers), all coatings suffered a severe and fast corrosion process that did not allow to distinguish between them. Thus, a less aggressive environment is required to compare both Cr(III) samples.

-   ***Potentiodynamic polarisation tests. "As obtained" samples in 0.1 M NaCl***
The aggressiveness of the electrolyte was decreased using 0.1 M NaCl instead of the CASS test electrolyte (used in the previous section). The *Figure 26* shows the anodic branches if the "*as obtained*" samples in 0.1 M NaCl, together with the ones measured in borate buffer electrolyte (*Figure 21*), for the sake of comparison.
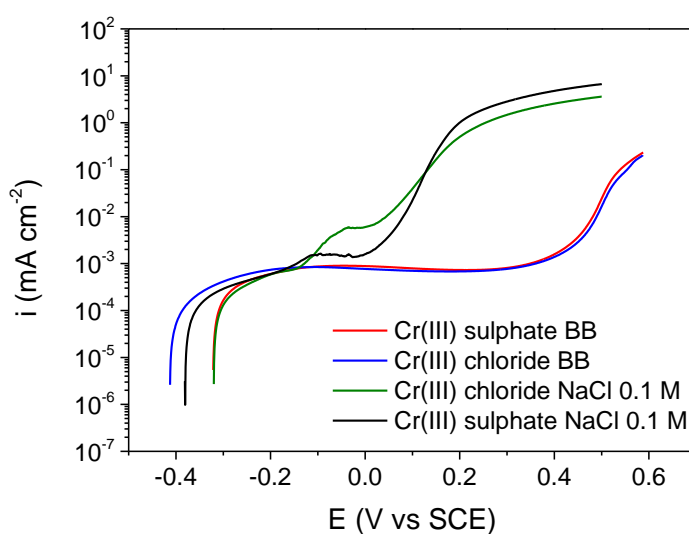
Figure 26. *Potentiodynamic polarisation curve of* the *as obtained Cr(III)-based Cr coatings in both borate buffer and 0.1 M NaCl electrolyte.*

Similar PDP curves were obtained for both Cr(III)-based systems in 0.1 M NaCl. The anodic branches showed an increase of the anodic current at approximately - 0.15 V, which was also observed in previous studies of Cr alloys [180] and could be attributed to the oxidation phenomenon of Cr(III) ions into Cr(VI) [181]. After that, a pseudo-passive region is observed in the potential range from - 0.1 to 0 V for both coatings. The i_{pass} for the chloride-based coating is approximately a ½ order of magnitude higher if compared to the sulphate-based system (6.0 and $1.4x10^{-3}$ mA cm^{-2} approximately), showing, initially, a slightly less stable oxide film. After such plateau, the anodic current was dramatically increased (approx. at 0.12 V), due to the metal dissolution taking place at the transpassive region, close to 0 V.

If the PDP curves obtained in both electrolytes are compared, a shift to more positive E_{corr} value is observed in 0.1 M NaCl as well as a narrow passive region, having a lower E_{pit} in comparison to the breakdown potential observed in the measurements with borate buffer (0.04 instead of 0.45 V), as a result of the more aggressiveness of the NaCl electrolyte.

Despite the differences observed in the PDP measurements carried out in 0.1 M NaCl, both coatings showed similar R_p values (not shown here), indicating that maybe this electrolyte was still very aggressive to show the subtle differences between the Cr(III)-based systems.

- *Critical chloride content*

CASS tests and PDP did not show significant differences in terms of corrosion resistance performance between *as obtained* samples for both systems. Therefore, in order to have a broad variety of aggressiveness, a screening of the corrosion resistance (based on the R_p obtained from LPR measurements) was carried out varying the chloride content (*Figure 27*) for two types of samples: (a) *as obtained, and (b)* aged samples (around 1 year).
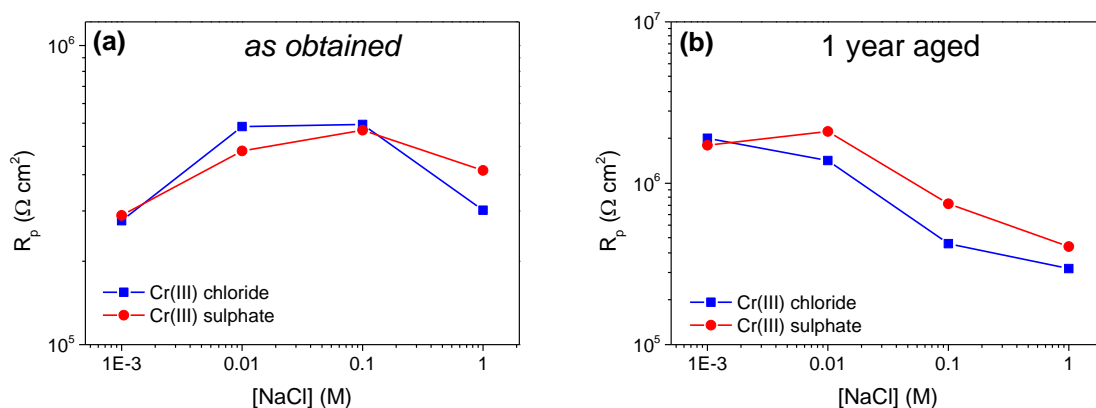
Figure 27. *Polarisation resistance evolution of the Cr(III)-based coatings as a function of the different chloride concentration in the electrolyte: (a) samples tested immediately after their obtaining and (b) after 1 year elapsed time.*

The figure above shows the variation of the R_p as a function of the chloride concentration. On the one hand, as obtained samples (*Figure 27* (a)) are showing that the R_p values vary between $2x10^5$ and $6x10^5 \, \Omega \, cm^2$ for both coatings. Apparently, the breakdown of the passive layer cannot be observed since no dramatic decrease of the R_p is observed at any chloride concentration. On the other hand, aged samples (1 year) are showing higher R_p values (*Figure 27* (b)): the highest resistance ($2x10^6 \, \Omega \, cm^2$) was obtained for both coatings in 0.001 M NaCl which was one order of magnitude higher than the "as obtained" samples. Although the R_p is maintained when using 0.01 M NaCl, there is a drop of the R_p when the concentration is increased to 0.1 M ($7x10^5 \, \Omega \, cm^2$ for the sulphate-based coating and $4x10^5 \, \Omega \, cm^2$ for the chloride-based coating). Such R_p values slightly continue decreasing as the concentration is increased to 1M NaCl. Therefore, a similar critical chloride content was found for the both Cr(III)-based coatings (between 0.01 and 0.1 M NaCl) where the sulphate-based system possessed a slightly higher R_p for 0.01 M to 1 M NaCl range. This could indicate a better corrosion resistance performance in comparison to the chloride-based system in this particular conditions.

As a summary, it seems that both Cr(III)-based coatings evolved with the time, reaching a higher corrosion performance for the aged samples in comparison to the *as obtained* ones (R_p was one order of magnitude higher tested in 0.001M NaCl). Moreover, the sulphate-based coating seems to behave better than the chloride-based one (further discussed in Annex B).

4.1.5 Summary of the chapter

The most important findings of this chapter are described below:

1. The chemical composition of the electroplated Cr layers obtained using both Cr(III)-based baths presented some differences:
   - Chloride presents higher C content (x2).
   - Sulphate has absorbed and adsorbed traces of S in the Cr layer (thiourea).
   - Chloride has a more amorphous structure.

   Whilst a higher Cr oxide/hydroxide to Cr metal ratio was observed for the sulphate system, as well as a thicker native oxide layer.

2. Despite the similar chemical nature (E_{fb}) and semiconductor behaviour (p type) of the native oxide layers formed on top of both Cr(III) systems, slight differences were observed on their semiconducting properties:
   - A more defective native oxide layer (higher point defects, N_A) was formed on the sulphate system, which was attributed to the presence of adsorbed S.
   - However, the electrochemically formed oxide layer (after removing the native one), presented a lower D_0 and i_{ss}, probably due to the absence of adsorbed S.

3. The sulphate system presented a slightly lower (2 times) R_p in the borate buffer electrolyte.
   - Such lower corrosion resistance was not observable when using a 0.1 M NaCl electrolyte, when studying immediately obtained samples.
   - However, when studying 1-year aged samples, the sulphate system was found to have a higher R_p even if it presented the same critical chloride content than the chloride system (0.01 - 0.1 M NaCl).

4.2 Effect of Fe on the properties of the obtained sulphate-based Cr electrodeposits and their performance

A model trivalent chromium-based electroplating bath was doped with different Fe content in order to study its effect on the electroplated coatings. The use of Fe is interesting as commercially is added to the baths to reduce the deposition time of the Cr electroplating process. Therefore, the impact that the Fe addition may have on the electroplated Cr layer as well as on the physicochemical properties of their native oxide layer was investigated. Furthermore, the possible modifications that the Fe may cause on the semiconducting properties of their native oxide layers as well as on their corrosion resistance performance was additionally explored. A detailed surface characterisation of the Cr layer and its native oxide film was made by X-ray Photoelectron Spectroscopy (XPS), Angle Resolved XPS (ARXPS) and Auger Electron Spectroscopy (AES). Moreover, the semiconducting properties were studied by Mott-Schottky and the corrosion performance by the Linear Polarisation Resistance (LPR) and kinetics of the oxide formation. Results revealed not only a homogeneous Fe distribution into the Cr layer but also the presence of an iron-chromium duplex oxide layer for concentrations ≥ 100 mg/L Fe in the bath. Mott-Schottky showed a p-n junction for such coatings due to the presence of an iron oxide layer on the top of a chromium oxide one, increasing the total amount of point defects (charge carrier density) which drastically affected the corrosion resistance (the polarisation resistance decreased by one order of magnitude and their oxide layer showed slower kinetics and higher passivation current). In contrast, coatings with a single chromium oxide layer behaving as p-type semiconducting showed the best corrosion performance (samples obtained from baths without Fe and with 8 mg/L Fe).

4.2.1 Chemical composition

4.2.1.1 Electroplated Cr layer (AES)

The *Figure 28* shows the AES depth profiles for the different Cr electrodeposits (the reference system without Fe and the three systems with different amount of Fe, Fe8, Fe100 and Fe400, containing respectively 8, 100 and 400 mg/L Fe in their electroplating baths), where the following elements were monitored as a function of the depth: Cr, C, O, S and Fe.
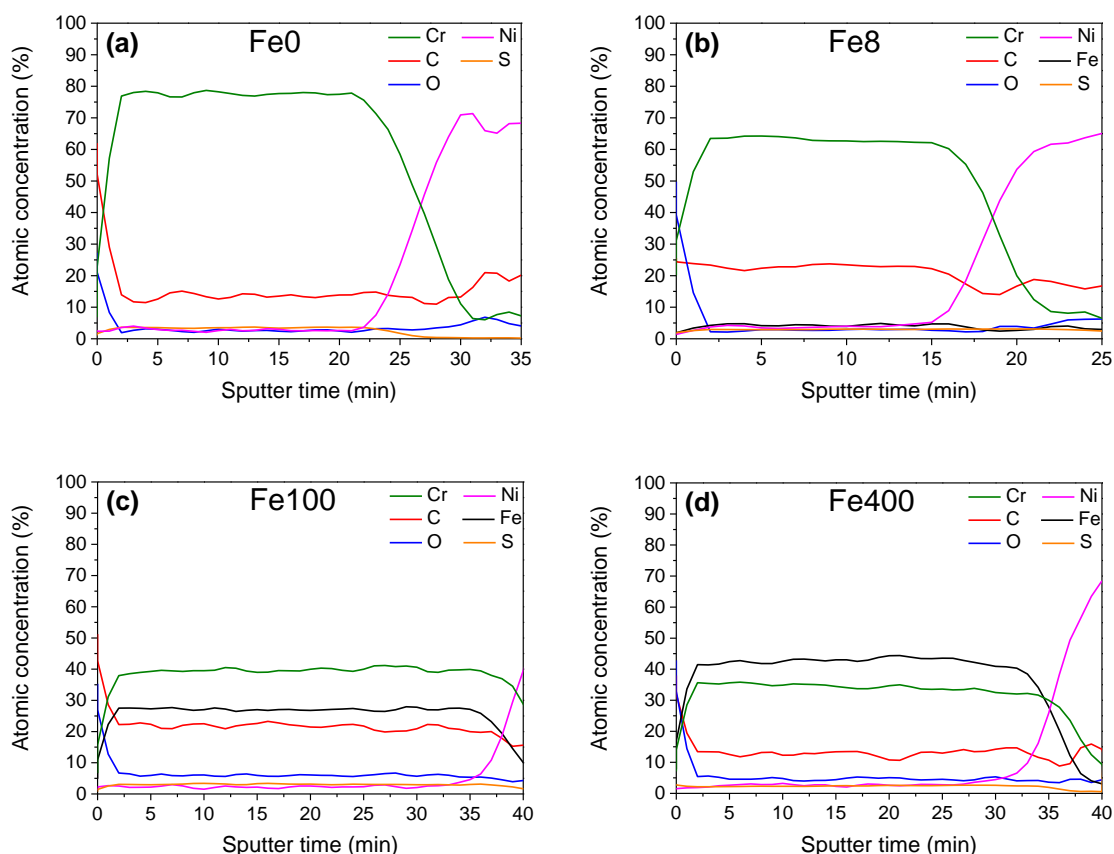
Figure 28*. AES depth profiles of (a) the reference sulphate-based Cr(III) coating without Fe, and the three coatings obtained using Fe doped baths, containing (b) 8, (c) 100 and (d) 400 mg/L of Fe, respectively.*

The C concentration in the Cr layer seems to be independent of the Fe concentration as it varies in the range of 10 - 25 % at. for all the coatings. Since organic additives are present in the electroplating process, C is expected to be present in the electroplated Cr layer [37,46,47,161]. The oxygen concentration is much higher at the beginning of the depth profile (at the surface) due to the presence of the native oxide layer. Although some residual atomic O was found inside the coating (i.e., beyond 3 minutes of sputtering), it was attributed to the high reactivity of Cr to spontaneously form an oxide layer even inside the ultra-high vacuum chamber at very low oxygen concentration; a similar effect was found elsewhere under similar oxygen concentrations [160].

Regarding to S, traces were also found through all the Cr layers, most probably due either to the adsorption or to the occlusions of sulphate-based salts or other organic additives (e.g., thiourea), as previously discussed in the chapter 4.1.

Finally, a Cr-Fe alloy was created according to the AES depth profiles above, where the Fe concentration in the coating increases as a function of the amount of Fe added to the electroplating bath (*Table 18).* The concentration of Fe varies from a 4 (Fe8 sample) up to 43 % at. concentration (Fe400 sample).

Table 18. Relation between the Fe added to the bath and present in the Cr layer (after 10 min sputtering).

[Fe] in electrolyte (mg/L)	[Fe] in Cr layer (% at.)
8	4.7 (1.1)
100	27.2 (0.3)
400	43.1 (0.8)

4.2.1.2 Electroplated Cr layer and native oxide layer (XPS)

In addition to the AES measurements, XPS high-resolution spectra of Cr, C, O, S and Fe were measured in order to obtain complementary information about the oxidation state of such elements in the electroplated Cr coatings. However, even after the Fe addition and independently of the presence of Fe (and its content), the Cr, O, C and S elements presented the same behaviour and chemical nature of the sulphate-based Cr coating without Fe (Fe0), since similar high-resolution spectra to the previously shown and already discussed in the chapter 4.1 were obtained (*Figure 16*).

The high-resolution spectra of the Fe $2p_{3/2}$ peak for Fe8 and Fe400 samples are shown in the *Figure 29*, where different trends were observed as a function of the Fe concentration of the bath. Due to the similar results obtained for Fe100 and Fe400 samples and for the sake of simplicity, from now on, only Fe400 data is shown.
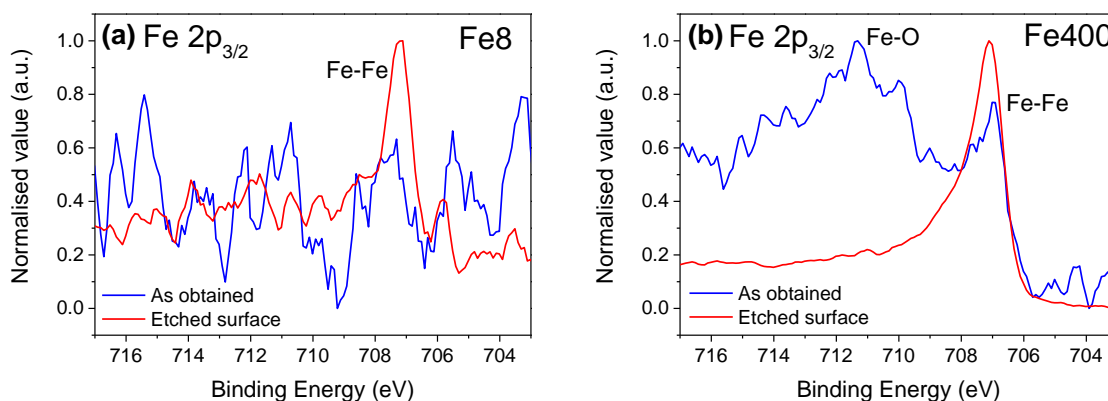
Figure 29. XPS high-resolution spectra (before and after the Ar ion etching) of the Fe $2p_{3/2}$ peak of (a) Fe8 and (b) Fe400 coatings.

Results showed the absence of Fe (Fe-Fe bond) at the surface for the Fe8 sample. In contrast, a broad peak centred at 711.0 eV (Fe-oxide/hydroxide species) [30,182] was observed for the Fe400 sample together with a peak at 707.0 eV (metallic Fe) [183,184]. After the etching, the later peak is also revealed for Fe8 sample whilst the peak at 711.0 eV disappears for Fe400 sample. These findings indicate a different composition of the surface

between Fe400 and samples Fe8, where the former seems to have Fe-oxide/hydroxide (Fe-O) species on the surface.

According to AES and XPS results, the addition of 8 mg/L Fe to the electroplating bath is enough to produce a Cr-Fe alloy coating but it does not lead to an electrodeposit which has Fe-oxide/hydroxide species in its native oxide layer, as it does the addition of 400 mg/L Fe. This fact is related to the Cr/Fe amount in the alloy, since the chemical composition and physicochemical properties of the native oxide layer are a function of the composition of the bulk material underneath, as well as are also function of the used electrolyte or media. It is known that the Cr is typically added to the steel, among other reasons, to increase the corrosion resistance behaviour due to the formation of a protective Cr oxide layer [185–187]. This effect has been only observed when the Cr is above a certain threshold, usually > 12 % at., when the corrosion resistance of the alloy increases abruptly at the same time that the Cr content increases in the oxide film [183,187,188]. In this specific case, the opposite effect is observed for the Fe100 and Fe400 samples since for the non-Fe containing sample there is a pure Cr oxide/hydroxide-based native oxide layer and, as the Fe content is increased in the alloy coating, the Cr amount decreases until certain threshold (somewhere between 4 and 43 % at. concentration Fe in the coating) where the Fe starts to be more dominant in the reactions and mechanisms of the formation of the native oxide layer, and finally iron oxide is formed in the oxide film.

Additional XPS depth profile measurements were performed to explore the composition of the native oxide layer of the Fe400 sample, by studying the Cr 2p and Fe 2p spectra (*Figure 30*). The evolution of the Cr and Fe 2p peaks as a function of the sputtering shows a relatively high contribution of metal-oxide signals due to the presence of the native oxide layer (576.8 eV for Cr and 711.0 eV for Fe) at the beginning (sputtering time 0). A significant decrease of those oxide-related components occurs during the sputtering, increasing the contribution of both metallic components (574.2 eV for Cr and 707.0 eV for Fe).
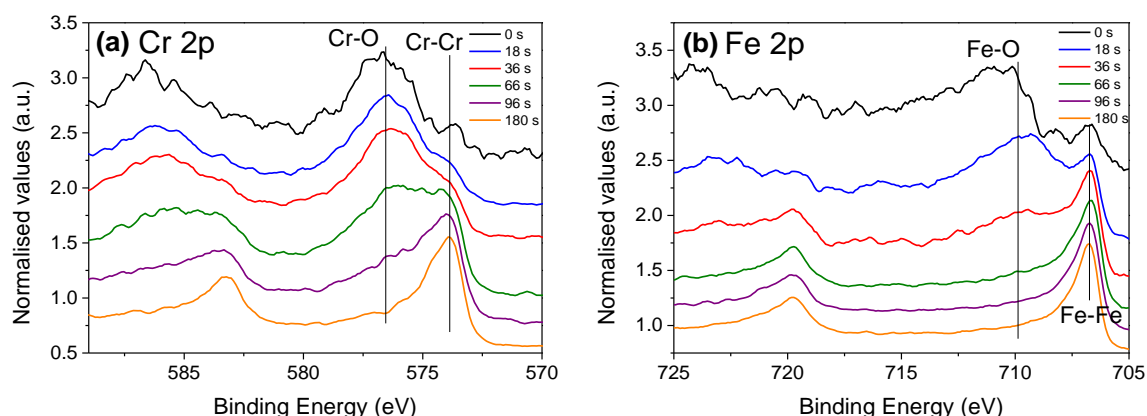
Figure 30. *Representative XPS high-resolution spectra of the (a) Cr 2p and (b) Fe 2p peaks for the Fe400 sample as a function of the sputtering time during the depth profile experiment.*

Interestingly, a selective etching of the iron oxide layer in comparison to the chromium oxide (the ratio of Cr-O/Cr peaks remains constant) was observed from 0 to 36 s. In fact, the signal corresponding to the Fe oxide/hydroxides (Fe-O) disappears after 66 s of sputtering whilst the Cr oxide/hydroxide signal (Cr-O) remains until disappearing completely after 180 s). It seems that the native oxide layer of Fe400 (and Fe100) sample may be formed by a duplex film, having an outer Fe-rich and an inner Cr-rich oxide/hydroxide layer. A similar finding was observed by other authors when studying stainless steel samples [74,172,189].

In order to confirm the hypothesis of the duplex native oxide layer, ARXPS measurements were run modifying the take-off angle (20 – 80 º) and avoiding side effects during the Ar ion sputtering in depth profile experiments (e.g., inhomogeneous sputtering of the surface). Information of such oxide layers was obtained at different angle/depth (the higher angle, the deeper analysed spot) using *as obtained* samples (without any previous sputtering). Initially, only the Fe 2p spectra was analysed; however, due to the complex deconvolution of the Fe-O peak (i.e., overlapping of satellites), the Fe 3p spectra was also measured (*Figure 31*) in order to elucidate the Fe oxidation states and the ratio of Fe^{3+}/Fe^{2+}[190,191].
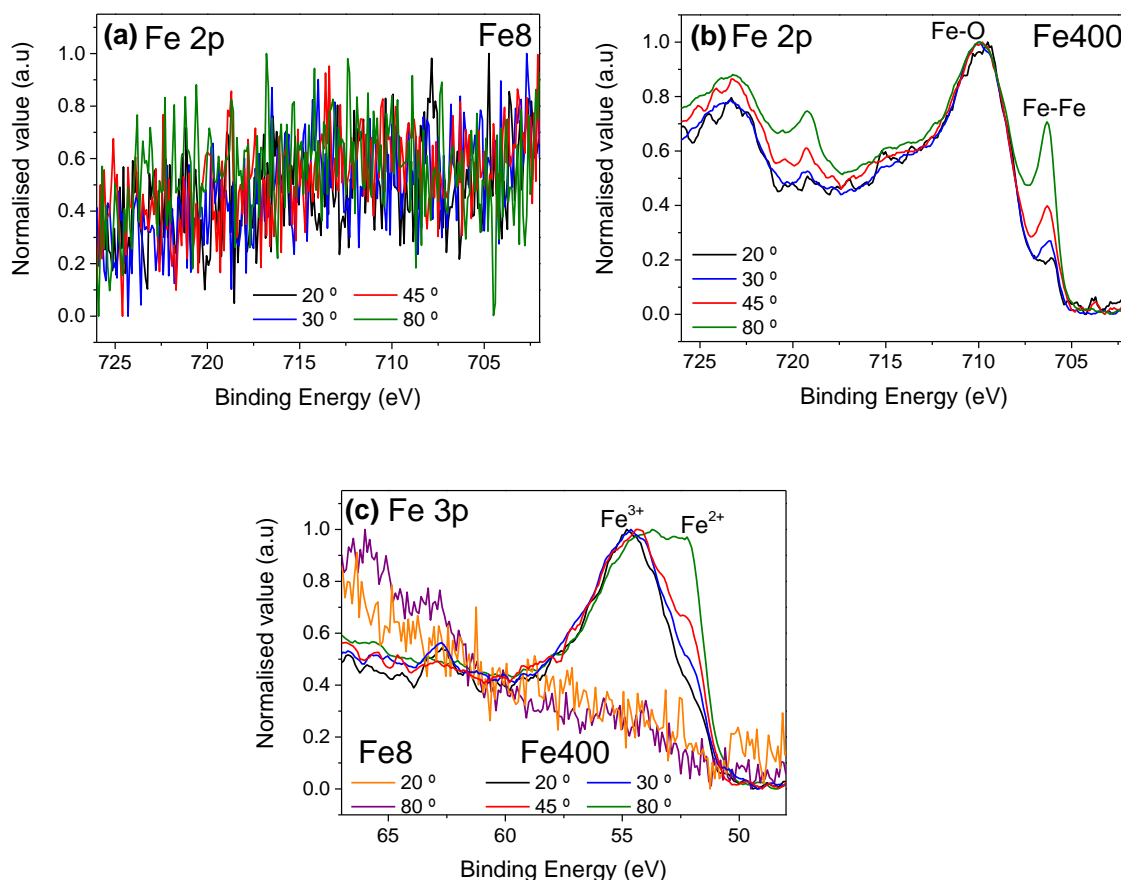
Figure 31. *ARXPS measurements of: i) the Fe 2p for (a) Fe8 and (b) Fe400 samples, and ii) the Fe 3p for (c) both samples (Fe8 and Fe400).*

In agreement with the previous XPS results, Fe8 sample did not show the presence of Fe in its native oxide layer at any take-off angle (*Figure 31* (a)), neither in the more superficial (< 45 º) nor in the deeper measurements (> 45 º). In contrast, the Fe400 sample possesses a strong Fe oxide (Fe-O) contribution at all angle/depth value in the Fe 2p spectra (*Figure 31* (b). Furthermore, the intensity of the metallic Fe-Fe peak increases as a function of the take-off angle, if the measurement goes deeper, lower volume of Fe oxide is measured or, what is the same, more metallic Fe is being measured. In order to study the different oxidation states of the Fe in such oxide layer, the Fe 3p spectra was also analysed (*Figure 31* (c)). The *Table 19* shows the quantification according to the different chemical states of the Fe (Fe^{3+}/Fe^{2+}) as well as the Cr/Fe ratio, respectively.

Table 19. Ratio of the metallic elements present in the native oxide layer of Fe400, studied by ARXPS.

Take-off angle (°)	Fe^{3+}/Fe^{2+}	Cr/Fe
20	0.9	0.63
30	1.3	0.60
45	1.1	0.63
80	0.5	2.00

It can be observed that, in the case of Fe400, there is iron oxide on the surface (20 º), constituted by approximately 50 % of Fe^{2+} and Fe^{3+}. In contrast, at the highest angle (80 º, corresponding to the deepest measurement) the Fe^{2+} signal becomes 2 times higher than Fe^{3+}. At the same time, if the content of Cr and Fe are compared, it can be observed that the maximum amount of Fe is located on the surface (Cr/Fe ratio is lower than 1 and only at 80 º the ratio increases to 2). These findings support the hypothesis of the duplex oxide film in Fe400 and in Fe100 samples. A similar behaviour has been previously observed in some stainless steels [192–194], where the Fe concentration in the bulk was high enough to form an iron oxide layer on top of a Cr oxide film. It is assumed that, initially, the Fe is preferentially dissolved to form an outer oxide layer (via formation of bivalent iron hydroxide). During the Fe oxide formation, the chromium is also oxidised through the still-forming oxide layer and through its boundaries to create an inner chromium hydroxide film (and further dehydrated) which eventually is covered by the iron oxide [195]. Under the scenario of this research, a similar oxide formation mechanism is also possible because of the higher mobility of Fe cations in comparison with the Cr ones [58,192]. Indeed, the presence of Fe oxide species (mainly Fe^{2+} according to the $Fe^{3+}/Fe^{2+}= 0.5$) into Cr oxide layer (80º take-off angle where Cr/Fe= 2.0) is in agreement with the presence of simultaneous oxidation reactions of Fe and Cr, where certain amount of Fe^{2+} species are occluded into the chromium oxide layer before reaching the outer iron oxide layer.

4.2.2 Semiconducting properties of the oxide layer

4.2.2.1 Mott-Schottky

Previously to the Mott-Schottky measurements, potentiodynamic polarisation curves were obtained to identify the passive region of the Cr coatings and to define the potential range for such experiment. The *Figure 32* shows the anodic branches in the borate buffer electrolyte (pH 8.4). The potential range in terms of passive region for Fe0 and Fe8 samples was similar, comprising approximately from E_{OCP} (- 0.25/- 0.3 V) to + 0.4 V (approximately the breakdown potential for both samples). However, the passive region of Fe100 and

Fe400 was found to be much larger, where the Fe400 sample did not show any breakdown potential up to 1.0 V. The transpassive dissolution of Cr occurs for Fe0 and Fe8 at approximately 0.4 - 0.5 V, being the Cr oxidised from Cr(III) to Cr(VI). Therefore, the iron will mainly govern the electrochemical behaviour at such potentials [74] in the samples with higher Fe concentration (Fe100 and Fe400). In fact, a similar behaviour was observed in the passive region of stainless steel samples in the literature [60,64,196], which are generally featured by two anodic peaks: the first one located approximately at 0 V which will be attributed to the oxidation of Fe(II) to Fe(III) whilst the second one, observed at approximately 0.6 V, which would correspond to the oxidation of Cr(III) to Cr(VI) as previously mentioned for Fe0 and Fe8 [197–199]; oxidation from Cr to Cr^{3+} and Fe to Fe^{2+} occurs prior to the first anodic peak, in the active region.

A shift of approximately 300 and 600 mV was observed for the breakdown potential of Fe100 and Fe400 respectively, in comparison to Fe0/Fe8 samples. This is probably caused because at high anodic potentials (0.6 - 1 V), as previously mentioned, the iron is ruling the electrochemical response, as the Cr is dissolved at lower potentials, and as a result, the polarisation curves are similar to the ones of iron and stainless steel, having a characteristic higher breakdown potential and consequently, a larger passive region.
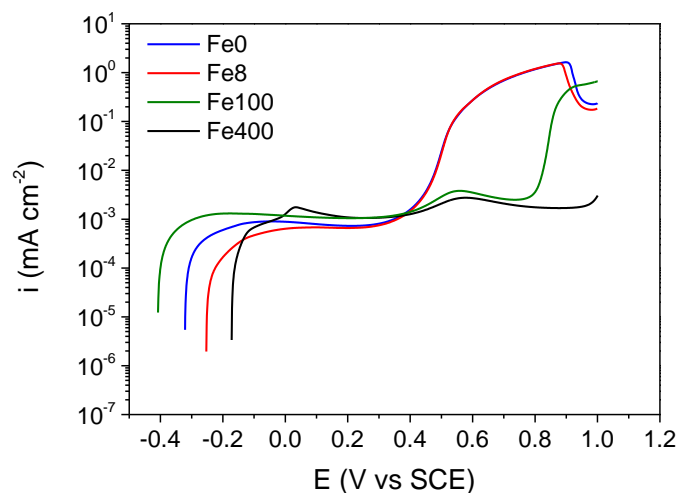
Figure 32. *Polarisation curves of the Fe0, Fe8, Fe100 and Fe400 coatings in borate buffer electrolyte.*

The Mott-Schottky plots of the native oxide layers are shown in the *Figure 33* where two different trends as a function of the Fe concentration were observed. Typical negative slopes of p-type semiconductors were observed for all samples where the chromium vacancies (V_{Cr3+}) were the main charge carriers or point defects in the native oxide layers. Such defects were acting as acceptor dopants in the Cr oxide layer [60,72,172]. In addition to the p-type behaviour, positive slopes (characteristic of n-type semiconductors) were only

observed for Fe100 and Fe400 samples. In those cases, Fe interstitials and oxygen vacancies were the main charge carriers. According to previous studies, the p-type behaviour (negative slope) corresponds to the Cr oxide layer [72] whilst the n-type behaviour (positive slope) corresponds to the Fe oxide [200,201]. Moreover, Mott-Schottky plots show a p-n heterojunction due to the p-type inner Cr oxide and n-type semiconducting behaviour of the outer Fe oxide layer [73,126,172,202]. This is in agreement with the previous results (*Figure 30* and *Figure 31*) where Fe100 and Fe400 samples showed a duplex oxide layer constituted by an outer Fe oxide layer and an inner Cr oxide layer. This modification of the semiconducting behaviour of the native oxide layer for Fe100 and Fe400 samples may have an impact on their protection ability (it will be discussed in section 4.2.4.2).
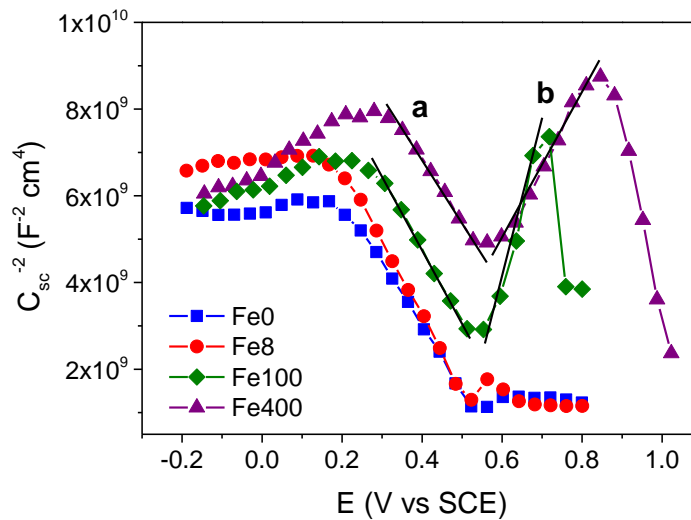
Figure 33. Mott-Schottky plots of Fe0, Fe8, Fe100 and Fe400 coatings.

In addition to the semiconductor type behaviour of the oxide film, the charge carrier density (N_q) was calculated using the *Equation 5* and *Equation 6* as acceptor density (N_A) or donor density (N_D), as well as the acceptor and/or donor flatband potential (E_{fb}). The *Table 20* shows the results obtained for the different systems. The charge carrier density can be understood as an intrinsic value that indicates the degree of point defects inside the oxide film, which are also related to different features (e.g., the protection ability of such oxide films). In general, the lower the N_q, the more limited the charge transfer is, hindering superficial electrochemical reactions such as corrosion events [180,203,204]. The obtained Nq values are ranged around 10^{20} cm^{-3} for all coatings, such values are in agreement with the ones obtained in other studies on Cr or Cr-Fe alloys, which are usually in the range 10^{19} - 10^{22} cm^{-3} [60,70,72,73,115]. Although there are no significant differences in the N_A of the

p-type semiconducting behaviour for all systems, the n-type semiconducting behaviour reveals more defects (N_D), specially for the Fe400 sample compared to Fe100, making their native oxide layer more defective.

Table 20. *Electronic properties obtained from the Mott-Schottky plot for the reference and Fe-containing Cr coatings.*

Added [Fe] (mg/L)	N_A ($\times 10^{20}$ cm^{-3})	N_D ($\times 10^{20}$ cm^{-3})	E_{fb} acceptor (V vs SCE)	E_{fb} donor (V vs SCE)	Semiconductor type
0	8.0 (0.3)	-	0.57 (0.01)	-	p
8	6.7 (0.4)	-	0.57 (0.01)	-	
100	[a]7.4 (0.6)	[b]3.4 (0.4)	[a]0.65 (0.01)	[b]0.47 (0.02)	[a]p // [b]n
400	[a]8.4 (0.5)	[b]6.8 (1.0)	[a]0.86 (0.01)	[b]0.30 (0.04)	

[a]Results for the negative slope (p type) in the range 0.3-0.5 V (using Equation 5)
[b]Results for the positive slope (n type) in the range 0.6-0.8 V (using Equation 6)

Regarding the E_{fb}, it represents the region at which there is no depletion layer at the p-n-type junction. At this potential, there is no electrostatic potential gradient (no band bending) in the oxide film [118]. Results are showing some modifications in the E_{fb} values, which can be explained by the modification of the chemical composition of the oxide layer and the different proportion of Cr and Fe in such oxide films (*Figure 29* and *Table 19*). For the p-type Cr oxide layer, an increase of the acceptor E_{fb} is observed in the following order: Fe0 = Fe8 < Fe100 < Fe400. Although the E_{fb} did not change after adding a small amount of Fe (Fe8) in comparison with the reference coating (Fe0), significant changes were obtained for Fe100 and Fe400 samples. This increase of the E_{fb} could explain the shift of the breakdown potential in the polarisation curve to more positive values when increasing the iron content (*Figure 32*). In the case of the n-type Fe oxide layer, an opposite trend is observed for the donor E_{fb} which decreases with the amount of Fe. This shift is believed to be caused by the increase of iron content in the sample (Cr-Fe alloy and outer oxide layer) and explained by the more negative E_{fb} of the oxide formed on pure iron [64,126,205,206].

4.2.3 Corrosion resistance evaluation of the Cr coating and oxide film

4.2.3.1 Kinetics of the oxide layer formation

Current-time transients (*Figure 34*) were measured to investigate the impact of the Fe content on the oxide layer formation kinetics. If the different curves are compared, two separated groups but with similar trend were observed: the reference non-Fe containing coating (Fe0) and all samples with Fe, respectively. This finding clearly would indicate that

the kinetic of the oxide layer formation was affected by the presence of Fe in the electroplated coating, even when Fe was added in smaller amounts (Fe8).
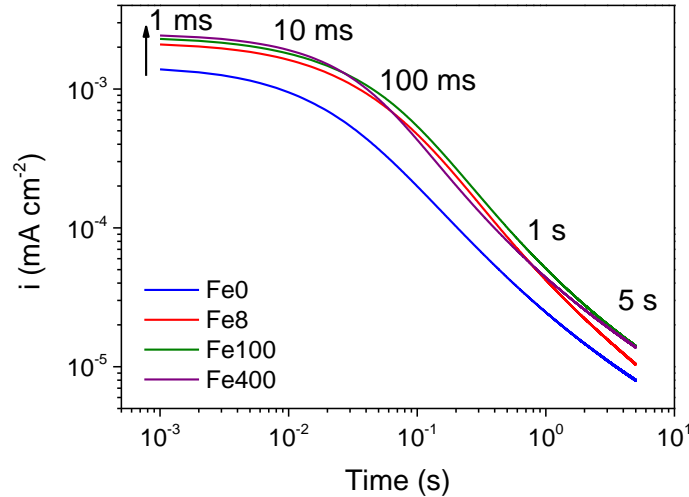
***Figure 34.** Passivation kinetics or current-time transients measurements of Fe0, Fe8, Fe100 and Fe400 coatings.*

In order to explain it, *Table 21* gathers the parameters that are obtained from the fitting the current-time transients in the range 20 - 60 ms of passivation time (corresponding to the oxide formation stage). Since the value of the *n* parameter was decreased for the Fe-containing coatings in comparison to Fe0, the presence of Fe into Cr(III) sulphate-based electrodeposits has a detrimental effect on the oxide layer formation kinetics. This parameter is proportional to the oxide layer formation velocity, typically lower values are characteristic of porous and poorly protective oxide films [148–150]. Moreover, the passivation current density measured at the beginning of the passivation (i_0) also increased with the amount of iron in the electroplated coating. This was in agreement with the statement above, since in general, higher current values involve a higher superficial reactivity, increasing the passivity breakdown susceptibility. In that sense, although Fe8 and Fe100 samples were showing similar *n* values (0.70), the current seemed to be slightly higher for the Fe100 sample, and therefore, a lower corrosion protection will be expected.

***Table 21**. Obtained parameters from the linear fitting (20-60ms) of the passivation kinetics measurements.*

Sample	n	i_0 (mA cm^{-2})
Sulphate (No Fe)	0.74 (0.06)	1.4 (0.2)
Fe8	0.70 (0.15)	1.5 (0.6)
Fe100	0.70 (0.17)	2.0 (0.3)
Fe400	0.67 (0.12)	2.7 (0.2)

Finally, according to the current-time transients curves, the following protection of the oxide layer is expected: Fe0 > Fe8 ~ Fe100 > Fe400.

4.2.3.2 Corrosion resistance evaluation

PDP and LPR measurements were carried out to evaluate the corrosion resistance performance of the Fe-doped Cr(III)-based electrodeposits compared to the reference Cr coating. The experiments were conducted in both borate buffer and 0.1 M NaCl electrolyte to compare the corrosion protection in different aggressive conditions. No significant difference was observed between the samples in the PDP experiments (not shown here) when using the 0.1 M NaCl. However, the passive region observed in borate buffer electrolyte (*Figure 32*) was disappeared, as well as the breakdown potential was decreased, probably due to the higher aggressiveness of the medium. The *Table 22* shows the polarisation resistance (R_p) values that were obtained after doing a linear fitting following the Ohm's Law using both electrolytes.

Table 22. *Polarisation resistance values obtained from the LPR measurements for the reference and Fe-doped sulphate-based Cr(III) coatings.*

Sample	R_p (x10^5 Ω cm^2)	
	Borate buffer (pH 8.4)	**0.1 M NaCl**
Fe0	1.0 (0.1)	1.5 (0.4)
Fe8	2.2 (0.2)	1.3 (0.3)
Fe100	1.3 (0.1)	0.9 (0.1)
Fe400	1.0 (0.1)	0.7 (0.2)

On the one hand, despite the differences observed in the PDP measured in borate buffer electrolyte (*Figure 32*) no clear trend was observed in the R_p value as a function of the Fe, since the calculated values for the Fe0 and Fe400 were practically the same. An increase in the R_p was observed for the Fe8; however, it was not considered significant due to the similitudes found between the Fe0 and Fe8, being attribute probably to a repeatability issue between different batches of samples. In general, it seems that the borate buffer electrolyte does not have the enough aggressivity to show differences between this samples.

On the other hand, when studying the polarisation resistance value obtained using 0.1 M NaCl electrolyte, a decreasing trend was observed as a function of the added Fe. It can be observed that the addition of 8 mg/L Fe to the electroplating bath does not modify significantly the corrosion resistance of the reference Cr coating. However, when adding 100 or 400 mg/L Fe to the bath, the R_p decreases reaching values almost one order of

magnitude lower, exhibiting a worst corrosion resistance. This is in agreement with the detrimental effect caused by the iron species in the native oxide layer of Cr-Fe alloys [207,208]. Moreover, having a Cr oxide layer doped with other elements also have a negative impact in the corrosion resistance in comparison to a purely constituted Cr oxide film [186].

Apparently, there is a critical value between 5 and 27 % of Fe content into the alloy (Table 18) that trigger the formation of a native duplex oxide layer (Fe100 and Fe400 samples, Figure 31) rather than a pure Cr oxide-based layer (Fe0 and Fe8 samples, Figure 16 and Figure 29, respectively). The presence of Fe in the native oxide layer is promoting the formation of a defective and poorly protective oxide layer due to the higher passivation currents (Figure 34), lower oxide formation kinetic (Table 21) and additional highly defective n-type semiconducting behaviour (Figure 33). In contrast, since the N_A did not change significantly, the grade of point defects of the Cr (p-type, *Table 20*) was not affected independently of the Fe content. It can be explained analysing the Mott-Schottky measurements, where the charge carriers of the surface are under different scenarios as a function of the applied potential. Since the passive region of a p-type semiconductor is normally below the E_{fb}, a depletion of positive holes occurs in the space charge of the oxide film. Under this first scenario, the surface will be negatively charged, minimizing the anion adsorption and enhancing the resistance to pitting corrosion (e.g., limiting Cl^- ions mobility). In contrast, a depletion of electrons occurs at potentials above the E_{fb} for a n-type semiconductor, and therefore, the surface will be charged positively [135,209]. This is the reason why passive films exhibiting n-type semiconducting behaviour generally have a higher susceptibility to pitting corrosion, being the donor density a representative feature of the affinity of Cl^- ions for the passive film or the pit nucleation ability [210–212].

Therefore, the addition of 8 mg/L of Fe to the sulphate-based Cr(III) bath increases the deposition rate providing similar corrosion resistance than the reference coating (Fe0.In contrast, although Fe100 and Fe400 improved the deposition rate much more than Fe8, the corrosion resistance was drastically affected due to their naturally formed duplex oxide layer. A critical Fe concentration (between 8 - 100 mg/L) in the bath could be further explore to reach the best deposition time/corrosion resistance relationship.

4.2.4 Summary of the chapter

Below the findings of this chapter are listed:

1. The Fe addition to the sulphate-based electroplating bath has a great impact on the physicochemical properties of the Cr layer, and as a consequence, on the native oxide layer.

2. Adding 8 - 400 ppm Fe to the bath makes Fe to codeposit in the Cr layer forming a Cr-Fe alloy (8 - 43 % at. Fe respectively in the electroplated layer).

3. Fe oxide is present in the native oxide layer when > 100 mg/L Fe are added to the bath, forming a duplex native oxide layer (outer Fe rich and inner Cr rich).

4. The presence of Fe in the native oxide layer (> 100 mg/L), affects dramatically to the semiconducting properties of such films and to the oxide layer formation kinetics.
   - New n-type semiconducting behaviour with higher point defects.
   - Different E_{fb} (chemical nature).
   - Slower oxide layer formation kinetics and higher passivation current.
   - Lower corrosion resistance, featured by a 1-order of magnitude lower R_p.

4.3 Hexavalent vs trivalent based Cr coatings

The native oxide layer of decorative Cr coatings obtained from trivalent and hexavalent chromium-based electroplating baths have been evaluated and characterised in detail, as well as their electroplated Cr layer. On the one hand surface sensitive techniques have been such as Synchrotron radiation-based X-ray Absorption Spectroscopy (XAS/XANES), Auger Electron Spectroscopy (AES) and X-ray Photoelectron Spectroscopy (XPS) have been used to explore the chemical composition of both Cr and oxide layer. On the other hand, electrochemical measurements were performed to evaluate the semiconducting properties by Mott-Schottky, Point Defect Model (PDM), as well as the corrosion resistance by studying its oxide formation kinetic, linear polarisation resistance (LPR) and potentiodynamic polarisation (PDP). Results have revealed a completely different behaviour between samples in most of the properties. The Cr(VI)-based electroplated Cr layer resulted to have a total absence of C and a more amorphous structure, as well as more Cr oxide/hydroxide- rich native oxide layer, which was constituted mainly by Cr hydroxides. Despite having a single Cr_2O_3 oxide layer, synchrotron-based measurements revealed the presence of a unique topmost CrO_3 thin film on the surface of the Cr(VI)-based Cr electrodeposits, which was believed to provide enhanced semiconducting properties to the native oxide layer, resulting in an outstanding corrosion capabilities in comparison to the Cr(III)-based coating.

4.3.1 Electroplated Cr layer

4.3.1.1 Chemical composition by AES and XPS

AES fast depth profiles (*Figure 35*) revealed that the Cr layer obtained when using a Cr(VI)-based electroplating bath was constituted by a homogeneous pure Cr layer, having a total absence of C unlike the Cr(III)-based systems, where a relative high C content was found in the electroplated Cr layer (due to the presence of organic additives that are used in the Cr(III)-based electroplating baths and are not used in the Cr(VI)-based ones (*Table 7*). In fact, the C signal of the Cr(VI) system remained negligible and constant almost until the Cr-Ni interphase was reached (after approximately 20 - 25 min). In contrast to Cr(III)-based coatings (sections 4.1 and 4.2), the signal of the C spectra was constituted by a noisy background (leading to the quantification of an artifact signal), confirming the absence of C on the Cr layer (validated also by the XPS high-resolution spectra).
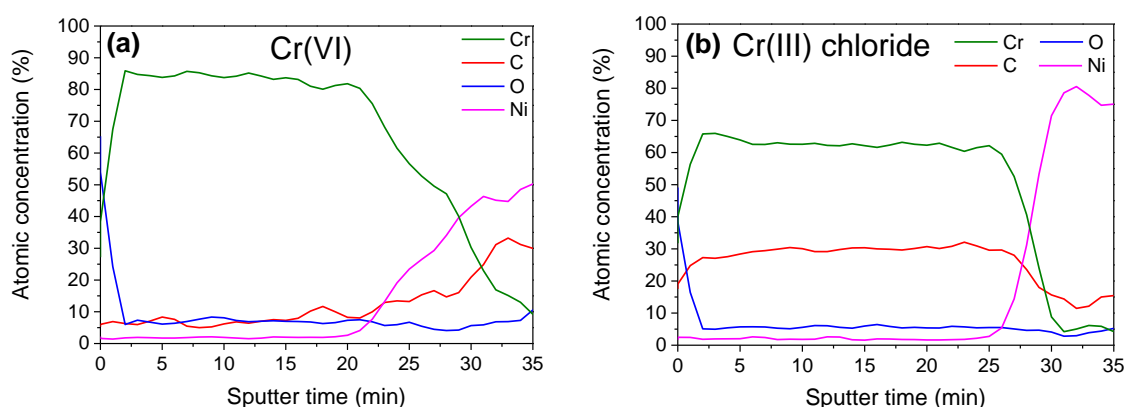
Figure 35. AES depth profiles of (a) Cr(VI) and (b) Cr(III)-based (chloride system) Cr coatings.

The *Table 23* shows the chemical composition measured by XPS of the surface before and after sputtering the surface (approximately 10 nm of penetration depth after etching) for both Cr coatings.

Table 23. Chemical composition, measured by XPS, corresponding to the surface and Cr layer after Ar ion sputtering (approx. 10 nm).

atomic %		*Cr*	*C*	*O*	*S*
Cr(VI)	Surface	12.7 (-)	37.3 (-)	46.6 (-)	3.5 (-)
	Etched	81.4 (-)	4.6 (-)	13.3 (-)	0.7 (-)
Cr(III) chloride	Surface	8.5 (5.2)	54.5 (21.4)	37.1 (16.1)	-
	Etched	70.1 (0.6)	20.2 (0.1)	9.7 (0.6)	-

On the one hand, the results corresponding to the non-etched surface followed a similar trend for both Cr(VI)-based and Cr(III)-based Cr coatings. As mentioned previously, typically, the surface is covered by a high C and O concentration corresponding to contamination (adventitious C together with adsorbed organic components). Additionally, traces of S were detected on the surface of the Cr(VI)-based coating, similarly to the sulphate-based Cr(III) coating (*Table 11*), most probably due to adsorbed sulphate ions coming from the electrolyte.

On the other hand, the etched surface is constituted by high Cr content (as it was expected once the contamination layer and the oxide were sputtered away). The oxygen present in the etched surface of both coatings was already discussed in the chapter 4.1 and attributed to a repassivation phenomenon of the Cr. Regarding to the C, it was only observed in the Cr(III) chloride-based coating and corresponds to the inclusions of organic additives. Finally, no S were found on the etched surface of the Cr(VI)-based coating.

The high-resolution spectra (*Figure 36*) of the main elements present in the Cr(VI)-based electrodeposits were acquired to study their chemical nature and oxidation states (Cr $2p_{3/2}$, C 1s, O 1s and S 2p). The high-resolution spectra belonging to Cr(III) chloride-based systems were shown in the *Figure 16*, with the exception of the S, element that it was only present for the sulphate systems.
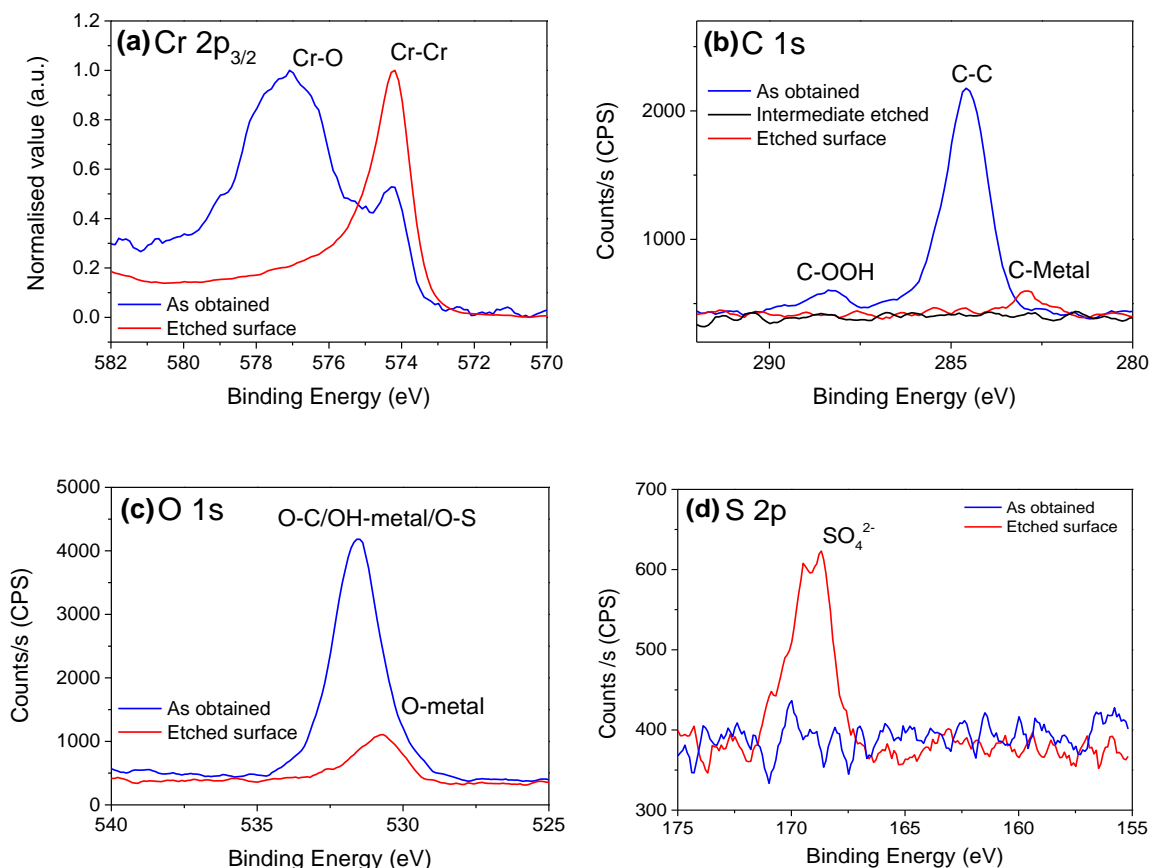
Figure 36. *XPS high-resolution spectra of (a) Cr $2p_{3/2}$, (b), C 1s, (c). O 1s and (d) S 2p (d) of the electroplated Cr(VI)-based coating, as a function of the depth.*

The Cr and O high-resolution spectra provided the same information than for the Cr(III)-based coatings: Cr oxide/hydroxide at the surface and mainly metallic Cr into the coating (already discussed in chapter 4.1). Regarding C 1s, as previously observed in the XPS chemical composition (*Table 23*), it is only present on the *as obtained* surface, corresponding to the C adventitious and organic contamination layer (C-C and C-OOH peaks found at 284.6 and 288.3 eV respectively), no C is detected inside the coating (*Figure 36* (b), *intermediate etched* surface), but it should be noted that after longer sputtering times (*Figure 36* (c), *etched surface*), a carbide C signal appears at 282.9 eV, as a result of the reduction effect caused by the sputtered energetic Ar ions as; this effect was previously observed in the literature [213]. The time at which the metallic Cr layer of the Cr(VI)-based coating suffers this effect (approximately between 100 and 160 s of Ar ion sputtering) is an

useful reference to confirm that the carbide signal measured in the Cr(III)-based systems (*Figure 16* (b)) are inherent carbides present in the electroplated coatings because they were detected long before that critical sputtering time; after that time an increase in the C content was observed in all systems due to this mentioned effect.

The S 2p spectra (*Figure 36* (d)) shows that the sulphur present in the *as obtained* surface is constituted by adsorbed sulphate ions, probably coming from the H_2SO_4 electrolyte used in the Cr(VI)-based electroplating baths. That sulphur was completely removed after etching the surface.

4.3.1.2 Morphology

The surface morphology of both Cr-based coatings was explored by means of FE-SEM. *Figure 37* shows the morphology of both Cr electrodeposits. As mentioned before, the Cr(III)-based coatings (*Figure 37 (b)*), present a nodular morphology with different sizes due to their electroplating mechanism [4,56,167,168], whilst the Cr(VI)-based coatings (*Figure 37 (a)*) has a more rough and homogeneously distributed surface with smaller nodules [44,49,214].
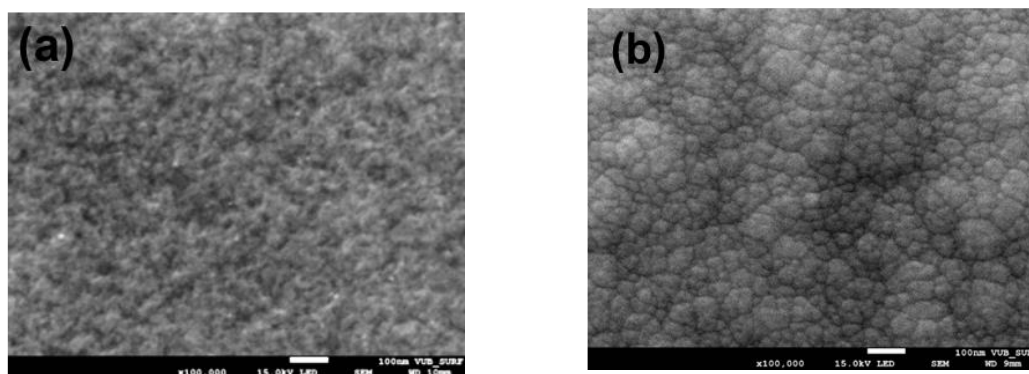
Figure 37. *Surface morphology of (a) Cr(VI) and (b) Cr(III)-based electrodeposits.*

4.3.1.3 Crystalline structure

XRD experiments (*Figure 38*) revealed that the Cr(VI)-based coatings were completely amorphous, presenting no peak in the diffractogram. The Cr(VI)-based Cr electrodeposits have been found to be amorphous or crystalline, depending on the chemical composition of the electroplating bath, as well as, on the electrodeposition conditions, having the current density a high impact [42,49]. In contrast, the Cr(III)-based system, possess a broad peak belonging to the Cr and an overall amorphous structure, caused by the high C content in the Cr layer as it was discussed previously in the chapter 4.1.
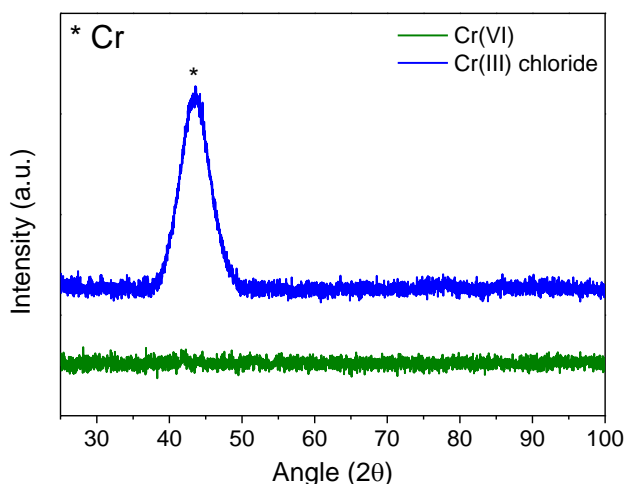
Figure 38. *XRD diffractograms of the C(VI) and Cr(III)-based coatings (green and blue respectively).*

4.3.2 Native oxide layer formed on top of the Cr coatings

4.3.2.1 Chemical composition

The chemical composition of the native oxide layers of both systems were calculated (*Table 24*) based on the deconvolution of the Cr $2p_{3/2}$ peak of XPS using the multiplet splitting effect (*Figure 39*).
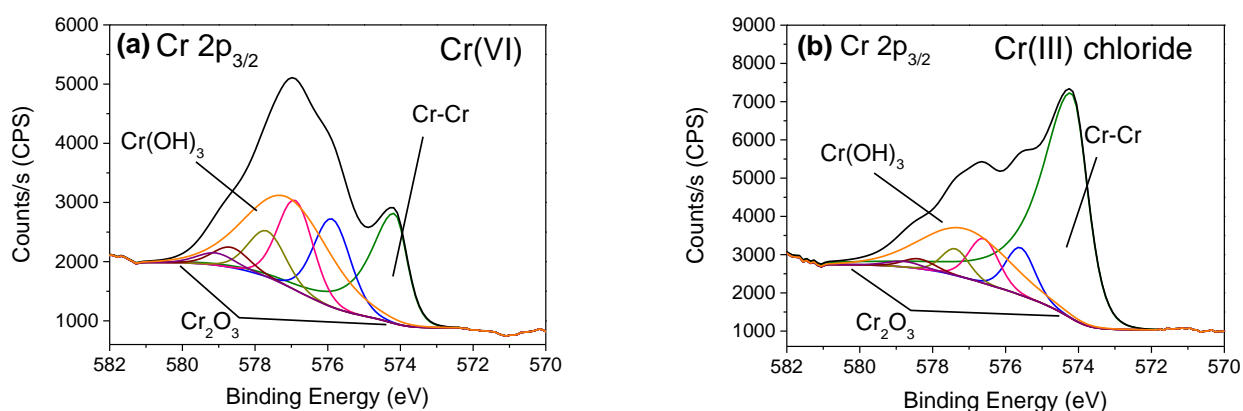
Figure 39. *Deconvolution, considering the multiplet-splitting effect, of the Cr $2p_{3/2}$ peak of the (a) Cr(VI)-based and (b) Cr(III)-based chloride coatings.*

Table 24. *Analysis of the Cr $2p_{3/2}$ high-resolution peak of the native oxide layer of the Cr(VI) and Cr(III)-based coatings.*

Atomic %	Cr-Cr	Cr-O		Cr_2O_3	$Cr(OH)_3$
Cr(VI)	21.3 (-)	78.7 (-)		9.7 (-)	69.0 (-)
Cr(III) chloride	51.8 (3.2)	48.2 (3.2)		13.8 (6.6)	34.3 (3.2)

At a first sight, it can be observed that the Cr-O component of the Cr(VI)-based coating is much larger that its metallic contribution. According to the *Table 24*, the native oxide film formed on Cr(VI) systems possess the highest oxide/hydroxide contribution (Cr-Cr/Cr-O ratio of 21.3/78.7) compared to the Cr(III)-based coatings (Cr-Cr/Cr-O ratio of 51.8/48.2). This difference can be due to the different conditions of the electroplating baths. Even if the Cr(III)-based baths are known to work under acidic pH (pH 3), the Cr(VI)-based ones are extremely acidic (they are mainly constituted by high concentrations of H_2SO_4, *Table 7*). At such low pH, the chromium solubility is increased and as a result, the concentration of Cr-O in comparison to Cr-Cr [171,215,216]. Regarding to the type of oxide/hydroxide, both coatings are showing a similar amount Cr_2O_3, whilst the amount of $Cr(OH)_3$ was much higher for the Cr(VI) system (69 %) in comparison to the Cr(III) chloride one (34.3 %).

In addition to conventional surface analysis techniques such as AES or XPS, the samples were also studied in a synchrotron facility by using the XAS technique (*Figure 40*). Total electron yield (TEY) measurements were carried on the Cr L edge together with C and O K edge.
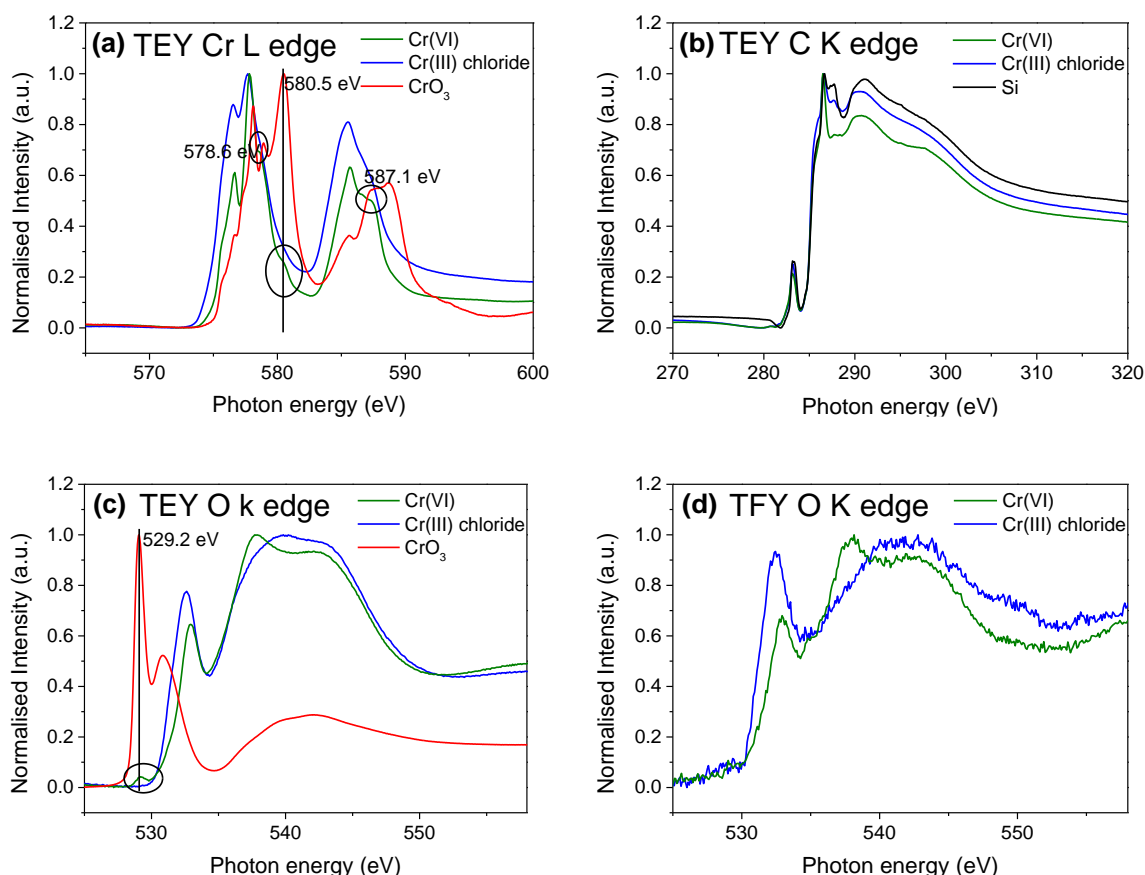
***Figure 40**. XAS measurements in TEY mode of the (a) Cr L edge, (b) C K edge, (c) O K edge and (d) TFY mode O K edge on electroplated Cr(VI) and Cr(III) chloride-based coatings.*

The Cr L edge spectra (*Figure 40* (a)), shows similar shapes and peaks for both Cr coatings, corresponding mainly with the signals of a the Cr_2O_3 standard (not show here) [217,218]. However, the Cr(VI)-based sample presented a higher relative intensity for the peaks located at 578.6 and 587.1 eV, which were attributed to the Cr_2O_3 (the intensity difference was slightly attenuated by the normalisation of the data). This could indicate a possible thicker native oxide layer of the Cr(VI) system. In addition, an extra shoulder was observed at 580.5 eV for the Cr(VI)-based coating, which corresponded to the main peak of the CrO_3 powder standard.

The C K edge spectra (*Figure 40* (b)) was measured with the aim of exploring the presence of the Cr carbides present in the Cr(III)-based coatings [219,220]; however, most of the signals were found to be masked by the C adventitious contamination layer since the spectra of the Cr coatings matched perfectly to the spectra of a silicon standard wafer [158,159]. The surfaces were etched using a coupled Ar ion gun (similarly to AES and XPS) to try to get rid of the contamination layer and to measure the Cr layer underneath. New peaks were promoted/revealed at 288.8 eV after the sputtering, which could be attributed to chromium carbides (according to the $Cr_{23}C_6$ and Cr_3C_2 powder standards, measurements not shown here); however, this peak was also observed in the Cr(VI)-based coating (which indeed does not contain carbides according to XPS, *Figure 36* (b), *intermediate etched*), indicating that they were formed by the Ar ion sputtering (as previously observed in *Figure 36* (b), etched surface).

The TEY O K edge spectra (*Figure 40* (c)), are showing similar shape for both Cr coatings analogously to the Cr L edge, with slight and not significant shifts in their peaks. The main peak located at approximately 532.7 eV and the broad signal observed in the 537.7 - 543.6 eV range are believed to correspond Cr_2O_3, as they matched with the spectra of the standard Cr_2O_3 powder [221]. However, an additional small peak was observed for Cr(VI)-based coating at approximately 529.2 eV which was attributed to the presence of CrO_3 as it corresponded to its main peak, in agreement with the same finding on the Cr L edge. Such CrO_3 oxide disappeared in the TFY spectra (larger analysis depth, *Figure 40* (d)). Both findings (the peak at 529.2 eV in TEY and its absence in TFY), confirms the presence of a thin CrO_3 layer on top of the Cr_2O_3 oxide one for the Cr(VI)-based coatings.

4.3.2.2 Thickness

The *Table 25* shows the thickness values of the native oxide layer formed on top of the two Cr coatings systems, which were measured using XPS superficial measurements and the Carlson equation (*Equation 2*).

***Table 25**. Native oxide layer thickness estimated by XPS (Carlson equation) for the Cr(VI) and Cr(III)-based coatings.*

Sample	Native oxide layer thickness (nm)
Cr(VI)	2.3 (-)
Cr(III) chloride	1.0 (0.1)

The native oxide film formed on the Cr(VI)-based coating was found to be 2 times thicker than the one formed on the Cr(III) system. This result is in agreement with the higher relative Cr_2O_3 signals observed in the Cr L edge (*Figure 40* (c)) of the synchrotron-based XAS measurements and also with the higher Cr oxy/hydroxide concentrations (Cr-O component) by XPS (*Table 24*).

4.3.3 Semiconducting properties of the oxide layer

4.3.3.1 Mott-Schottky

Initially, the anodic branch was obtained by PDP measurements in borate buffer electrolyte (pH 8.4) to determine the passive region.
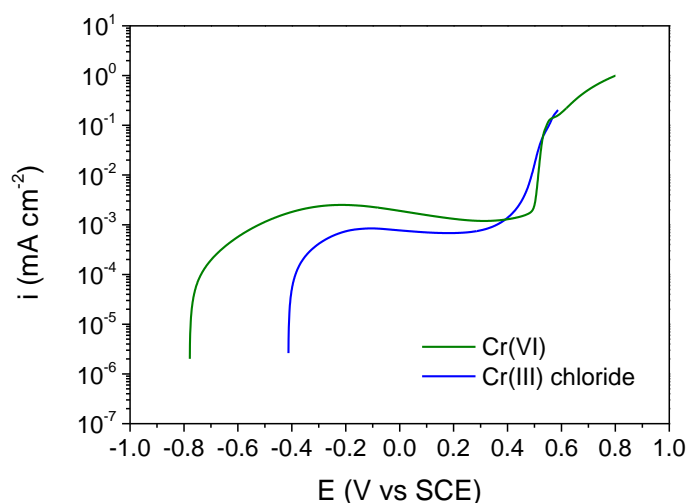
***Figure 41.** Polarisation curve of the Cr(VI) and Cr(III)-based Cr coatings in borate buffer electrolyte (pH 8.4).*

The corrosion potential of the Cr(VI)-based coating was found to be much more negative than the chloride-based Cr(III) one (- 0.8 V and - 0.4 V, respectively) whilst the breakdown potential was slightly more positive (0.4 V vs. 0.5 V, for Cr(VI) and Cr(III) systems respectively). The passive region of the Cr(VI)-based system was broader and its i_{pass} was found to be approximately ½ order of magnitude higher than the Cr(III) one, at potentials below 0.2 V; initially, the higher i_{pass} will denote a less stable passive film. The *Figure 42* shows the Mott-Schottky plots for the Cr(VI) and Cr(III)-based electrodeposits.
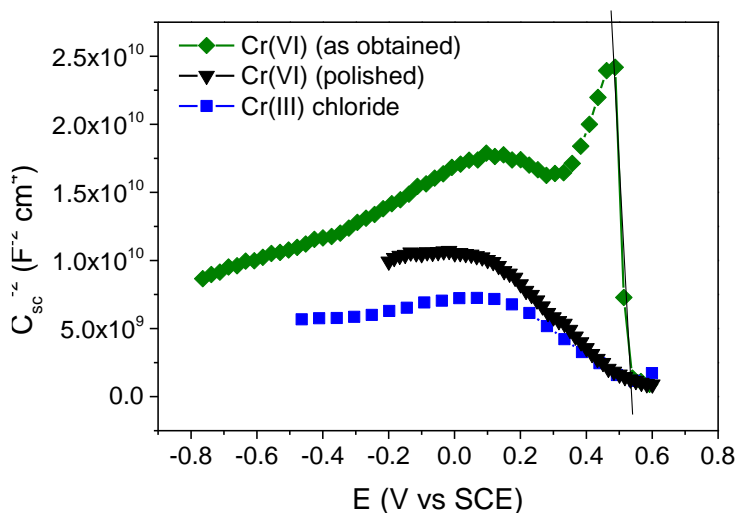
Figure 42. *Mott-Schottky plot of the as obtained surface of Cr(III) and Cr(VI)-based Cr coatings in borate buffer (pH 8.4), together with the corresponding measurement after polishing the Cr(VI) system.*

Although a similar Mott-Schottky plot was expected for the Cr(VI)-based and the Cr standard (similar chemical composition without C), the shape of the Mott-Schottky plot was found to be completely different (*Figure 42* and *Figure 22*). The main differences that could explain this are mainly, but not exclusively the followings: (i) differences in the non-stoichiometry of the oxides present in the native oxide layer, since their semiconducting properties could depend on that [222], (ii) presence of the thin CrO_3 layer that was found by synchrotron-based XAS measurements on the top of the surface of the native oxide layer formed on Cr(VI)-based coatings, (iii) the fact that the Cr standard is polished after each experiment, which could be having an impact on the semiconducting properties of its oxide. Taking into account that some authors observed that the properties of the formed passive films were sensible to different mechanical treatments of the surface [223], the Cr(VI)-based sample was gently polished in order to remove CrO_3 thin layer present in the native oxide layer and to find out if this CrO_3 was formed in the electroplating bath or if it was inherent to the system. This was addressed by measuring the semiconducting properties, using Mott-Schottky, of the spontaneously formed fresh air-oxide film. At first glance, a change in the shape Mott-Schottky plot was observed (*Figure 42*, black line) being more similar to the Cr standard and to the Cr(III)-based systems (*Figure 22* and *Figure 42*). This confirms that: (i) most probably, the CrO_3 is having an impact on the semiconducting properties of the native oxide layer, (ii) the native oxide layer of Cr(VI) systems cannot be straightforwardly compared to the one of Cr standard and only the polished ones can be easily compared.

The electronic properties were calculated from the previous Mott-Schottky plot (*Figure 42*) and gathered in the *Table 26* in order to support the discussion on the semiconducting properties. Despite the multiple linear regions observed in the Cr(VI)-based sample, the fitting was carried out in the last slope, located between 0.4 and 0.6 V, because a similar E_{fb} (chemical nature of the oxide) was obtained in comparison to the Cr(III) system (further discussed below), whilst very different E_{fb} values were obtained for the previous slopes (- 1.1, 0.05 and 1.5 V respectively for the slopes present in the following potential ranges:- 0.3 to 0, 0.15 to 0.25 and 0.35 to 0.45). Moreover, when increasing the frequency of the Mott-Schottky plot such slopes disappeared, showing a trend with only one linear region (corresponding to the last slope of the *Figure 42*, in the 0.4 - 0.6 V range, which was fitted for the data analysis) with the same E_{fb} to the one obtained in the table below.

Table 26. *Electronic properties calculated from the Mott-Schottky plot for the Cr(VI) and Cr(III)-based coatings, as obtained and after polishing the Cr(VI) sample.*

Sample	E_{corr} *(V vs SCE)*	N_A *($x10^{20}$ cm^{-3})*	E_{fb} *(V vs SCE)*	*Semiconductor type*
Cr(VI)	- 0.72 (0.08)	0.32 (0.08)	0.51 (0.00)	
Cr(VI) (polished)	- 0.21 (-)	5.13 (-)	0.53 (-)	p
Cr(III) chloride	- 0.42 (0.04)	6.9 (0.2)	0.56 (0.01)	

Regarding the native oxide layers of Cr(III) and Cr(VI) systems, it can be observed that Cr(VI)-based systems possess a one order-of-magnitude less defective oxide film (0.32 and $6.9x10^{20}$ cm^{-3} N_A for Cr(VI) and Cr(III) systems, respectively). It would decrease the reactivity of the surface, hindering as a result the electronic mobility and the electrochemical reactions taking place at the oxide/electrolyte interphase [118,119]. Some differences are also observed when analysing the E_{fb} of the oxide layers of both systems: the native oxide layer formed on the Cr(VI)-based system has a lower E_{fb} (0.51 V) in comparison to the native oxide layer formed on the Cr(III) system (0.56 V). This may indicate some subtle differences in the chemical nature of their oxide layers.

When the surface of the Cr(VI)-based coating is polished, the charge carriers density are decreased by one order of magnitude (from 0.32 to $5.13x10^{20}$ cm^{-3}), having a similar N_A value (but still smaller) to the Cr(III)-based sample and to the Cr standard (Table 14 and *Table 20*). The E_{fb} potential is slightly increased after the polishing (from 0.51 to 0.53 V) whilst the E_{corr} is significantly shifted towards more positive values (from - 0.72 to - 0.21 V) reaching a similar value compared to the Cr(III) system (- 0.42 V). This supports the hypothesis of the CrO_3 layer providing the enhanced semiconducting properties; this layer is believed to be formed during the native oxide layer formation in the electroplating bath

due to the extremely acid and high sulphuric acid concentration and, when it is removed after the polishing, a common Cr_2O_3 is believed to be formed by the exposure to the atmosphere, similarly to the Cr(III)-based in terms of semiconducting properties.

4.3.3.2 Point Defect Model

The PDM measurements results are shown in the *Figure 43*. A negative exponential function was obtained for both cases, which was fitted according to the *Equation 7* (experimental fit shown in the figure) to obtain the diffusion coefficient (*Table 27*).
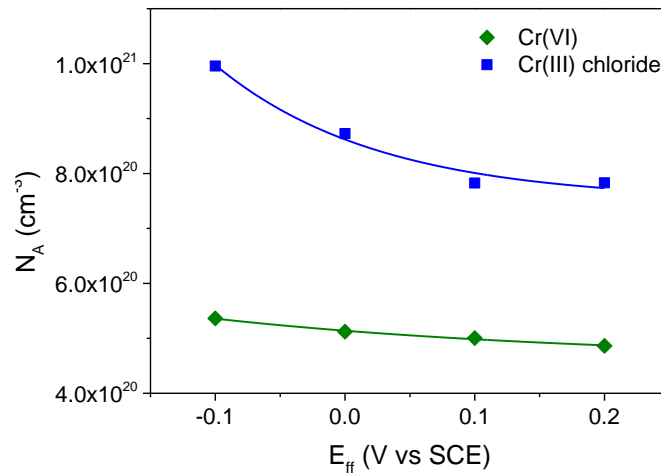
Figure 43. *Charge carrier density evolution of the Cr(VI) and Cr(III)-based coatings as a function of the film formation potential.*

The preliminary electrochemical protocol used to remove the native oxide layer, prior to the formation of passive films (described in the experimental section, *Table 8*) was believed to be enough to remove the topmost CrO_3 layer since the Mott-Schottky plot of the obtained passive films in the PDM experiment changed the shape in a similar way to the observed in the Mott-Schottky experiments after polishing the surface (*Figure 42*). So, the CrO_3 layer is assumed no to be playing a role in such passive films formed on the Cr(VI) system.

Table 27. *Results of the Point Defect Model data fitting for the Cr(VI) and Cr(III)-based coatings.*

| Parameter	Cr(VI)	Cr(III) chloride
w_1 *(cm^{-3})*	5.4×10^{19}	1.1×10^{20}
b *(V^{-1})*	3.4	8.0
w_2 *(cm^{-3})*	4.6×10^{20}	7.5×10^{20}
$K_e = \varepsilon_L$ *(V cm^{-1})*	1×10^6	
i_{ss} *(A cm^{-2})*	1.1×10^{-8}	3.1×10^{-8}
D_0 *(cm^2 s^{-1})*	9.4×10^{-19}	1.6×10^{-18}

Slightly lower i_{ss} and D_0 values were obtained for Cr(VI)-based system. This is in agreement with the previous Mott-Schottky results for the native oxide layer formed on Cr(VI) system. Typically, a high ion mobility will lead to a higher tendency for aggressive ions to penetrate and move through the oxide layer, reaching the metal surface and initiation pitting corrosion events, which eventually will cause the passive film breakdown with the consequent loss of protection; in contrast a low current and ion mobility will provide the passive layer a more protective ability [175]. Therefore, the lower point defects (Mott-Schottky results) and the lower mobility and diffusion coefficient (PDM results) obtained for the oxide layer formed on the Cr(VI) system are typical of a protective oxide film.

On the other hand, the D_0 from PDM is less than ½ order of magnitude lower (*Table 27*) for Cr(VI) in comparison to the Cr(III) system. This could be due to the fact that, as previously mentioned in the chapter 4.1, in the Mott-Schottky measurements the native oxide layer is measured (observable positive effect of the topmost CrO_3 layer), whilst in the PDM passive films are studied after removing the native oxide layer, and probably after removing the CrO_3 layer (further discussed in the Annex B). In this case, the slight differences observed in the i_{ss} and D_0 between the Cr(VI) and Cr(III)-based systems could be due to the different C amount and crystalline structure of both electroplated Cr layers.

4.3.4 Corrosion resistance evaluation of the Cr coating and oxide film

4.3.4.1 Kinetics of the oxide layer formation

Current-time transients (*Figure 44*) were measured to investigate the oxide layer formation kinetics in order to explore the protection capabilities of the different oxide layers. The *Table 28* shows the different parameters obtained after the linear fitting of such curves within the range 20 - 60 ms (*Figure 44*). Information of the oxide formation kinetic through the passivation index *n* (slope of the fitting) and from the current values of the beginning of the passivation (i_0) were obtained.
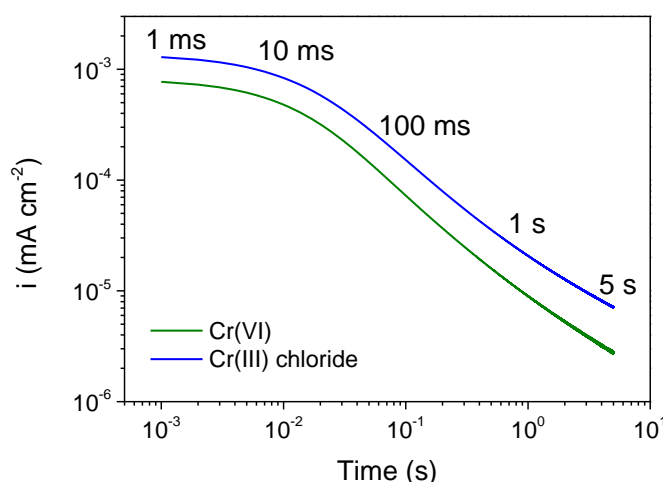
Figure 44. *Passivation kinetics or current-time transients measurements of the oxide layer formed on Cr(VI) and Cr(III)-based coatings.*

Table 28*. Obtained parameters from the linear fitting of the passivation kinetics measurements carried out on the Cr(VI) and Cr(III)-based coatings.*

Sample	n	i_0 (mA cm^{-2})
Cr(VI)	0.87 (0.08)	0.8 (0.1)
Cr(III) chloride	0.78 (0.01)	1.4 (0.1)

The oxide layer formed on the Cr(VI) system presents a significantly lower passivation current (0.8 mA cm^{-2}) in comparison to Cr(III) system (1.4 mA/cm^{-2}). In addition, a higher oxide formation kinetic was obtained for the Cr(VI)-based electrodeposit (0.87 vs. 0.78, *Table 28*). These features are typical of compact and protective passive films that are formed very quickly, hindering the absorption and penetration of aggressive ions. Better protective abilities are expected from the oxide formed on the Cr(VI)-based Cr electrodeposits compared to the Cr(III) system, since due to the observed higher oxide layer formation kinetics and lower passivation current. These enhanced properties are in agreement with the Mott-Schottky and PDM measurements where the native and formed oxide layer were found to be less defective and to present less diffusibility.

4.3.4.2 Corrosion resistance evaluation. Borate buffer vs NaCl electrolyte

PDP measurements were run to study the anodic branches of both systems (*Figure 45*). According to the findings observed in the previous chapters (4.1 and 4.2), two electrolytes were used in these measurements in order to explore the corrosion performance of the coatings (i) in a non-aggressive medium where the semiconducting properties were already studied (borate buffer electrolyte, pH 8.4) and (ii) in a more aggressive medium (0.1 M

NaCl). For the sake of reproducibility, samples were tested immediately after they were produced ("*as obtained*").
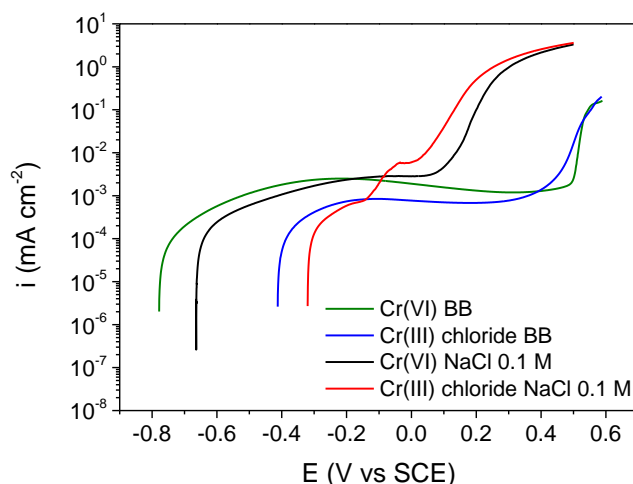
Figure 45. *Potentiodynamic polarisation curve of Cr(VI) and Cr(III)-based Cr coatings in both borate buffer and 0.1 M NaCl.*

The *Figure 45* shows the anodic branches of the PDP curves of the Cr(VI) and Cr(III)-based Cr coatings in both electrolytes. The impact of the 0.1 M NaCl electrolyte was similar for both Cr electrodeposits, in terms of potential values: a shift of the E_{corr} was observed to approximately + 100 mV, as well as a considerably lower E_{pit} (approx. - 400 mV) in comparison to the breakdown potential obtained in the PDP carried out in the borate buffer electrolyte. The Cr(VI)-based system presents a lower E_{corr} but a slightly higher E_{pit} in 0.1 M NaCl when compared to the Cr(III) system: the E_{corr} and E_{pit} values of the Cr(VI)-based coating are - 0.66 and + 0.10 V, respectively, whilst the Cr(III)-based system has - 0.32 and 0.05 V, respectively. Additionally, as the main difference between both coatings, the passive region is reduced by approximately 500 mV for the Cr(VI)-based whilst the Cr(III)-based Cr coating does not present a passive region, despite an small pseudo-passive region located in the - 0.04 and 0 V range. Regarding the impact of 0.1 M NaCl on the i_{pass}, was found to be different for each system when comparing to the borate buffer electrolyte: the Cr (VI)-based one did not undergo any significant variation (~ 10^{-3} mA cm^{-2} at 0.0 V) whilst the Cr(III)-based system abruptly increased its i_{pass} from 6×10^{-4} mA cm^{-2} to 6×10^{-3} mA cm^{-2} at 0.0 V.

Prior to the pseudo-passive region of the Cr(III)-based system, an small increase of the anodic current is observed at approximately - 0.1 V, related to the oxidation of Cr(III) to Cr(VI) [180,181] as explained in the chapter 4.1; curiously, this current increase was not observed for the Cr(VI)-based coating.

Summarising, although the corrosion capabilities have been diminished for both systems when studied in 0.1 M NaCl, the Cr(III)-based one exhibits an increased i_{pass} (one order of magnitude) and is showing a pseudo-passive region instead of the wide and well-defined passive region that the Cr(VI)-based systems presents. Initially and theoretically, all this will provide a less protective behaviour to the Cr(III)-based system.

Additionally, the polarisation resistance was calculated (*Table 29*) from LPR measurements.

Table 29. *Polarisation resistance values obtained from the LPR measurements for the Cr(VI) and Cr(III)-based Cr coatings in both borate buffer (pH 8.4) and 0.1 M NaCl electrolytes.*

Sample	R_P (x10^5 Ω cm^2)	
	Borate buffer (pH 8.4)	0.1 M NaCl
Cr(VI)	4.3 (0.6)	1.9 (0.1)
Cr(III) chloride	2.6 (0.6)	1.2 (0.1)

The R_p of the Cr(VI)-based electrodeposit was found to be almost 2 times higher in comparison to the Cr(III)-based systems in the borate buffer electrolyte (pH 8.4). This is in agreement with the semiconducting properties of the native oxide layer: one order-of-magnitude lower point defects (Mott-Schottky, *Table 26*) as well as a lower diffusion coefficient (*Table 27*) and a higher oxide layer formation kinetics (*Table 28*). These features are believed to be conferred by the presence of the thin topmost CrO_3 layer detected by synchrotron-based XAS (*Figure 40*), since in the literature the CrO_3 was observed to provide good anticorrosion to coatings [224], as well as its hydrated form H_2CrO_4.[225] If R_p values are compared in 0.1 M NaCl electrolyte, the values are decreased for both coatings due to the higher aggressiveness of the electrolyte but, even so, similar corrosion resistance was obtained: 1.9 and 1.2x10^5 Ω cm^2 respectively. Once again, the Cr(VI) system possess a slightly higher polarisation resistance value, showing still a better corrosion resistance performance.

4.3.5 Summary of the chapter

The most relevant observed findings are mentioned below:

1. Cr(VI)-based Cr coatings are constituted by pure Cr layers in comparison to Cr-C layers of the Cr(III)-based ones.

2. The presence of a topmost very thin CrO_3 layer was found on the surface by synchrotron-based XAS, whilst XPS was not sensitive enough to detect it.

3. The native oxide layer formed on Cr(VI)-based Cr electrodeposits shows an enhanced semiconducting properties and oxide formation kinetics.
    - Lower point defects (1 order of magnitude lower N_A).
    - Higher oxide formation kinetics and lower passivation current.

    However, when removing the native oxide layer by polishing the surface, the new air-formed oxide layer presents higher defects, having closer values to the oxide formed on the Cr(III)-based Cr coating.

4. The Cr(VI)-based coating presented a higher corrosion resistance (higher R_p) in both borate buffer (pH 8.4) and 0.1 M NaCl.

CHAPTER 5. GENERAL CONCLUSIONS

This Ph.D. intended to provide new insights about the passive layer of nanometric electroplated decorative Cr coatings. The different Cr coatings have been obtained by electrodeposition using model Cr(III) and Cr(VI)-based electrolytes. The physicochemical properties of the Cr layers and their native oxide layers have been explored including the semiconducting behaviour of their passive films and corrosion resistance performance. Analogously, the effect of Fe addition on a sulphate-based Cr(III) electroplating bath has been investigated based on the same terms. Finally, a comparison between a Cr(III) and Cr(VI)-based Cr electrodeposit was carried out.

As a result, a correlation has been stablished between the properties of the Cr layer/oxide film (regardless the underneath substrate) and the semiconducting properties and corrosion resistance performance. The main conclusions are the following:

Cr(III) chloride vs sulphate-based Cr coatings

1. The sulphate-based Cr coating has shown lower C content and a more crystalline structure. Additionally, traces of S were found in the sulphate system, corresponding to superficial adsorbed sulphates ions and absorbed sulphate salts/thiourea (S=C). The semiconducting properties of the native oxide layer were showing higher point defects. Despite having a more Cr-oxide rich and thicker native oxide layer, the sulphate-based system presented a lower corrosion resistance performance in borate buffer electrolyte (pH 8.4). Thus, a direct correlation between the semiconducting properties and the corrosion resistance was found.

2. Increasing the aggressiveness of the electrolyte (0.1 M NaCl) provokes a much lower corrosion resistance compared to borate buffer electrolyte. However, although a similar behaviour was obtained for both Cr(III)-based systems, aged sulphate-based coating has shown a better performance.

As a summary, the traces of adsorbed S on the sulphate-based Cr electrodeposits are believed to be responsible of the more defective and less protective oxide film formation. Among all the measured parameters (chemical composition, thickness, structure, etc.) the semiconducting properties and specifically, the concentration of point defects measured by Mott-Schottky seems to be ruling the corrosion performance.

Additionally, such defective oxide layer (sulphate system) evolved with the time and showed a better performance in aggressive mediums such as NaCl-based electrolytes after 1-year aging.

Effect of Fe addition on the Cr(III) sulphate-based bath

3. The addition of Fe to the Cr(III) sulphate-based electroplating implies the formation of a Cr-Fe alloy but with a different impact on the naturally formed oxide layer:

    (i)   adding 8 mg/L Fe did not affect to the native oxide layer (a single Cr_2O_3 oxide layer showing a p-type semiconductor behaviour) and to the corrosion resistance (similar to the Fe0 sample).

    (ii) if the Fe concentration in the bath is 100 mg/L or higher (400 mg/L), a duplex oxide film was formed, containing an outer Fe-rich and an inner Cr-rich oxide/hydroxide layer. A more defective native oxide layer (p-n type semiconductor behaviour) having higher passivation current values during the kinetics formation. It was in agreement with the lower polarisation resistance (one order of magnitude lower if systems are compared in 0.1 M NaCl electrolyte).

    As main conclusion, adding 100 - 400 mg/L Fe affected dramatically to the semiconducting properties and oxide layer formation, and as a result, to the corrosion resistance properties of the coatings. In contrast, it was possible to decrease de deposition rate adding 8 mg/L Fe to the sulphate-based Cr(III) electroplating bath without diminishing the corrosion performance .

Cr(III) vs Cr(VI)-based Cr coatings

4. In contrast to Cr(III)-based system, the Cr(VI)-based ones provides amorphous and pure Cr coatings.

5. The native oxide layer formed on the Cr(VI)-based is formed by a single layer of Cr_2O_3 (p-type behaviour) which also has a thin CrO_3 oxide on the top according to synchrotron-based measurements, probably due to the extremely acidic working conditions of the electroplating bath of the Cr(VI) system. The semiconducting properties in comparison to the Cr(III)-based samples are much better (N_A are one order of magnitude less defective, having a lower ion diffusion coefficient, faster oxide layer formation kinetic and lower passivation current values). Consequently, a more protective native oxide layer was formed, presenting a higher corrosion resistance performance in both borate buffer and 0.1 M NaCl electrolytes.

In few words, the enhanced corrosion resistance of Cr(VI)-based coatings in comparison to the Cr(III) ones was found to be caused by the presence of a topmost thin CrO_3 layer. This layer provided less defective oxide layer with a very high oxide formation kinetics, which resulted in a very protective oxide film.

CHAPTER 6. FUTURE PERSPECTIVES

New insights have been provided on decorative Cr coatings based on Cr(III) electroplating baths, in terms of physicochemical properties of the electroplated Cr layers and their native oxide layer, and their impact in the corrosion resistance performance. Interestingly, the results have brought the following open question and issues to address:

-   To explore in detail the electroplated Cr layers. It has been found that both Cr(III)-based electroplated Cr layers are constituted by chromium carbide coatings but there were not observable by XRD or even by synchrotron-based XAS. Therefore, additional techniques/strategies are required to determine such carbides (e.g., $Cr_{23}C_6$, Cr_3C_2, etc.). The following strategy could be followed: (i) chemical treatments and attacks of cross-section samples, (ii) heat treatment and annealing processes to promote the crystallisation and further observation in XRD, (iii) using more sophisticated equipment such as TEM coupled with Selected Area Electron Diffraction (SAED) for their observation and characterisation.

-   To transfer the knowledge generated in this Ph.D. to the industry and to validate the findings creating new protection systems:

    (i)   using the Ni-Cr multilayer configuration of real commercial coatings.

    (ii) studying different electroplating bath formulations by modifying their organic additives (e.g., phosphorus-based ligands) in order to tune the corrosion resistance performance.

-   To further decrease the deposition rate of Cr(III)-based baths varying the Fe concentration between 8 and 100 mg/L, or even changing the doping agent but assuring that the p-type semiconducting behaviour is maintained.

-   Finally, taking into account the direct impact of the semiconducting properties of the native oxide layer on the corrosion performance, the surfaces of the Cr coatings could be further post-treated to improve such properties, for example, promoting the indirect formation of CrO_3 using new Cr(VI)-free alternatives or modifying the bath and working conditions to tune the semiconducting properties of the oxide film.

CHAPTER 7. REFERENCES

[1]   N. V. Mandich, D.L. Snyder, Electrodeposition of Chromium, in: Mod. Electroplat., Wiley, 2011: pp. 205–248. https://doi.org/10.1002/9780470602638.ch7.

[2]   R.P. Renz, J.J. Fortman, E.J. Taylor, M.E. Inman, A Functional Trivalent Chromium Process to Replace Hexavalent Chromium Plating, in: AESF/EPA Conf. Environ. Process Excell., 2003: pp. 196–207.

[3]   U.P. Kumar, C.J. Kennady, Characterization of Chromium Electrodeposits Obtained From Trivalent Electrolytes Containing Formaldehyde as Additive, Int. J. Thin Film Sci. Technol. 4 (2015) 147–153.

[4]   Y.B. Song, D.T. Chin, Current efficiency and polarization behavior of trivalent chromium electrodeposition process, Electrochim. Acta. 48 (2002) 349–356. https://doi.org/10.1016/S0013-4686(02)00678-3.

[5]   V.S. Protsenko, V.O. Gordiienko, F.I. Danilov, S.C. Kwon, M. Kim, J.Y. Lee, Unusually high current efficiency of nanocrystalline Cr electrodeposition process from trivalent chromium bath, Surf. Eng. 27 (2011) 690–692. https://doi.org/10.1179/1743294410Y.0000000019.

[6]   J. Li, Y. Li, X. Tian, L. Zou, X. Zhao, S. Wang, S. Wang, The Hardness and Corrosion Properties of Trivalent Chromium Hard Chromium, Mater. Sci. Appl. 8 (2017) 1014–1026. https://doi.org/10.4236/msa.2017.813074.

[7]   Y.B. Song, D.T. Chin, Pulse plating of hard chromium from trivalent baths, Plat. Surf. Finish. 87 (2000) 80–87.

[8]   L. Fedrizzi, S. Rossi, F. Bellei, F. Deflorian, Wear-corrosion mechanism of hard chromium coatings, Wear. 253 (2002) 1173–1181. https://doi.org/10.1016/S0043-1648(02)00254-5.

[9]   D.L. Snyder, Decorative chromium plating, Met. Finish. 93 (1995) 205–212. https://doi.org/10.1016/s0026-0576(00)80328-1.

[10]   P. Lansdell, J.P.G. Farr, The corrosion resistance of chromium electroplated from trivalent and hexavalent chromium plating solutions, Trans. Inst. Met. Finish. 75 (1997) 219–223. https://doi.org/10.1080/00202967.1997.11871178.

[11]   H. Brown, T.W. Tomaszewski, Electrodeposition of a micro-cracked corrosion resistant nickel-chromium plate, U.S. Patent No. 3,471,271, 1969. https://doi.org/10.1145/178951.178972.

[12]   A. Prinz, H. Viecenz, Nickel system, U.S. Patent No. US 2012/0164479 A1, 2012.

[13]   A. Königshofen, R. Kiefer, Multicorrosion Protection System for Decorative Parts With Chrome Finish, European Patent No. EP 3 147 389 B1, 2019.

[14]   J. Hao, L. Qian, Nickel and/or Chromium plated member and method for manufacturing the same, European Patent No. EP 3 067 443 A1, 2016.

[15]   S. Sugawara, H. Sakai, P. Hartmann, Chrome-plated part and manufacturing method of the same, U.S. patent No. US 2012/0052319 A1, 2012.

[16]   L. Ganborena, Novel insights into the corrosion mechanism of decorative multilayer nickel-chromium coatings on ABS: towards a correlation between CASS and electrochemical tests, Ph.D. thesis, Universidad del País Vasco/Euskal Herriko Unibertsitatea, 2020.

[17]   L. Ganborena, J.M. Vega, B. Özkaya, H.J. Grande, E. García-Lecina, AN SKP and EIS study of microporous nickel-chromium coatings in copper containing

electrolytes, Electrochim. Acta. 318 (2019) 683–694. https://doi.org/10.1016/j.electacta.2019.05.108.

[18] Directive 2000/53/EC of the European Parliament and of the Council of 18 September 2000 on end-of life vehicles - Commission Statements, OJ L 269, 21.10.2000, p. 34–43, 2000.

[19] B. Sonntag, V. Sundaram, Substitution of Cr (VI)-containing chromate coatings by the European automobile industry, 2006.

[20] Lanxess Deutschland GmbH, Functional chrome plating with decorative character. Analysis of Alternatives for Chromium trioxide, 2016.

[21] D. Smart, T.E. Such, S.J. Wake, A Novel Trivalent Chromium Electroplating Bath., Trans. Inst. Met. Finish. 61 (1983) 105–110. https://doi.org/10.1080/00202967.1983.11870647.

[22] L. Frazer, Shiny Science: A new substitute for hexavalent chromium, Environ. Health Perspect. 114 (2006) A482–A485. https://doi.org/10.1289/ehp.114-a482.

[23] Kiesow Dr. Brinkmann, Chromium(III) – a genuine alternative to chromium (VI)?, JOT J. Für Oberflächentechnik. (2014) 1–3.

[24] Z. Zeng, A. Liang, J. Zhang, A Review of Recent Patents on Trivalent Chromium Plating, Recent Patents Mater. Sci. 2 (2009) 50–57. https://doi.org/10.2174/1874464810902010050.

[25] S.L. Handy, C.F. Oduoza, T. Pearson, Theoretical aspects of electrodeposition of decorative chromium from trivalent electrolytes and corrosion rate study of different nickel/chromium coatings, Trans. Inst. Met. Finish. 84 (2006) 300–308. https://doi.org/10.1179/174591906X162946.

[26] S. Renton, J.C. Crowther, Chromium electroplating, U.S. Patent No. 4,093,521, 1978.

[27] C. Barnes, J.J.B.W. Ward, Electrodeposition of black chromium, U.S. Patent No. 4,196,063, 1980.

[28] J. Sjöberg, Validation and development of an electrodeposition process to deposit a black chromium coating from a trivalent chromium electrolyte, Ph.D. thesis, Uppsala Universitet, 2016.

[29] K.-D. Schulz, P. Wachter, P. Hartmann, Electroplating bath and method for producing dark chromium layers, International Patent No. WO 2012/150198 A2, 2012.

[30] Y.F. Jiang, F.Z. Yang, Z.Q. Tian, S.M. Zhou, Effects of iron ion contents on composition, morphology, structure and properties of chromium coatings electrodeposited from novel trivalent chromium sulphate electrolyte, Trans. Inst. Met. Finish. 90 (2012) 86–90. https://doi.org/10.1179/174591911X13225583568581.

[31] V.S. Protsenko, Electrodeposition from trivalent chromium baths as an environmentally friendly alternative to electroplating from hazardous hexavalent chromium baths, ChemXpress. 4 (2014) 246–252. https://doi.org/10.1007/s10098-014-0711-1.

[32] D. Dal Zilio, G. Schiavon, Electroplating bath containing trivalent chromium and process for depositing chromium, European patent No. EP 2 899 299 A1, (2015).

[33]   C.. Fink, Process of electrodepositing chromium and of preparing baths therefor, U.S. Patent No. 1,581,188, 1926.

[34]   A. Yli-Pentti, Electroplating and Electroless Plating, in: Compr. Mater. Process., Elsevier, 2014: pp. 277–306. https://doi.org/10.1016/B978-0-08-096532-1.00413-1.

[35]   J.P. Hoare, On the Mechanisms of Chromium Electrodeposition, J. Electrochem. Soc. 126 (1979) 190–199. https://doi.org/10.1149/1.2129004.

[36]   V.S. Protsenko, V.O. Gordiienko, F.I. Danilov, Unusual "chemical" mechanism of carbon co-deposition in Cr-C alloy electrodeposition process from trivalent chromium bath, Electrochem. Commun. 17 (2012) 85–87. https://doi.org/10.1016/j.elecom.2012.02.013.

[37]   Z. Zeng, Y. Sun, J. Zhang, The electrochemical reduction mechanism of trivalent chromium in the presence of formic acid, Electrochem. Commun. 11 (2009) 331–334. https://doi.org/10.1016/j.elecom.2008.11.055.

[38]   Z. Zeng, Y. Zhang, W. Zhao, J. Zhang, Role of complexing ligands in trivalent chromium electrodeposition, Surf. Coatings Technol. 205 (2011) 4771–4775. https://doi.org/10.1016/j.surfcoat.2011.04.019.

[39]   H.H. Sheu, C.H. Lin, S.Y. Jian, H. Bin Lee, B.R. Yang, M. Der Ger, Effects of complexing agents and current density on carbon content of trivalent chromium carbon coating and its properties, Int. J. Electrochem. Sci. 11 (2016) 7099–7110. https://doi.org/10.20964/2016.08.60.

[40]   O.J. Suarez, J.J. Olaya, M.F. Suarez, S.E. Rodil, Corrosion resistance of decorative chromium films obtained from trivalent chromium solutions, J. Chil. Chem. Soc. 57 (2012) 977–982. https://doi.org/10.4067/S0717-97072012000100005.

[41]   R.A. Tremmel, Methods to improve the corrosion performance of microporous nickel deposits, Plat. Surf. Finish. (1996) 24–27.

[42]   G. Saravanan, S. Mohan, Corrosion behavior of Cr electrodeposited from Cr(VI) and Cr(III)-baths using direct (DCD) and pulse electrodeposition (PED) techniques, Corros. Sci. 51 (2009) 197–202. https://doi.org/10.1016/j.corsci.2008.10.005.

[43]   C.W. Liao, K.H. Hou, H.C. Wang, C.E. Lu, M. Der Ger, Corrosion and wear resistance of electroplating trivalent chromium-carbon coating, Key Eng. Mater. 642 (2015) 45–49. https://doi.org/10.4028/www.scientific.net/KEM.642.45.

[44]   Z. Zeng, A. Liang, J. Zhang, Electrochemical corrosion behavior of chromium-phosphorus coatings electrodeposited from trivalent chromium baths, Electrochim. Acta. 53 (2008) 7344–7349. https://doi.org/10.1016/j.electacta.2008.03.081.

[45]   H.H. Sheu, J.H. Syu, Y.M. Liu, K.H. Hou, M. Der Ger, A comparison of the corrosion resistance and wear resistance behavior of Cr-C, Ni-P and Ni-B coatings electroplated on 4140 alloy steel, Int. J. Electrochem. Sci. 13 (2018) 3267–3278. https://doi.org/10.20964/2018.04.49.

[46]   C.E. Lu, J.L. Lee, H.H. Sheu, K.H. Hou, C.C. Tseng, M. Der Ger, Preparation and characterizations of high carbon content Cr-C coatings electroplated from a trivalent chromium-based bath, Int. J. Electrochem. Sci. 10 (2015) 5405–5419.

[47]   A.A. Edigaryan, V.A. Safonov, E.N. Lubnin, L.N. Vykhodtseva, G.E. Chusova, Y.M. Polukarov, Properties and preparation of amorphous chromium carbide electroplates, Electrochim. Acta. 47 (2002) 2775–2786. https://doi.org/10.1016/S0013-4686(02)00163-9.

[48]   Z. Zeng, L. Wang, A. Liang, L. Chen, J. Zhang, Fabrication of a nanocrystalline Cr-C layer with excellent anti-wear performance, Mater. Lett. 61 (2007) 4107–4109. https://doi.org/10.1016/j.matlet.2007.01.066.

[49]   S.C. Kwon, M. Kim, S.U. Park, D.Y. Kim, D. Kim, K.S. Nam, Y. Choi, Characterization of intermediate Cr-C layer fabricated by electrodeposition in hexavalent and trivalent chromium baths, Surf. Coatings Technol. 183 (2004) 151–156. https://doi.org/10.1016/j.surfcoat.2003.09.069.

[50]   D.B. Lee, Oxidation of Cr-C electroplating between 400 and 900°C in air, Mater. Corros. 59 (2008) 598–601. https://doi.org/10.1002/maco.200804143.

[51]   S. Ghaziof, M.A. Golozar, K. Raeissi, Characterization of as-deposited and annealed Cr-C alloy coatings produced from a trivalent chromium bath, J. Alloys Compd. 496 (2010) 164–168. https://doi.org/10.1016/j.jallcom.2010.02.101.

[52]   H.H. Sheu, T.Y. Hong, T. Te Lin, M. Der Ger, The effect of heat treatment on the corrosion resistance, mechanical properties and wear resistance of Cr-C Coatings and Cr-C/Al2O3 composite coatings electrodeposited on low carbon steel, Int. J. Electrochem. Sci. 13 (2018) 9399–9415. https://doi.org/10.20964/2018.10.39.

[53]   B. Li, A. Lin, F. Gan, Preparation and characterization of Cr-P coatings by electrodeposition from trivalent chromium electrolytes using malonic acid as complex, Surf. Coatings Technol. 201 (2006) 2578–2586. https://doi.org/10.1016/j.surfcoat.2006.05.001.

[54]   B. Li, A. Lin, X. Wu, Y. Zhang, F. Gan, Electrodeposition and characterization of Fe-Cr-P amorphous alloys from trivalent chromium sulfate electrolyte, J. Alloys Compd. 453 (2008) 93–101. https://doi.org/10.1016/j.jallcom.2006.11.162.

[55]   H. Yu, B. Chen, H. Wu, X. Sun, B. Li, Improved electrochemical performance of trivalent-chrome coating on Al 6063 alloy via urea and thiourea addition, Electrochim. Acta. 54 (2008) 720–726. https://doi.org/10.1016/j.electacta.2008.06.069.

[56]   S. Surviliene, V. Jasulaitiene, O. Nivinskiene, A. Češuniene, Effect of hydrazine and hydroxylaminophosphate on chrome plating from trivalent electrolytes, Appl. Surf. Sci. 253 (2007) 6738–6743. https://doi.org/10.1016/j.apsusc.2007.01.122.

[57]   S. Marcelin, B. Ter-Ovanessian, B. Normand, Electronic properties of passive films from the multi-frequency Mott-Schottky and power-law coupled approach, Electrochem. Commun. 66 (2016) 62–65. https://doi.org/10.1016/j.elecom.2016.03.003.

[58]   A. Fattah-alhosseini, M.M. Khalvan, Semiconducting properties of passive films formed on AISI 420 stainless steel in nitric acid solutions, J. Adv. Mater. Process. 1 (2013) 15–22.

[59]   N.E. Hakiki, M. Da Cunha Belo, A.M.P. Simões, M.G.S. Ferreira, Semiconducting properties of passive films formed on Stainless Steels: Influence of the alloying elements, J. Electrochem. Soc. 145 (1998) 3821–3829. https://doi.org/10.1149/1.1838880.

[60]   I.H. Toor, M. Ejaz, H.S. Kwon, Mott-Schottky analysis of passive films on Cu containing Fe-20Cr-xCu (x=0, 4) alloys, Corros. Eng. Sci. Technol. 49 (2014) 390–395. https://doi.org/10.1179/1743278214Y.0000000154.

[61]   R.A. Antunes, M.C. Lopes De Oliveira, J.A. Batista De Souza, Effect of temperature on corrosion and semiconducting properties of oxide films formed on M5 zirconium

alloy, Corros. Eng. Sci. Technol. 51 (2016) 104–109.
https://doi.org/10.1179/1743278215Y.0000000036.

[62] D.D. Macdonald, The Point Defect Model for the Passive State, J. Electrochem. Soc. 139 (1992) 3434–3449. https://doi.org/10.1149/1.2069096.

[63] U. Konig, About the influence of the electronic properties of passive layers on the corrosion rate, Mater. Sci. Forum. 192–194 (1995) 79–88.
https://doi.org/10.4028/www.scientific.net/msf.192-194.79.

[64] L. Hamadou, A. Kadri, N. Benbrahim, Characterisation of passive films formed on low carbon steel in borate buffer solution (pH 9.2) by electrochemical impedance spectroscopy, Appl. Surf. Sci. 252 (2005) 1510–1519.
https://doi.org/10.1016/j.apsusc.2005.02.135.

[65] M.C.L. de Oliveira, V.S.M. Pereira, O.V. Correa, N.B. de Lima, R.A. Antunes, Correlation between the corrosion resistance and the semiconducting properties of the oxide film formed on AZ91D alloy after solution treatment, Corros. Sci. 69 (2013) 311–321. https://doi.org/10.1016/j.corsci.2012.12.015.

[66] I.G. Ogunsanya, C.M. Hansson, The semiconductor properties of passive films and corrosion behavior of stainless steel reinforcing bars in simulated concrete pore solution, Materialia. 6 (2019). https://doi.org/10.1016/j.mtla.2019.100321.

[67] R.K. de Oliveira, O.V. Correa, M.C.L. de Oliveira, R.A. Antunes, Surface Chemistry and Semiconducting Properties of Passive Film and Corrosion Resistance of Annealed Surgical Stainless Steel, J. Mater. Eng. Perform. 29 (2020) 6085–6100.
https://doi.org/10.1007/s11665-020-05067-3.

[68] H. Tsuchiya, S. Fujimoto, O. Chihara, T. Shibata, Semiconductive behavior of passive films formed on pure Cr and Fe-Cr alloys in sulfuric acid solution, Electrochim. Acta. 47 (2002) 4357–4366. https://doi.org/10.1016/S0013-4686(02)00508-X.

[69] C. Boissy, B. Ter-Ovanessian, N. Mary, B. Normand, Correlation between predictive and descriptive models to characterize the passive film - Study of pure chromium by electrochemical impedance spectroscopy, Electrochim. Acta. 174 (2015) 430–437. https://doi.org/10.1016/j.electacta.2015.05.179.

[70] D.S. Kong, S.H. Chen, C. Wang, W.W. Yang, A study of the passive films on chromium by capacitance measurement, Corros. Sci. 45 (2003) 747–758.
https://doi.org/10.1016/S0010-938X(02)00148-8.

[71] Y. Ren, G. Zhou, Rediscovering Mott-Schottky Plots: A Knee-point in the Plot for Passive Films on Chromium, J. Electrochem. Soc. 164 (2017) C182–C187.
https://doi.org/10.1149/2.1691704jes.

[72] L. Jinlong, L. Tongxiang, The effect of passivated potential on the passive films formed on pure chromium in borate buffer solution, Surf. Interface Anal. 49 (2016) 533–537. https://doi.org/10.1002/sia.6190.

[73] N.B. Hakiki, S. Boudin, B. Rondot, M. Da Cunha Belo, The electronic structure of passive films formed on stainless steels, Corros. Sci. 37 (1995) 1809–1822.
https://doi.org/10.1016/0010-938X(95)00084-W.

[74] C.O.A. Olsson, D. Landolt, Passive films on stainless steels - Chemistry, structure and growth, Electrochim. Acta. 48 (2003) 1093–1104.
https://doi.org/10.1016/S0013-4686(02)00841-1.

[75] K. Hashimoto, K. Asami, A. Kawashima, H. Habazaki, E. Akiyama, The role of corrosion-resistant alloying elements in passivity, Corros. Sci. 49 (2007) 42–52. https://doi.org/10.1016/j.corsci.2006.05.003.

[76] M.J. Graham, Recent advances in oxide film characterization, Pure Appl. Chem. 64 (1992) 1641–1645. https://doi.org/10.1351/pac199264111641.

[77] J.E. Maslar, W.S. Hurst, J.J. Bowers, J.H. Hendricks, In situ Raman spectroscopic investigation of stainless steel hydrothermal corrosion, Corrosion. 58 (2002) 739–747. https://doi.org/10.5006/1.3277656.

[78] P. Christensen, A. Hamnett, In-situ techniques in electrochemistry - ellipsometry and FTIR, Electrochim. Acta. 45 (2000) 2443–2459. https://doi.org/10.1016/S0013-4686(00)00332-7.

[79] N.H. Turner, B.I. Dunlap, R.J. Colton, Surface Analysis: X-ray Photoelectron Spectroscopy, Auger Electron Spectroscopy, and Secondary Ion Mass Spectrometry, Anal. Chem. 56 (1984) 373R-416R. https://doi.org/10.1021/ac00269a026.

[80] N.H. Turner, J.A. Schreifels, Surface analysis: X-ray photoelectron spectroscopy and Auger electron spectroscopy, Anal. Chem. 72 (2000) 99R-110R. https://doi.org/10.1021/a10000110.

[81] N.H. Turner, X-ray Photoelectron and Auger Electron Spectrocpy, Encycl. Anal. Chem. (2006) 1–34. https://doi.org/10.1002/9780470027318.

[82] J.F. Watts, J. Wolstenholme, An Introduction to Surface Analysis by XPS and AES, John Wiley & Sons, 2019. https://doi.org/10.1002/9781119417651.

[83] A. Hubin, H. Terryn, X-ray photoelectron and Auger electron spectroscopy, in: Non-Destructive Microanal. Cult. Herit. Mater., 2004: pp. 277–312.

[84] S. Tougaard, Surface analysis | X-ray Photoelectron Spectroscopy, in: Ref. Modul. Chem. Mol. Sicences Chem. Eng., Elsevier Inc., 2013. https://doi.org/10.1016/B978-0-12-409547-2.00527-8.

[85] B.R. Strohmeier, An ESCA method for determining the oxide thickness on aluminum alloys, Surf. Interface Anal. 15 (1990) 51–56. https://doi.org/10.1002/sia.740150109.

[86] S. Suzuki, T. Kosaka, H. Inoue, Y. Waseda, Angle resolved XPS study of thin oxide layers formed on the surface of iron-chromium binary alloys exposed to air, ISIJ Int. 36 (1996) 433–437. https://doi.org/10.2355/isijinternational.36.433.

[87] R.P. Gunawardane, C.R. Arumainayagam, Auger electron spectroscopy, in: Charact. Nanoparticles Meas. Process. Nanoparticles, Elsevier, 2019. https://doi.org/10.1016/B978-0-12-814182-3.00020-1.

[88] R.D. Holbrook, A.A. Galyean, J.M. Gorham, A. Herzing, J. Pettibone, Overview of Nanomaterial Characterization and Metrology, in: Charact. Nanomater. Complex Environ. Biol. Media, Elsevier, 2015: pp. 47–87. https://doi.org/10.1016/B978-0-08-099948-7.00002-6.

[89] V. Thiel, P. Sjövall, Using time-of-flight secondary ion mass spectrometry to study biomarkers, Annu. Rev. Earth Planet. Sci. 39 (2011) 126–156. https://doi.org/10.1146/annurev-earth-040610-133525.

[90] A. Benninghoven, Chemical Analysis of Inorganic and Organic Surfaces and Thin

Films by Static Time-of-Flight Secondary Ion Mass Spectrometry (TOF-SIMS), Angew. Chemie Int. Ed. 33 (1994) 1023–1043. https://doi.org/10.1002/anie.199410231.

[91]   D. Goebl, B. Bruckner, D. Roth, C. Ahamer, P. Bauer, Low-energy ion scattering: A quantitative method?, Nucl. Instruments Methods Phys. Res. Sect. B Beam Interact. with Mater. Atoms. 354 (2015) 3–8. https://doi.org/10.1016/j.nimb.2014.11.030.

[92]   C. Cushman, T. Grehl, M.R. Linford, Low Energy Ion Scattering (LEIS). I. The Fundamentals, Vac. Technol. Coat. (2015) 2–7.

[93]   H.H. Brongersma, T. Grehl, E.R. Schofield, R.A.P. Smith, H.R.J. Ter Veen, Analysis of the outer surface of platinum-gold catalysts by low-energy ion scattering, Platin. Met. Rev. 54 (2010) 81–87. https://doi.org/10.1595/147106710X494358.

[94]   C. V. Cushman, P. Brüner, J. Zakel, G.H. Major, B.M. Lunt, N.J. Smith, T. Grehl, M.R. Linford, Low energy ion scattering (LEIS). A practical introduction to its theory, instrumentation, and applications, Anal. Methods. 8 (2016) 3419–3439. https://doi.org/10.1039/c6ay00765a.

[95]   S. Hofmann, Practical surface analysis: state of the art and recent developments in AES, XPS, ISS and SIMS, Surf. Interface Anal. 9 (1986) 3–20. https://doi.org/10.1002/sia.740090104.

[96]   R. Escobar Galindo, R. Gago, A. Lousa, J.M. Albella, Comparative depth-profiling analysis of nanometer-metal multilayers by ion-probing techniques, Trends Anal. Chem. 28 (2009) 494–505. https://doi.org/10.1016/j.trac.2009.01.004.

[97]   D.R. Baer, M.H. Engelhard, A.S. Lea, P. Nachimuthu, T.C. Droubay, J. Kim, B. Lee, C. Mathews, R.L. Opila, L. V. Saraf, W.F. Stickle, R.M. Wallace, B.S. Wright, Comparison of the sputter rates of oxide films relative to the sputter rate of SiO2, J. Vac. Sci. Technol. A. 28 (2010) 1060–1072. https://doi.org/10.1116/1.3456123.

[98]   H. Fujiwara, Introduction to Spectroscopic Ellipsometry, in: Spectrosc. Ellipsom. Princ. Appl., 2007: pp. 1–11. https://doi.org/10.1002/9780470060193.ch1.

[99]   D. Gonçalves, E.A. Irene, Fundamentals and applications of spectroscopic ellipsometry, Quim. Nova. 25 (2002) 794–800. https://doi.org/10.1590/S0100-40422002000500015.

[100]   X. Zhou, G.E. Thompson, Electron and photon based spatially resolved techniques, in: Shreir's Corros., 2010: pp. 1405–1429. https://doi.org/10.1016/B978-044452787-5.00070-6.

[101]   G. Feng, L. Wu, J. Letey, Evaluating aeration criteria by simultaneous measurement of oxygen diffusion rate and soil-water regime, Soil Sci. 167 (2002) 495–503. https://doi.org/10.1097/00010694-200208000-00001.

[102]   A. Bharti, N. Goyal, Fundamentals of Synchrotron Radiations, in: Synchrotron Radiat. - Useful Interes. Appl., IntechOpen, 2019. https://doi.org/10.5772/intechopen.79284.

[103]   Scheme of sinchrotron light, (2021). https://intranet.cells.es/AboutUs/WhatIs (accessed September 19, 2021).

[104]   S. Pascarelli, Fundamentals of X-ray Absorption Fine Structure: basic principles, ESRF, (2016).

[105] H. Hulme, An X-ray absorption near- edge structure (XANES) study of the oxidation state of tin in zirconium alloy oxide films, Ph.D. thesis, University of Manchester, 2015.

[106] J.G. Parsons, M. V. Aldrich, J.L. Gardea-Torresdey, Environmental and biological applications of extended X-ray absorption fine structure (EXAFS) and X-ray absorption near edge structure (XANES) spectroscopies, Appl. Spectrosc. Rev. 37 (2002). https://doi.org/10.1081/ASR-120006044.

[107] J.E. Penner-Hahn, X-ray Absorption Spectroscopy, in: Compr. Coord. Chem. II, 2003: pp. 159–186. https://doi.org/10.1016/B0-08-043748-6/01063-X.

[108] S. Mobilio, F. Boscherini, C. Meneghini, Synchrotron radiation: Basics, methods and applications, Springer, New York, 2015. https://doi.org/10.1007/978-3-642-55315-8.

[109] J.I. Goldstein, D.E. Newbury, J.R. Michael, N.W.M. Ritchie, J.H.J. Scott, D.C. Joy, Scanning Electron Microscopy and X-Ray Microanalysis, Springer, New York, 2018.

[110] C.E. Lyman, J.I. Goldstein, A.D. Romig, P. Echlin, D.C. Joy, D.E. Newbury, D.B. Williams, J.T. Armstrong, C.E. Fiori, E. Lifshin, K.-R. Peters, Scanning Electron Microscopy, X-Ray Microanalysis, and Analytical Electron Microscopy, Plenum Press, New York, 1990.

[111] T. V. Vorburger, H.G. Rhee, T.B. Renegar, J.F. Song, A. Zheng, Comparison of optical and stylus methods for measurement of surface texture, Int. J. Adv. Manuf. Technol. 33 (2007) 110–118. https://doi.org/10.1007/s00170-007-0953-8.

[112] Y. Waseda, E. Matsubara, K. Shinoda, X-Ray Diffraction Crystallography, Springer, 2011. https://doi.org/10.1360/SSPMA2015-00359.

[113] H.-H. Ge, X.-M. Xu, L. Zhao, F. Song, J. Shen, G.-D. Zhou, Semiconducting behavior of passive film formed on stainless steel in borate buffer solution containing sulfide, J. Appl. Electrochem. 41 (2011) 519–525. https://doi.org/10.1007/s10800-011-0272-5.

[114] S.P. Harrington, T.M. Devine, Relation Between the Semiconducting Properties of a Passive Film and Reduction Reaction Rates, J. Electrochem. Soc. 156 (2009) C154–C159. https://doi.org/10.1149/1.3077576.

[115] A.A. Ogwu, A.M. Oje, J. Kavanagh, Corrosion, ion release and Mott-Schottky probe of chromium oxide coatings in saline solution with potential for orthopaedic implant applications, Mater. Res. Express. 3 (2016). https://doi.org/10.1088/2053-1591/3/4/045401.

[116] L. Jinlong, L. Hongyun, Comparison of corrosion properties of passive films formed on phase reversion induced nano/ultrafine-grained 321 stainless steel, Appl. Surf. Sci. 280 (2013) 124–131. https://doi.org/10.1016/j.apsusc.2013.04.108.

[117] I.-H. Toor, Mott-Schottky Analysis of Passive Films on Si Containing Stainless Steel Alloys, J. Electrochem. Soc. 158 (2011) C391–C395. https://doi.org/10.1149/2.083111jes.

[118] S. Ningshen, U. Kamachi Mudali, V.K. Mittal, H.S. Khatak, Semiconducting and passive film properties of nitrogen-containing type 316LN stainless steels, Corros. Sci. 49 (2007) 481–496. https://doi.org/10.1016/j.corsci.2006.05.041.

[119] Y. Xiao, J. Gu, J. Zhang, Semiconductor Property and Corrosion Behavior of

Passive Film Formed on Steel with Zinc Coating in 5% NaCl Solution, Arab. J. Sci. Eng. 42 (2017) 4273–4280. https://doi.org/10.1007/s13369-017-2640-x.

[120] A. Seyeux, V. Maurice, P. Marcus, Oxide Film Growth Kinetics on Metals and Alloys: I. Physical Model, J. Electrochem. Soc. 160 (2013) C189–C196. https://doi.org/10.1149/2.036306jes.

[121] D.D. MacDonald, The history of the Point Defect Model for the passive state: A brief review of film growth aspects, Electrochim. Acta. 56 (2011) 1761–1772. https://doi.org/10.1016/j.electacta.2010.11.005.

[122] H. Jang, S. Ahn, H. Kwon, Determination of the Diffusivity of Cation Vacancy in the Passive Film on Ni, ECS Trans. 3 (2019) 319–331. https://doi.org/10.1149/1.2789238.

[123] A. Fattah-alhosseini, Passivity of AISI 321 stainless steel in 0.5 M H2SO4 solution studied by Mott–Schottky analysis in conjunction with the point defect model, Arab. J. Chem. 9 (2016) S1342–S1348. https://doi.org/10.1016/j.arabjc.2012.02.015.

[124] A. Fattah-alhosseini, M.H. Alemi, S. Banaei, Diffusivity of Point Defects in the Passive Film on Stainless Steel, Int. J. Electrochem. (2011) 1–6. https://doi.org/10.4061/2011/968512.

[125] E. Sikora, J. Sikora, D.D. Macdonald, A new method for estimating the diffusivities of vacancies in passive films, Electrochim. Acta. 41 (1996) 783–789. https://doi.org/10.1016/0013-4686(95)00312-6.

[126] S.J. Ahn, H.S. Kwon, Effects of solution temperature on electronic properties of passive film formed on Fe in pH 8.5 borate buffer solution, Electrochim. Acta. 49 (2004) 3347–3353. https://doi.org/10.1016/j.electacta.2004.02.043.

[127] ASTM B117-19, Standard Practice for Operating Salt Spray (Fog) Apparatus, ASTM International, West Conshohocken, PA, www.astm.org, 2019.

[128] S. Dean, "Corrosion Testing of Materials with Metallic and Inorganic Coatings," in Testing of Metallic and Inorganic Coatings, ed. W. Harding and G.B. Di (West Conshohocken, PA: ASTM International), 177-192. https://doi.org/10.1520/STP20037S, 1987.

[129] ISO 9227:2017, Corrosion Tests in Artificial Atmospheres—Salt Spray Tests, International Standard Organization, 2017.

[130] ISO 10289:1999 Methods for corrosion testing of metallic and other inorganic coatings on metallic substrates — Rating of test specimens and manufactured articles subjected to corrosion tests, International Standard Organisation, 1999.

[131] Y.S. Jimenez, M.T. Gil, M.T. Guerra, L.S. Baltes, J.C.M. Rosca, Interpretation of Open Circuit Potential of Two Titanium Alloys For A Long Time Immersion In Physiological Fluid, Bull. Transilv. Univ. Brasov. Eng. Sci. Ser. I. 2 (2009) 197–204.

[132] K.B. Kabir, I. Mahmud, Study of Erosion-Corrosion of Stainless Steel, Brass and Aluminum by Open Circuit Potential Measurements, J. Chem. Eng. 25 (2011) 13–17. https://doi.org/10.3329/jce.v25i0.7234.

[133] F. Mansfeld, Tafel Slopes and Corrosion Rates from Polarization Resistance Measurements, Corrosion. 29 (1973) 397–402. https://doi.org/10.5006/0010-9312-29.10.397.

[134] W.J. Lorenz, F. Mansfeld, Determination of corrosion rates by electrochemical DC

and AC methods, Corros. Sci. 21 (1981) 647–672. https://doi.org/10.1016/0010-938X(81)90015-9.

[135] D. Landolt, Corrosion and surface chemistry of metals, EPFL Press, Lausanne (Switzerland), 2007. https://doi.org/10.5860/choice.45-0897.

[136] M. Stern, A.L. Geary, Electrochemical Polarization, 1. A Theoretical Analysis of the Shape of Polarization Curves, J. Electrochem. Soc. 104 (1957) 751–752. https://doi.org/10.1149/1.2428473.

[137] C. Nyby, X. Guo, J.E. Saal, S.C. Chien, A.Y. Gerard, H. Ke, T. Li, P. Lu, C. Oberdorfer, S. Sahu, S. Li, C.D. Taylor, W. Windl, J.R. Scully, G.S. Frankel, Electrochemical metrics for corrosion resistant alloys, Sci. Data. 8 (2021) 1–11. https://doi.org/10.1038/s41597-021-00840-y.

[138] G. Chi, D. Yi, H. Liu, Effect of roughness on electrochemical and pitting corrosion of Ti-6Al-4V alloy in 12 wt.% HCl solution at 35 °C, J. Mater. Res. Technol. 9 (2020) 1162–1174. https://doi.org/10.1016/j.jmrt.2019.11.044.

[139] Andrzej Lasia, Electrochemical Impedance Spectroscopy and its Applications, Springer, New York, 2014. https://doi.org/10.1016/B978-044452190-3.00010-0.

[140] Gamry Instruments, Basics of Electrochemical Impedance Spectroscopy, Aplication Note, (2011) 37–70. https://doi.org/10.1201/b11100-5.

[141] Princeton Applied Research, Basics of Electrochemical Impedance Spectroscopy, application Note AC-1, (1995) 1–13.

[142] A. Berradja, Electrochemical Techniques for Corrosion and Tribocorrosion Monitoring: Methods for the Assessment of Corrosion Rates, in: Corros. Inhib., 2019: pp. 1–26. https://doi.org/10.5772/intechopen.86743.

[143] U. Angst, B. Elsener, C.K. Larsen, Ø. Vennesland, Critical chloride content in reinforced concrete - A review, Cem. Concr. Res. 39 (2009) 1122–1138. https://doi.org/10.1016/j.cemconres.2009.08.006.

[144] S. Mundra, M. Criado, S.A. Bernal, J.L. Provis, Chloride-induced corrosion of steel rebars in simulated pore solutions of alkali-activated concretes, Cem. Concr. Res. 100 (2017) 385–397. https://doi.org/10.1016/j.cemconres.2017.08.006.

[145] P. Ghods, O.B. Isgor, G. McRae, G.P. Gu, J. Li, Effect of surface condition on the chloride-induced depassivation of rebar in concrete, 12th Int. Conf. Fract. 2009, ICF-12. (2009).

[146] Z. Ai, W. Sun, J. Jiang, D. Song, H. Ma, J. Zhang, D. Wang, Passivation characteristics of alloy corrosion-resistant steel Cr10Mo1 in simulating concrete pore solutions: combination effects of pH and chloride, Materials (Basel). 9 (2016) 1–17. https://doi.org/10.3390/ma9090749.

[147] J.W. Schultze, M.M. Lohrengel, D. Ross, Nucleation and growth of anodic oxide films, Electrochim. Acta. 28 (1983) 973–984. https://doi.org/10.1016/0013-4686(83)85175-5.

[148] Y.X. Qiao, Y.G. Zheng, W. Ke, P.C. Okafor, Electrochemical behaviour of high nitrogen stainless steel in acidic solutions, Corros. Sci. 51 (2009) 979–986. https://doi.org/10.1016/j.corsci.2009.02.026.

[149] D.K. Priest, Electrochemical Aspects of Stress Corrosion, J. Electrochem. Soc. 106 (1959) 358–360. https://doi.org/10.1149/1.2427346.

[150] J. Ninlachart, K.S. Raja, Passivation kinetics of Mg-Nd-Gd-Zn-Zr (EV31A) and Mg-Y-Nd-Gd-Zr (WE43C) in NaOH solutions, J. Magnes. Alloy. 5 (2017) 254–270. https://doi.org/10.1016/j.jma.2017.08.004.

[151] C. Escriva Cerdan, Caracterización de la pasividad del acero Inoxidable UNS N08031 en ácido fosfórico contaminado mediante técnicas electroquímicas, Ph.D. thesis, Universitat Politècnica de València, 2013.

[152] ISO 4288:1996 Geometrical Product Specifications (GPS). Surface texture: Profile method for the assessment of surface texture, International Standard Organization, 1996.

[153] A. Hankin, F.E. Bedoya-Lora, J.C. Alexander, A. Regoutz, G.H. Kelsall, Flat band potential determination: Avoiding the pitfalls, J. Mater. Chem. A. 7 (2019) 26162–26176. https://doi.org/10.1039/c9ta09569a.

[154] R. Beranek, (Photo)electrochemical methods for the determination of the band edge positions of TiO2-based nanomaterials, Adv. Phys. Chem. (2011) 1–20. https://doi.org/10.1155/2011/786759.

[155] ASTM G5-94(2011)e1, Standard Reference Test Method for Making Potentiostatic and Potentiodynamic Anodic Polarization Measurements, ASTM International, West Conshohocken, PA, www.astm.org, 2011.

[156] ASTM B368-21, Standard Test Method for Copper-Accelerated Acetic Acid-Salt Spray (Fog) Testing (CASS Test), ASTM International, West Conshohocken, PA, www.astm.org, 2021.

[157] B.S. Kang, Y.T. Sul, S.J. Oh, H.J. Lee, T. Albrektsson, XPS, AES and SEM analysis of recent dental implants, Acta Biomater. 5 (2009) 2222–2229. https://doi.org/10.1016/j.actbio.2009.01.049.

[158] F. Mangolini, J.B. McClimon, F. Rose, R.W. Carpick, Accounting for nanometer-thick adventitious carbon contamination in X-ray absorption spectra of carbon-based materials, Anal. Chem. 86 (2014) 12258–12265. https://doi.org/10.1021/ac503409c.

[159] S. Sinha, M. Mukherjee, A study of adventitious contamination layers on technically important substrates by photoemission and NEXAFS spectroscopies, Vacuum. 148 (2018) 48–53. https://doi.org/10.1016/j.vacuum.2017.10.038.

[160] R. Steinberger, C.E. Celedón, B. Bruckner, D. Roth, J. Duchoslav, M. Arndt, P. Kürnsteiner, T. Steck, J. Faderl, C.K. Riener, G. Angeli, P. Bauer, D. Stifter, Oxygen accumulation on metal surfaces investigated by XPS, AES and LEIS, an issue for sputter depth profiling under UHV conditions, Appl. Surf. Sci. 411 (2017) 189–196. https://doi.org/10.1016/j.apsusc.2017.03.163.

[161] F.I. Danilov, V.S. Protsenko, V.O. Gordiienko, Electrode processes occurring during the electrodeposition of chromium-carbon coatings from solutions of Cr(III) salts with carbamide and formic acid additions, Russ. J. Electrochem. 49 (2013) 475–482. https://doi.org/10.1134/S1023193513050054.

[162] L.Q. Guo, S.X. Qin, B.J. Yang, D. Liang, L.J. Qiao, Effect of hydrogen on semiconductive properties of passive film on ferrite and austenite phases in a duplex stainless steel, Sci. Rep. 7 (2017) 1–6. https://doi.org/10.1038/s41598-017-03480-8.

[163] T. Xie, A. Rani, B. Wen, A. Castillo, B. Thomson, R. Debnath, T.E. Murphy, R.D. Gomez, A. Motayed, The effects of surface conditions of TiO2 thin film on the UV

assisted sensing response at room temperature, Thin Solid Films. 620 (2016) 76–81. https://doi.org/10.1016/j.tsf.2016.07.075.

[164] E. McCafferty, J.P. Wightman, Determination of the concentration of surface hydroxyl groups on metal oxide films by a quantitative XPS method, Surf. Interface Anal. 26 (1998) 549–564. https://doi.org/10.1002/(sici)1096-9918(199807)26:8<549::aid-sia396>3.3.co;2-h.

[165] Z.D. Hood, S.P. Adhikari, S.F. Evans, H. Wang, Y. Li, A.K. Naskar, M. Chi, A. Lachgar, M.P. Paranthaman, Tire-derived carbon for catalytic preparation of biofuels from feedstocks containing free fatty acids, Carbon Resour. Convers. 1 (2018) 165–173. https://doi.org/10.1016/j.crcon.2018.07.007.

[166] C.E. Lu, N.W. Pu, K.H. Hou, C.C. Tseng, M. Der Ger, The effect of formic acid concentration on the conductivity and corrosion resistance of chromium carbide coatings electroplated with trivalent chromium, Appl. Surf. Sci. 282 (2013) 544–551. https://doi.org/10.1016/j.apsusc.2013.06.008.

[167] S. Mahdavi, S.R. Allahkaram, Investigation of Tribological Behavior of Electrodeposited Cr, Co-Cr and Co-Cr/TiO2 Nano-Composite Coatings, Int. J. Mater. Metall. Eng. 9 (2015) 787–791. https://doi.org/doi.org/10.5281/zenodo.1107019.

[168] K. Nygren, M. Samuelsson, A. Flink, H. Ljungcrantz, Å. Kassman Rudolphi, U. Jansson, Growth and characterization of chromium carbide films deposited by high rate reactive magnetron sputtering for electrical contact applications, Surf. Coatings Technol. 260 (2014) 326–334. https://doi.org/10.1016/j.surfcoat.2014.06.069.

[169] M.C. Biesinger, B.P. Payne, A.P. Grosvenor, L.W.M. Lau, A.R. Gerson, R.S.C. Smart, Resolving surface chemical states in XPS analysis of first row transition metals, oxides and hydroxides: Cr, Mn, Fe, Co and Ni, Appl. Surf. Sci. 257 (2011) 2717–2730. https://doi.org/10.1016/j.apsusc.2010.10.051.

[170] S. Tardio, M.-L. Abel, R.H. Carr, J.E. Castle, J.F. Watts, Comparative study of the native oxide on 316L stainless steel by XPS and ToF-SIMS, J. Vac. Sci. Technol. A Vacuum, Surfaces, Film. 33 (2015) 1–14. https://doi.org/10.1116/1.4927319.

[171] Z. Wang, F. Di-Franco, A. Seyeux, S. Zanna, V. Maurice, P. Marcus, Passivation-Induced Physicochemical Alterations of the Native Surface Oxide Film on 316L Austenitic Stainless Steel, J. Electrochem. Soc. 166 (2019) C3376–C3388. https://doi.org/10.1149/2.0321911jes.

[172] M.G.S. Ferreira, M. Da Cunha Belo, N.E. Hakiki, G. Goodlet, M.F. Montemor, A.M.P. Simões, Semiconducting properties of oxide and passive films formed on AISI 304 stainless steel and Alloy 600, J. Braz. Chem. Soc. 13 (2002) 433–440. https://doi.org/10.1590/S0103-50532002000400005.

[173] E.S.M. Sherif, A comparative study on the electrochemical corrosion behavior of iron and X-65 steel in 4.0 wt % sodium chloride solution after different exposure intervals, Molecules. 19 (2014) 9962–9974. https://doi.org/10.3390/molecules19079962.

[174] Q. Li, H. Lu, J. Cui, M. An, D. Li, Understanding the low corrosion potential and high corrosion resistance of nano-zinc electrodeposit based on electron work function and interfacial potential difference, RSC Adv. 6 (2016) 97606–97612. https://doi.org/10.1039/c6ra19563f.

[175] N. Li, Y. Li, S. Wang, F. Wang, Electrochemical corrosion behavior of

nanocrystallized bulk 304 stainless steel, Electrochim. Acta. 52 (2006) 760–765. https://doi.org/10.1016/j.electacta.2006.06.023.

[176] M. Långberg, C. Örnek, F. Zhang, J. Cheng, M. Liu, E. Grånäs, C. Wiemann, A. Gloskovskii, Y. Matveyev, S. Kulkarni, H. Noei, T.F. Keller, D. Lindell, U. Kivisäkk, E. Lundgren, A. Stierle, J. Pan, Characterization of Native Oxide and Passive Film on Austenite/Ferrite Phases of Duplex Stainless Steel Using Synchrotron HAXPEEM, J. Electrochem. Soc. 166 (2019) C3336–C3340. https://doi.org/10.1149/2.0421911jes.

[177] Z. Wang, E.M. Paschalidou, A. Seyeux, S. Zanna, V. Maurice, P. Marcus, Mechanisms of Cr and Mo Enrichments in the Passive Oxide Film on 316L Austenitic Stainless Steel, Front. Mater. 6 (2019) 1–12. https://doi.org/10.3389/fmats.2019.00232.

[178] Z. Wang, C. Carrière, A. Seyeux, S. Zanna, D. Mercier, P. Marcus, XPS and ToF-SIMS Investigation of Native Oxides and Passive Films Formed on Nickel Alloys Containing Chromium and Molybdenum, J. Electrochem. Soc. 168 (2021). https://doi.org/10.1149/1945-7111/abf308.

[179] H.J. Jang, H.O. Lee, H.G. Kim, Effects of Crystallization on the Corrosion and Passivity of Amorphous Pd-Fe-Co-Si-B Alloys, J. Nanomater. 2017 (2017) 1–7. https://doi.org/10.1155/2017/8973161.

[180] C. Wang, J. Yu, Y. Yu, Y. Zhao, Y. Zhang, X. Han, Comparison of the corrosion and passivity behavior between CrMnFeCoNi and CrFeCoNi coatings prepared by argon arc cladding, J. Mater. Res. Technol. 9 (2020) 8482–8496. https://doi.org/10.1016/j.jmrt.2020.05.093.

[181] M.J. Muñoz-Portero, J. García-Antón, J.L. Guiñón, V. Pérez-Herranz, Pourbaix diagrams for chromium in concentrated aqueous lithium bromide solutions at 25 °C, Corros. Sci. 51 (2009) 807–819. https://doi.org/10.1016/j.corsci.2009.01.004.

[182] A. Rossi, B. Elsener, G. Hähner, M. Textor, N.D. Spencer, XPS, AES and ToF-SIMS investigation of surface films and the role of inclusions on pitting corrosion in austenitic stainless steels, Surf. Interface Anal. 29 (2000) 460–467. https://doi.org/10.1002/1096-9918(200007)29:7<460::AID-SIA889>3.0.CO;2-T.

[183] P. Keller, H.H. Strehblow, XPS investigations of electrochemically formed passive layers on Fe/Cr-alloys in 0.5 M H2SO4, Corros. Sci. 46 (2004) 1939–1952. https://doi.org/10.1016/j.corsci.2004.01.007.

[184] M. Detroye, F. Reniers, C. Buess-Herman, J. Vereecken, AES-XPS study of chromium carbides and chromium iron carbides, Appl. Surf. Sci. 144–145 (1999) 78–82. https://doi.org/10.1016/S0169-4332(98)00769-7.

[185] R. Kierchheim, B. Heine, H. Fischmeister, S. Hofmann, H. Knote, U. Stolz, The Passivity of Iron-Chromium Alloys, Corros. Sci. 29 (1989) 899–917. https://doi.org/10.1016/0010-938X(89)90060-7.

[186] Y.Y. Yang, Y.Y. Liu, M.L. Cheng, N.W. Dai, M. Sun, J. Li, Y.M. Jiang, Enhancements of Passive Film and Pitting Resistance in Chloride Solution for 316LX Austenitic Stainless Steel After Sn Alloying, Acta Metall. Sin. (English Lett. 32 (2019) 98–106. https://doi.org/10.1007/s40195-018-0855-9.

[187] K. Asami, K. Hashimoto, S. Shimodaira, An XPS study of the passivity of a series of iron-chromium alloys in sulphuric acid, Corros. Sci. 18 (1978) 151–160. https://doi.org/10.1016/S0010-938X(78)80085-7.

[188] X. Peng, Y. Zhang, F. Wang, A novel electrodeposited Ni-Cr nanocomposite with increased resistance to pitting corrosion in 3.5% NaCl solution, Electrochem. Solid-State Lett. 8 (2005) B46–B49. https://doi.org/10.1149/1.1960169.

[189] S. Zhang, C. Sun, J. Di, Y. Tan, Corrosion behavior and morphology of passive films modified with zinc–aluminum simultaneous treatment on different metals, Metals (Basel). 10 (2020) 1–20. https://doi.org/10.3390/met10080986.

[190] T. Yamashita, P. Hayes, Analysis of XPS spectra of Fe 2+ and Fe 3+ ions in oxide materials, Appl. Surf. Sci. 254 (2008) 2441–2449. https://doi.org/10.1016/j.apsusc.2007.09.063.

[191] A. Mekki, D. Holland, C.F. McConville, M. Salim, An XPS study of iron sodium silicate glass surfaces, J. Non. Cryst. Solids. 208 (1996) 267–276. https://doi.org/10.1016/S0022-3093(96)00523-6.

[192] G. Lorang, M. Da Cunha Belo, A.M.P. Simões, M.G.S. Ferreira, Chemical Composition of Passive Films on AISI 304 Stainless Steel, J. Electrochem. Soc. 141 (1994) 3347–3356. https://doi.org/10.1149/1.2059338.

[193] J.J. Kim, Y.M. Young, Study on the passive film of type 316 stainless steel, Int. J. Electrochem. Sci. 8 (2013) 11847–11859.

[194] L. Freire, M.A. Catarino, M.I. Godinho, M.J. Ferreira, M.G.S. Ferreira, A.M.P. Simões, M.F. Montemor, Electrochemical and analytical investigation of passive films formed on stainless steels in alkaline media, Cem. Concr. Compos. 34 (2012) 1075–1081. https://doi.org/10.1016/j.cemconcomp.2012.06.002.

[195] J.Y. Jiang, D. Wang, H.Y. Chu, H. Ma, Y. Liu, Y. Gao, J. Shi, W. Sun, The passive film growth mechanism of new corrosion-resistant steel rebar in simulated concrete pore solution: Nanometer structure and electrochemical study, Materials (Basel). 10 (2017) 1–14. https://doi.org/10.3390/ma10040412.

[196] J. Wielant, V. Goossens, R. Hausbrand, H. Terryn, Electronic properties of thermally formed thin iron oxide films, Electrochim. Acta. 52 (2007) 7617–7625. https://doi.org/10.1016/j.electacta.2006.12.041.

[197] A. Kocijan, Č. Donik, M. Jenko, Electrochemical and XPS studies of the passive film formed on stainless steels in borate buffer and chloride solutions, Corros. Sci. 49 (2007) 2083–2098. https://doi.org/10.1016/j.corsci.2006.11.001.

[198] W.S. Li, J.L. Luo, Electrochemical investigations on formation and pitting susceptibility of passive films on iron and iron-based alloys, Int. J. Electrochem. Sci. 2 (2007) 627–665.

[199] Z. Petrović, M. Metikos-Huković, R. Peter, M. Petravić, Surface modification of iron for corrosion protection: Kinetics of anodic film formation and electroreduction, Int. J. Electrochem. Sci. 7 (2012) 9232–9247.

[200] M. Ebrahimi, I. Danaee, H. Eskandari, S. Nikmanesh, Corrosion Resistance and Semiconducting Properties of the Passive Films on Duplex Stainless Steel 2205, Int. J. ISSI. 14 (2017) 9–15.

[201] M.G.S. Ferreira, A.M.P. Simões, C. Compere, B. Rondot, M. Da Cunha Belo, Semiconducting behaviour of stainless steel passive films in contact with artificial seawater, Mater. Sci. Forum. 289–292 (1998) 887–894. https://doi.org/10.4028/www.scientific.net/msf.289-292.887.

[202] S. Ahn, H. Kwon, Diffusivity of point defects in the passive film on Fe, J.

Electroanal. Chem. 579 (2005) 311–319. https://doi.org/10.1016/B978-044452224-5/50050-0.

[203] Y. Qiao, X. Cai, J. Cui, H. Li, Passivity and Semiconducting Behavior of a High Nitrogen Stainless Steel in Acidic NaCl Solution, Adv. Mater. Sci. Eng. (2016) 1–8. https://doi.org/10.1155/2016/6065481.

[204] D. Zou, R. Liu, J. Li, W. Zhang, D. Wang, Y. Han, Corrosion resistance and semiconducting properties of passive films formed on 00Cr13Ni5Mo2 supermartensitic stainless steel in Cl- environment, J. Iron Steel Res. Int. 21 (2014) 630–636. https://doi.org/10.1016/S1006-706X(14)60098-4.

[205] E.M.A. Martini, I.L. Muller, Characterization of the film formed on iron borate solution by electrochemical impedance spectroscopy, Corros. Sci. 42 (2000) 443–454. https://doi.org/10.1016/S0010-938X(99)00064-5.

[206] K. Azumi, T. Ohtsuka, N. Sato, Mott-Schottky Plot of the Passive Film Formed on Iron in Neutral Borate and Phosphate Solutions, J. Electrochem. Soc. 134 (1987) 1352–1357. https://doi.org/10.1149/1.2100672.

[207] J.A.L. Dobbelaar, E.C.M. Herman, J.H.W. de Wit, The corrosion behaviour of iron-chromium alloys in 0.5 M sulphuric acid, Corros. Sci. 33 (1992) 765–778. https://doi.org/10.1016/0010-938X(92)90109-G.

[208] Y. Yu, S. Shironita, K. Souma, M. Umeda, Effect of chromium content on the corrosion resistance of ferritic stainless steels in sulfuric acid solution, Heliyon. 4 (2018) 1–13. https://doi.org/10.1016/j.heliyon.2018.e00958.

[209] B. Ter-Ovanessian, N. Mary, B. Normand, Passivity Breakdown of Ni-Cr Alloys: From Anions Interactions to Stable Pits Growth, J. Electrochem. Soc. 163 (2016) C410–C419. https://doi.org/10.1149/2.0381608jes.

[210] G. Bianchi, A. Cerquetti, F. Mazza, S. Torchio, Electronic properties of oxide films and pitting susceptibility of type 304 stainless steel, Corros. Sci. 12 (1972) 495–502. https://doi.org/https://doi.org/10.1016/S0010-938X(72)80080-5.

[211] F. Ammeloot, B. Millet, C. Fiaud, L. Robbiola, E.M.M. Sutter, Characterization of naturally grown oxide layers on copper with and without benzotriazole by electrochemical and photoelectrochemical measurements, in: Met. 95; Int. Conf. Met. Conserv., 1997: pp. 95–98.

[212] S. Gao, C. Dong, H. Luo, K. Xiao, X. Li, Electrochemical Behavior and Nonlinear Mott-Schottky Characterization of a Stainless Steel Passive Film, Anal. Lett. 47 (2014) 1162–1181. https://doi.org/10.1080/00032719.2013.865201.

[213] P. Selvam, B. Viswanathan, V. Srinivasan, Ion-induced carbide formation of TiFe: evidence from XPS and AES studies, J. Less-Common Met. 161 (1990) 77–85. https://doi.org/10.1016/0022-5088(90)90315-B.

[214] Z. Zeng, L. Wang, A. Liang, J. Zhang, Tribological and electrochemical behavior of thick Cr-C alloy coatings electrodeposited in trivalent chromium bath as an alternative to conventional Cr coatings, Electrochim. Acta. 52 (2006) 1366–1373. https://doi.org/10.1016/j.electacta.2006.07.038.

[215] L. Wang, A. Seyeux, P. Marcus, Thermal stability of the passive film formed on 316L stainless steel surface studied by ToF-SIMS, Corros. Sci. 165 (2019). https://doi.org/10.1016/j.corsci.2019.108395.

[216] S. Fujimoto, H. Tsuchiya, Semiconductor properties and protective role of passive

films of iron base alloys, Corros. Sci. 49 (2007) 195–202.
https://doi.org/10.1016/j.corsci.2006.05.020.

[217] O.M. Ozkendir, Electronic and crystal structure analysis of the FeCrO3 oxide, J. Electron Spectros. Relat. Phenomena. 191 (2013) 54–59. https://doi.org/10.1016/j.elspec.2013.10.004.

[218] G.C. Vásquez, D. Maestre, A. Cremades, J. Ramírez-Castellanos, E. Magnano, S. Nappini, S.Z. Karazhanov, Understanding the effects of Cr doping in rutile TiO2 by DFT calculations and X-ray spectroscopy, Sci. Rep. 8 (2018) 1–13. https://doi.org/10.1038/s41598-018-26728-3.

[219] J.G. Chen, B. Frühberger, J. Eng, B.E. Bent, Controlling surface reactivities of transition metals by carbide formation, J. Mol. Catal. A Chem. 131 (1998) 285–299. https://doi.org/10.1016/S1381-1169(97)00271-9.

[220] M. Magnuson, M. Andersson, J. Lu, L. Hultman, U. Jansson, Electronic structure and chemical bonding of amorphous chromium carbide thin films, J. Phys. Condens. Matter. 24 (2012) 1–7. https://doi.org/10.1088/0953-8984/24/22/225004.

[221] C.L. Chen, C.L. Dong, K. Asokan, G. Chern, C.L. Chang, Electronic structure of Cr doped Fe3O4 thin films by X-ray absorption near-edge structure spectroscopy, Solid State Commun. 272 (2018) 48–52. https://doi.org/10.1016/j.ssc.2018.01.011.

[222] C.L. Chang, S.K.R.S. Sankaranarayanan, M.H. Engelhard, V. Shutthanandan, S. Ramanathan, On the relationship between nonstoichiometry and passivity breakdown in ultrathin oxides: combined depth-dependent spectroscopy, mott-schottky analysis, and molecular dynamics simulation studies, J. Phys. Chem. C. 113 (2009) 3502–3511. https://doi.org/10.1021/jp808424g.

[223] K. Jaffré, B. Ter-Ovanessian, H. Abe, N. Mary, B. Normand, Y. Watanabe, Effect of mechanical surface treatments on the surface state and passive behavior of 304L stainless steel, Metals (Basel). 11 (2021) 1–14. https://doi.org/10.3390/met11010135.

[224] H. Bin Sun, Study on the anticorrosion of Zn-Ni alloy passivation film, in: Proc. Third Int. Symp. Corros. Reliab. Electron. Mater. Devices, 1994.

[225] A.R. Brooks, C.R. Clayton, K. Doss, Y.C. Lu, On the Role of Cr in the Passivity of Stainless Steel, J. Electrochem. Soc. 133 (1986) 2459–2464. https://doi.org/10.1149/1.2108450.

SCIENTIFIC CURRICULUM

Several scientific-related activities have been carried out during this Ph.D., covering from theoretical practical courses or seminars, as well as activities aimed at the development of the divulgation skills, such as the development of scientific publications or attendance to scientific conferences:

- *Courses*

    o Electrochemical Doctoral School in Corrosion 2018, organised by SURF research group of VUB in Brussels (02/2018).

    o Optimizing Adhesion to Metal (inks, lacquers, structural adhesives…)". Prof. Gary Critchlow of Loughborough University (2h, 01/2018).

    o Fundaments and applications of x-ray photoelectronic spectroscopy (XPS)". Organised by SGIker, UPV/EHU in Leioa (20 h, 10/2017).

    o Quality of the measurement" at CIDETEC. 03/2017 (16 hours).

- *Seminars*

    o Aplicación de la normativa europea REACH & CLP (Fernández Almau, REACH Plus, 12/2019).

    o Introducción a la norma UNE-EN ISO 17025 (Juan Carlos Morla, SONDER CONSULTING, S.L., 09/2019).

    o SECM - Una técnica electroquímica localizada con múltiples aplicaciones en investigación (Assist. Prof. Yaiza Gonzalez-Garcia, Materials Science and Engineering department – TU Delft, Holanda, 03/2019).

    o The Kaleidoscope of Surface Engineering". T.S. Sudarshan Ph.D, 06/2017.

    o Thermal spray, vision form an expert. Dr. Sergio Armada, 05/2017.

- *Webinar*

    o Introducción al software COMSOL Multiphysics (modelado multifísico de procesos de electrodeposición), 09/2018.

    o Non-Destructive Electrochemical Methods for Corrosion Testing" (Metrohm, 04/2017).

    o "New Spectroscopic Techniques in Energy Research" (CellPress, 04/2017).

- *Workshop*

    o Retos y necesidades en la caracterización de materiales y recubrimientos (Fischer Instruments, San-Sebastián, 05/2019).

- Conferences

    o Oral communication presented at the ECASIA'19 conference in Dresden (09/2019).

    J. León, J. M. Vega, B. Ter-Ovanessian, S. Pletincx, B. Normand, H. Terryn, E. García-Lecina, H. Grande. Impact of the Fe concentration in sulphate based trivalent Cr electrolytes on the final properties of electroplated Cr coatings.

    o Poster communication in the EIS 2019 conference in Cap-ferret (06/2019).

    J. León, J. M. Vega, B. Ter-Ovanessian, S. Pletincx, B. Normand, H. Terryn, E. García-Lecina, H. Grande, Effect of Fe on the semiconducting properties of passive films formed on model sulphate based trivalent chromium electroplated coatings.

    o Poster communication (and flash presentation) in the SMT32 conference in San Sebastián (June, 2018).

    J. León, E. García-Lecina, J. M. Vega, H. Grande, H. Terryn, B. Normand, B. Ter-Ovanessian. Corrosion resistance and semiconducting properties of chromium electrodeposits obtained from model electrolytes.

- *Publications*

  o *J. León, S. Pletincx, H. Terryn, B. Özkaya, E. García-Lecina, J. M. Vega. Unrevealing the Fe effect on the corrosion of chromium coatings: chemical composition and semiconducting properties.*

  Published in the Journal of the Electrochemical Society (11/2021).
  Leon et al 2021 *J. Electrochem. Soc* https://doi.org/10.1149/1945-7111/ac3ac0

- *User participant in synchrotron measurements*

  o ALBA Synchrotron, Cedanyola del Vallès (Barcelona, Spain).

  Proposal ID: 2019023326. *Impact of the chemical composition, thickness and density on the corrosion resistance and semiconducting capabilities of Cr nanocoatings and their oxides by synchrotron XRR and NEXAFS.*

 *Beamline:* BOREAS, HECTOR endstation.

  Date: 08/12/2019.

APPENDIXES

Appendix A

The XPS depth profile of the Cr standard is shown in the *Figure 46* (a). Similar findings to the AES depth profile (*Figure 15* (a)) were observed: a predominant Cr concentration, together with an unexpected and uniform C and O concentration, approximately 20 and 10 % at. respectively. High resolution spectra of the Cr, C and O were measured (*Figure 46* (b, c, d)) to explain the presence of such elements in a bulk pure Cr standard.
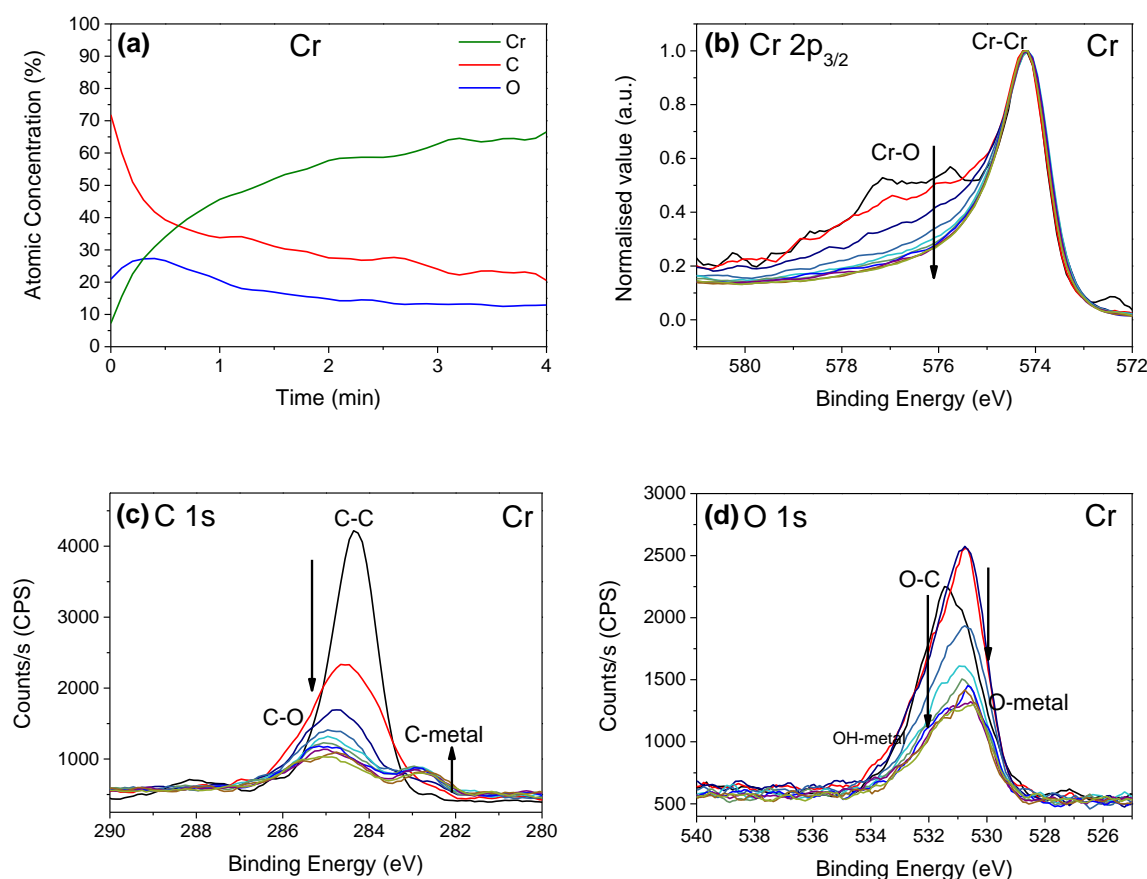
Figure 46. *XPS measurements on the Cr standard: (a) XPS depth profile, together with the (b) Cr $2p_{3/2}$, (c) C 1s and (d) O 1s high-resolution spectra, as a function of the sputtered depth.*

The Cr $2p_{3/2}$ peak (*Figure 46* (b)) shown an Cr oxide/hydroxide-rich surface that increases its metallic Cr contribution as the oxide layer is sputtered away, as expected.

The C 1s high-resolution spectra (*Figure 46* (c)) confirmed that the superficial C was constituted by an organic and adventitious C contamination layer; however, as the sputtering progressed a metal carbide signal appeared (approximately after 42 s of sputtering), which was unexpected to be found in a Cr standard of high purity (99.95 %). Most probably, this is an effect caused by the Ar ion gun, which sometimes can form such carbides on metallic surfaces (previously discussed in the chapter 4.1). Additionally, as

mentioned before in the chapter 4.1, this surface was found later to be contaminated with C particles, which could explain such results.

Regarding the O 1s spectra (*Figure 46* (d)), revealed that there were significant organic components on the surface (O-C) which disappeared partially when the sputtering was carried out at the same time that the metallic oxide (O-metal) contribution started to decrease; however, the signal was stabilised in a significant non-zero value. Initially this could point out to different events happening in the surface: (i) oxide presence inside the Cr standard, which seems very unlikely due to its high purity, (ii) repassivation of the surface, (iii) oxygen implantation caused by the Ar sputtering and (iv) detection of superficial oxygen due to an inhomogeneous sputtering of the Ar ion gun.

The Ar ion gun was calibrated and the measurements were repeated in other different XPS equipment, obtaining the same trend for the oxygen and being, as a result, the repassivation issue the most probable explanation.

Additionally, similar findings were observed during the AES depth profile on a Cr(III) sulphate-based electrodeposit (*Figure 47*), where a stable oxygen signal was found in the Cr layer. Then, the sample was stored at the vacuum chamber for 20 h and when measuring again an increase of the oxygen signal was observed, (almost three times, from an approximate 5 to 16 % at.), with no additional changes in the rest of the elements. This demonstrated the high reactivity of the Cr, even under UHV conditions, to react with traces of oxygen to oxidise its surface.
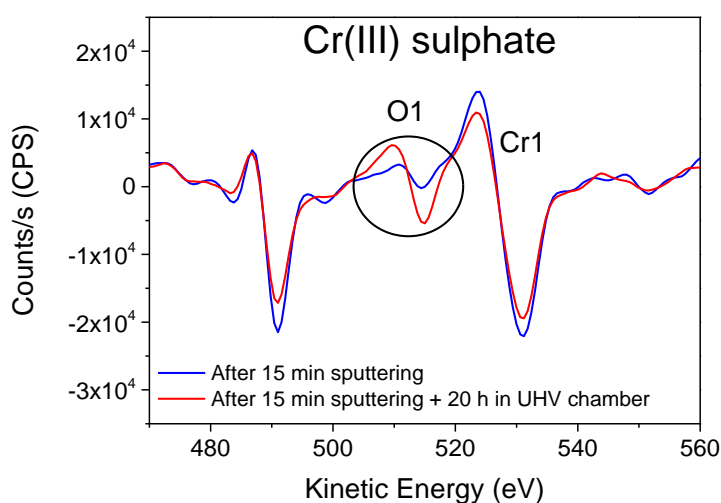
Figure 47. *AES survey spectra performed on the Cr(III)-sulphate coating after 15 min sputtering (blue line) and after 15 min sputtering + 20 h storage at the vacuum chamber (red line).*

This repassivation phenomenon could also be explained by some gas leakage of the chamber or due to a malfunction in the vacuum pump. However, this event was also observed in other different XPS equipment, reducing the probability of being caused by external oxygen entering in the vacuum chamber.

Appendix B

The native oxide layer of the Cr electrodeposits was removed electrochemically by following the same procedure used in the PDM measurements (*Table 8*) in order to find out if (i) the adsorbed S was hindering the native oxide layer formation, leading as a result to a more defective oxide layer, (ii) to confirm the findings observed in the section 4.3.3.1 regarding the enhanced semiconducting properties provided by the CrO_3 topmost layer in the Cr(VI)-based coating and (iii) to explain the discrepancies between the Mott-Schottky (study on the native oxide) and the PDM results.

The *Table 30* shows the obtained results and comparison between the semiconducting properties of the native oxide layer and the oxide films formed after removing the native oxide for all the Cr coating systems.

Table 30. Comparison of the electronic properties, calculated from the Mott-Schottky plot, for the native oxide layers and oxide films formed after removing electrochemically the native oxide layer.

Sample	Oxide layer	Mott-Schottky N_A ($x10^{20}$ cm^{-3})	PDM D_0 (cm^2 s^{-1})
Cr	Native	4.8 (0.1)	n/a
	After removing the native oxide layer	5.9 (0.6)	$7.2x10^{-19}$
Cr(III) chloride	Native	6.9 (0.2)	n/a
	After removing the native oxide layer	8.8 (0.5)	$1.6x10^{-18}$
Cr(III) sulphate	Native	8.0 (0.3)	n/a
	After removing the native oxide layer	4.7 (0.1)	$8.8x10^{-19}$
Cr(VI)	Native	0.3 (0.1)	n/a
	After removing the native oxide layer	5.0 (0.6)	$9.4x10^{-19}$

According to the findings of the Mott-Schottky of the chapter 4.1 and 4.3 (section 4.1.3.1 and 4.3.3.1) the following point defect concentration ranking was observed, in terms of native oxide layers: Cr(VI) << Cr < Cr(III) chloride < Cr(III) sulphate, concluding that, the Cr(VI) system possessed the lower point defects concentration (lower N_A) due to the presence of the CrO_3 thin layer, the pure Cr in second place as the ideal Cr system with a standard Cr oxide/hydroxide layer and then the Cr(III) systems, having the sulphate-based one a slightly higher value due to the presence of ad/absorbed S which hindered its oxide layer formation, leading to a more defective native oxide layer.

According to the table above, after removing the native oxide layer and studying the semiconducting properties of the new air-formed oxide layer all the systems got a more

defective oxide layer (higher N_A value), except for the sulphate-based Cr(III) system, which showed a decrease in the point defects concentration (from 8.0 to 4.7). This supports the hypothesis of the adsorbed S being the responsible of the more defective native oxide layer formation. During the electrochemical removal of its native oxide layer the adsorbed S was partially or totally removed and it did not participate or hinder the formation of the oxide film, leading to a less defective oxide. Analogously, the Cr(VI) loses the CrO_3 layer during the electrochemical removal of the native oxide layer and the point defects concentration is increased (from 0.3 to 5.0) supporting the hypothesis of such CrO_3 layer being the responsible of the enhanced semiconducting properties (also confirmed by polishing the surface in the 4.3.3.1 section).

Additionally, the pure Cr, Cr(VI) and Cr(III) sulphate system possessed similar N_A values after removing the native oxide layer (5.9, 4.7 and 5.0 respectively) in comparison to the significantly high value of the Cr(III) chloride system. In fact, this trend is positively correlated to the diffusion coefficient (D_0) of PDM results, having the Cr(III) chloride system a significantly higher value in comparison to the rest of the system which present lower and similar values. The higher D_0 and N_A values of Cr(III) chloride after removing the native oxide layer, in comparison to the Cr(III) sulphate system could explain the better corrosion resistance performance of the sulphate system in 0.1 M NaCl of the 1 year-aged samples (critical chloride content experiment in section 4.1.4.2.2).

This D_0 and N_A correlation after removing the native oxide layer also confirms that the properties of the native oxide layers formed on such Cr electrodeposits can be very different from their air-formed oxide layers after removing the native one. Therefore, the PDM measurements cannot be comparable to the M-S experiments when studying native oxide layer; however, PDM results are in agreement to the M-S after removing the native oxide layer (since in PDM the native oxide layer is removed).